Influence of highly contrasted dual-scale porosity carbon interlock fabrics on permeability, flow-induced deformation and saturation during CRTM process : Experimental characterization and modeling

Gabriela Soares Gambarini

MEMOIRE DE DOCTORAT DE

L'ECOLE CENTRALE DE NANTES

ECOLE DOCTORALE N° 602
Sciences de l'Ingénierie et des Systèmes
Spécialité : Mécanique des Solides, des Matériaux, des Structures et des surfaces

Par
Gabriela SOARES GAMBARINI

Influence of highly contrasted dual-scale porosity carbon interlock fabrics on permeability, flow-induced deformation and saturation during CRTM process

Projet de recherche doctoral présenté et soutenu à l'École Centrale de Nantes le 29 août 2023
Unité de recherche : UMR 6183, Institut de Recherche en Génie Civil et Mécanique (GeM)

Rapporteurs avant soutenance :

Véronique MICHAUD Associate professor, HDR, École Polytechnique Fédérale (EPF) Lausanne, Suisse

Joël BRÉARD Professeur des universités, Université de Caen Normandie

Composition du Jury :

Président : Jean-Luc BAILLEUL Professeur des universités, Nantes Université

Examinateurs :

Véronique MICHAUD Associate professor, HDR, École Polytechnique Fédérale (EPF) Lausanne, Suisse

Joël BRÉARD Professeur des universités, Université de Caen Normandie

Mylène LAGARDERE Maître-assistante, HDR, IMT Nord Europe

Directeur de recherches doctorales: Sébastien COMAS-CARDONA Professeur des universités, École Centrale de Nantes

Co-dir. de recherches doctorales : Christophe BINETRUY Professeur des universités, École Centrale de Nantes

Invité

Boris DUCHAMP Ingénieur de recherche, IRT M2P, Metz

Acknowledgements

First and foremost, my sincere appreciation to the entire team at IRT M2P, for giving me the opportunity to contribute to this project and for the enriching exchanges I had during my time in Nantes and when I went to Porcelette. I would also like to extend thanks to Safran Composites for their support, providing us with the necessary materials for this study, even during the challenging times of the COVID-19 pandemic.

I am deeply grateful to the exceptional team at Centrale Nantes that helped me in so many ways, specially my two advisors Sébastien Comas-Cardona and Christophe Binetruy for their expertise and support. It was a great pleasure to work and learn from you both and I deeply admire your passion for science and your strong work ethic. Your guidance was extremely important to me and I really can't thank you both enough. Also, special thanks to Jean-Michel Lebrun for his experimental support and to Gabriel Valdes Alonzo and Elena Syerko for their numerical analysis enriching this study.

I would like to express my gratitude to my incredible colleagues, who created a supportive and inspiring work environment where we cheered each other on during the highs and lows of thesis research. I wish you all the utmost success and i will miss sharing the workplace with you.

To my lovely friends, thank you for your encouragement and patience during this time, even when I was not as present. Your understanding and support mean a lot to me.

Lastly, I want to thank my family for their trust me and the choices I made. their constant support, even from afar. I love you all deeply, and I consider this accomplishment as much yours as it is mine.

In conclusion, I am immensely thankful to IRT M2P, my advisors from Centrale Nantes, colleagues, friends, and family for their support and encouragement. Your contributions were the most crucial thing for the completion of this thesis. I look forward to the future with optimism, knowing that I have been fortunate to have such a strong network of support behind me.

Thank you for everything.

Contents

Chapter 1

Introduction

In the industry of composite materials, the integration of 3D fiber reinforcements has emerged as a transformative advancement in Liquid Composite Molding (LCM) processes. 3D fiber reinforcements can improve the mechanical properties of a part, with superior transverse stiffness in comparison to 2D laminates, better interlaminar shear strength minimizing the risk of delamination, enhanced weight reduction amongst other advantages [71].

A layer-to-layer interlock fabric was developed by Safran composites within the context of the project INCREASE. This project was created to optimize the production of aeronautical components and is lead by IRT-M2P alongside different industrial partners. One of the key points of the INCREASE project is to decrease the duration of the injection/impregnation phase by the development of new fiber reinforcements and the implementation of the Compression Resin Transfer Molding (C-RTM) process in place of the traditional RTM process currently used for the production of fan blades.

Despite the growing interest in the integration of 3D fiber reinforcements in composite materials, there remains a significant gap in the literature regarding the characterization of these advanced materials. While numerous studies have investigated the mechanical properties and behavior of traditional 2D laminates, the same level of attention has not been given to the comprehensive characterization of 3D fiber reinforcements. The complex architecture of a 3D fiber reinforcement poses unique challenges in its experimental characterization because of the highly contrasted double-scale porosity and high transverse stiffness.

The interlock fabric is made of carbon-fibers, which makes it difficult to visualize the flow due to its non-translucent nature. It also possess very dense tows and open inter-tow spaces which created a highly-contrasted dual-scale porosity that affects the impregnation and does not saturate immediately. Different traditional permeability experimental methods will be modified in order to accommodate the specification of the fabric and measure the permeability correctly. Differently from the RTM process that has a constant cavity thickness, the C-RTM process compresses the fabric until the desired fiber volume fraction (Figure 1.1). This process can help minimize cycle time but also generates internal pressure if the process parameters such as the closing speed is too high, for example.

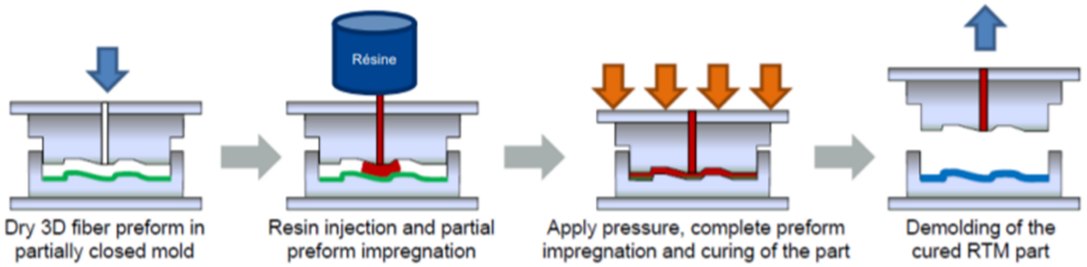

Figure 1.1: Schematic representation of the C-RTM process - provided by Safran composites.

When compared to the traditional RTM process, the modeling of the C-RTM process is more complex due to a higher number of parameters and particularly the change in cavity thickness and evolving fibrous architecture during the process process [63]. A simulation tool (PAM-RTM) is being developed to model the C-RTM process and the instrinsic permeability of the fabric **K** is an important parameter for the simulation and crucial for good quality impregnation. With the introduction to a compaction phase, the cavity size changes and the permeability evolution is needed across various fiber volume fractions.

This study will describe the experimental methodology used to characterize the permeability of an interlock fabric for the C-RTM process and the physical phenomena that could expected during it:

The **chapter 2** presents the state of the art that describes the types of textile reinforcements, the traditional experimental techniques used for the permeability characterization of composite fabrics, the compression behavior of fiber reinforcements, the fluid-solid interactions and the saturation measurement. This review sets the foundation necessary for the understanding of the subsequent chapters.

The **chapter 3** describes the fabrics and materials used in the different techniques presented in this study.

The **chapter 4** marks the beginning of the characterization section, focusing on the permeability measurement. The chapter describes the techniques used to measure both in-plane and transverse permeability of the INCREASE06 interlock fabric. The deviation angle is visually examined through injection techniques and the in-plane and transverse intrinsic (saturated) permeabilities during compression are measured using a unidirectional compression saturated technique. The measurements obtained from different techniques reveal a significant variation between the unsaturated permeability measured with injection techniques and the intrinsic saturated permeability from the unidirectional saturated compression. Both are important to understand the filling during the C-RTM process.

Chapter 5 introduces a methodology to identify the occurrence of flow-induced deformation during the compression of a saturated fabric. The mechanical signature of the interlock fabric is compared to that of traditional fabrics. The differences observed in the mechanical behavior are explained by variations in the weaving pattern between interlock, twill, and quasi-unidirectional fabrics. A processing window for the C-RTM process is presented with the limiting mold closing speed that is crucial to avoid flow-induced deformation.

The **chapter 6** describes the bench design for a dielectric sensor used to measure the saturation of the interlock fabric during injection. The bench design is adapted for conductive carbon fibers its integrated into a universal testing machine used control and

achieve the desired fiber volume fractions. The chapter discusses the measurement of parameters such as the unsaturated length and the time required for a specific area to reach full saturation. These measurements are performed at three different fiber volume fractions, from injections conducted in both the weft and warp directions of the fabric.

Chapter 2

State of the art

Contents

2.1 Textile composites

Textiles composites are largely used various industries such as in the aerospace, sporting and maritime [12]. The textile composite consists fiber yarns interlaced in different patterns through various techniques, including weaving, knitting, braiding, etc. plus a matrix material is typically a polymer resin Each technique has its own advantage and can be tailored to the requirements of the application.

2.1.1 Classification of textile reinforcements

The textiles can be classified accordingly to its dimension (1D, 2D or 3D) and its selection will depend on the desired properties regarding the manufacturing process and the desired mechanical properties of the final part. Figure 2.1 shows the classification of the various types of textiles:

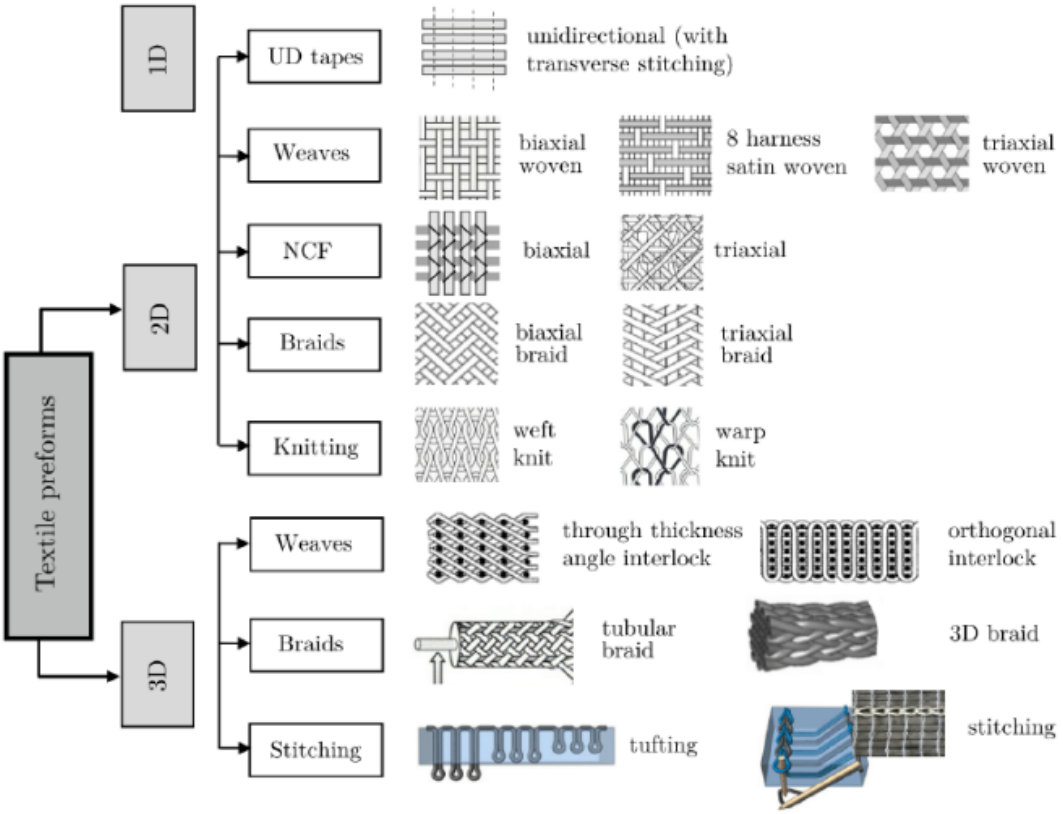

Figure 2.1: Textiles preforms classification according to dimension [53]

1D and quasi-unidirectional textiles

An unidirectional fibrous material is a type of reinforcement that is non-woven and have the fibers arranged in a single parallel direction. Single yarns or fiber bundles can be considered as unidirectional fibrous material. Tapes are also produced by aligning several bundles side by side.

Weaving can produce a quasi unidirectional fabric by incorporating a thin thread in the weft direction to hold the yarns together [53]. The unidirectional alignment of the fibers can provide great strength in the fiber direction [51], however, these materials are not suitable for parts that require strength in all directions, since they lack anisotropic strength. For those applications, 2D or 3D woven fabrics are more appropriate.

2D textiles

A woven 2D fabric consists of the weft and warp yarns interlaced together in a determined sequence to create a 2D surface. The interlacing pattern determines the type of weave and influences the mechanical and visual properties of the fabric. The most common 2D fabrics are plain, twill and satin weaves as seen in Figure 2.2:

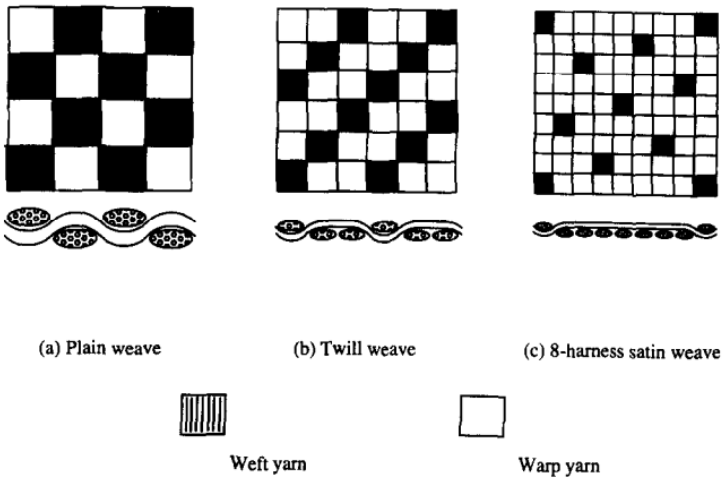

Figure 2.2: Schematics of the common weaves: (a) plain, (b) twill and, (c) harness satin [67].

The vast majority of composite parts are made using 2D textiles due to their wide availability, ease of draping and the ability to control desired characteristics through weaving operations (specific architecture styles and parameters such as yarn size, areal weight, tensions, etc [26].)

However, a limitation of 2D textiles is their susceptibility to delamination and cracking. Since they are stacked, delamination can occur between the layers if under stress of impact. This will compromise the structural integrity of the composite part. 3D reinforcements are presented as an interesting alternative over 2D fabrics for applications where the part is subjected to out-of-plane loading [71].

3D textiles

3D reinforcements have yarns in the x direction (warp), y direction (weft) and z direction (binding yarn). Due to the transverse binding yarns, the risk of delamination and cracking is greatly reduced.

3D reinforcements are being largely used in the aerospace industry where the parts are subjected to many special considerations and must be fail proof. In comparison to the labor-intensive process of cutting, preparing and stacking of numerous 2D layers, the use of 3D reinforcement lowers production time since the reinforcement is made in the desired thickness eliminating the need of additional layup.

The weaved 3D reinforcements can be categorized by the type of weaving architecture. The three main architectures are: layer-to-layer, angle and orthogonal interlock fabrics.

- Orthogonal: the binding yarn interlaces through the thickness of the preform in a 90° angle (one weft column)(Figure 2.3 a) ;

- Angle: the binding yarns passes through the thickness of the preform through more than two columns of weft threads [22](Figure b);

- Layer-to-layer: the binding yarn goes between two successive layers then goes back to its initial position (Figure 2.3 c);

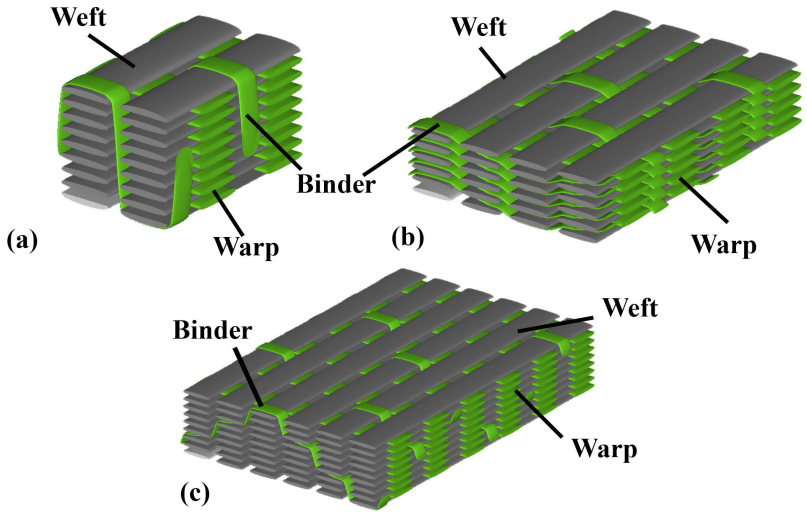

Figure 2.3: Schematic example of an Orthogonal (a), Layer-to-layer (b) and Angle interlock (c) [60].

The interlock fabric used in this study (INCREASE06 geometry that will be presented in detail in Chapter 3) has a layer-to-layer architecture.

2.2 Liquid Composite Molding - LCM

The Liquid Composite Molding family describes the type of manufacturing process where a dry reinforcement is placed in a mold and impregnated with a liquid polymeric resin. Compared to open mold techniques, LCM processes can achieve a higher fiber volume fraction (V_f) by compacting the reinforcement during the process [7]. The LCM processes can be classified in four main categories depending on the mold construction and strength and type of injection system: Resin Transfer Moulding (RTM), Compression Resin Transfer Moulding (C-RTM), RTMLight and vaccum assisted RTM.

The use of heavy press and rigid mold allows a faster process time and better dimensional tolerances. This is particularly advantageous in the production of aircraft turbine blades, where high-pressure RTM and, more recently, C-RTM techniques have been employed for serial production. Both processes are described as follows:

2.2.1 Resin Transfer Molding - RTM

The RTM process starts with the placing of the dry preform into the rigid mold (Figure 2.4 (a)). The mold is then closed to the desired final cavity thickness (Figure 2.4 (b)). Next, a liquid thermoset resin is injected into the preform through the inlet point (Figure 2.4 (c)). Once the resin is injected, it undergoes a curing process either by implementing a thermal cure cycle or waiting for the desired amount of time. After the curing process is done, the composite part is ready to be demolded as seen in Figure 2.4(d)).

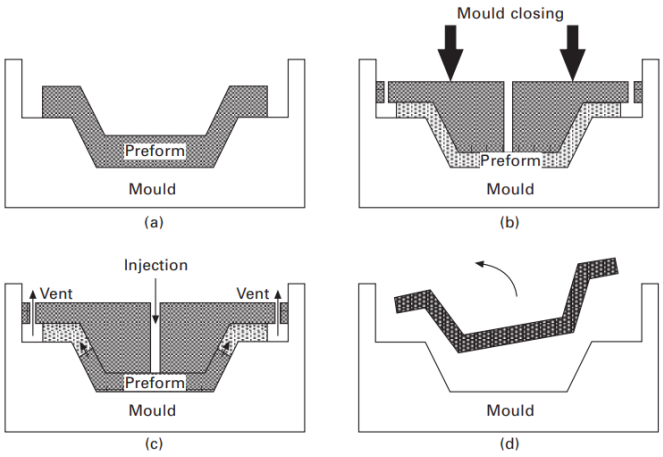

Figure 2.4: (a-d) Steps in the Resin Transfer Molding (RTM) process [7].

2.2.2 Compression Resin Transfer Molding - C-RTM

The difference between the C-RTM and traditional RTM is that the resin injection is done before the compaction to the final desired thickness. The process takes advantage of the higher permeability of the less compressed reinforcement in order to reduce cycle time [7]. As depicted in Figure 2.5, the resin can be injected into a not fully compacted reinforcement or into a gap and then compressed to decrease fluid pressure during injection.

C-RTM is a faster alternative in comparison to the traditional RTM, however, this comes with the expense of higher forces applied to the mold and higher fluid pressure at the end of the compaction step.

2.3 Permeability characterization of 3D interlock

2.3.1 Darcy's law

The first formulated law to explain the fluid flow in a porous medium was done by Henry Darcy in 1856 [17]. He performed a series of experiments to determine the flow velocity of water through a column of sand of know pressure gradient. He introduced the material parameter called (bulk) permeability K that characterizes the porous medium. The relation is given in 1D as follows:

$$u_D = -\frac{\mathrm{K}}{\mu}\nabla P \tag{2.1}$$

Where u_D is the Darcy's fluid velocity, ∇P the pressure gradient and μ the viscosity of the fluid.

This relation considered a porous medium that is homogeneous and isotropic therefore K is taken as constant. If the medium is anisotropic, the permeability must be seen now as a tensor $\boldsymbol{K}$.

Liakopoulos [39] expanded Darcy's equation and showed that the permeability K is a symmetric tensor of second rank that represents the ease of flow in all three-directions. If the permeability main directions coincide to the principal directions of the preform (weft, warp and z) then the diagonal permeability tensor $\mathbf{K}$ can be expressed as:

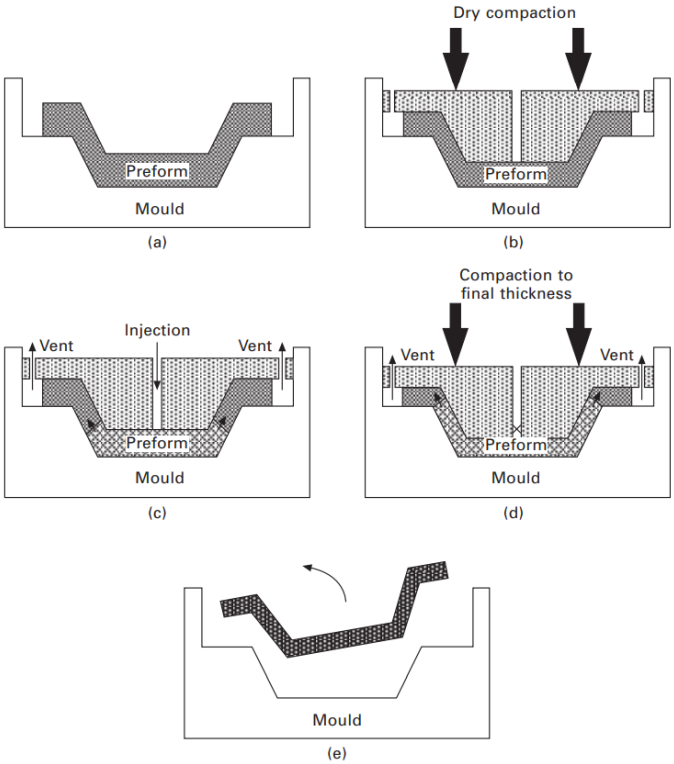

Figure 2.5: (a-e) Steps in the Compression Resin Transfer Moudling (C-RTM) process [7].

$$\boldsymbol{K} = \begin{bmatrix} K_{xx} & 0 & 0 \\ 0 & K_{yy} & 0 \\ 0 & 0 & K_{zz} \end{bmatrix} \tag{2.2}$$

If the permeability tensor is direction dependent in an orthotropic medium like fiber reinforcements composites, $\mathbf{K}$ takes then a form of a symmetric second order tensor with constant coefficients [65]. The in plane skew term K_{xy} and the through-thickness skew terms (K_{xz} and K_{yz}) appear when the tensor is rotated:

$$\boldsymbol{K} = \begin{bmatrix} K_{xx} & K_{xy} & K_{xz} \\ K_{xy} & K_{yy} & K_{yz} \\ K_{xz} & K_{yz} & K_{zz} \end{bmatrix} \tag{2.3}$$

2.3.2 Experimental permeability measurement techniques

Various methods to measure the permeability of fibrous media have been published over the last decades as reviewed by Sharma and Siginer [65]. They can be classified by the type of fluid (liquid or gas), type of flow (in-plane, transverse or three-dimensional) and also transient (unsaturated) or steady state (saturated) permeabilities. Three international benchmark exercises on the measurment of the permeability were carried out between 2011 and 2019 [42, 75, 4] and showed the importance of machine calibration and sample preparation to avoid scatter results.

2.3.2.1 Transient techniques

Transient techniques are done based on the wetting of a dry reinforcement. It measures the unsaturated permeability and its mostly done by capturing the flow front position over time during impregnation. It can be done at constant pressure or constant velocity and two most common techniques are radial flow and channel/rectilinear flow [65].

Rectilinear flow

It is an in-plane measurement technique to characterize the permeability by conducting a linear flow channel [75]. The preform is placed on a mold with a transparent side and a pressure difference is created by the injection of the fluid or a created vacuum. The flow front profiles are tracked with various means and the flow front position with time is used to calculate the permeability by the integration of 1-D Darcy's law (Fig.2.6).

It is an experiment easy to conduct, with high reproducibility, however, visualization tools and sensors are needed. It only determines the permeability component in one direction and for one fiber volume fraction V_f, therefore, a set of experiments is required at different directions for the characterization of all six tensor components for various V_f [61, 75].

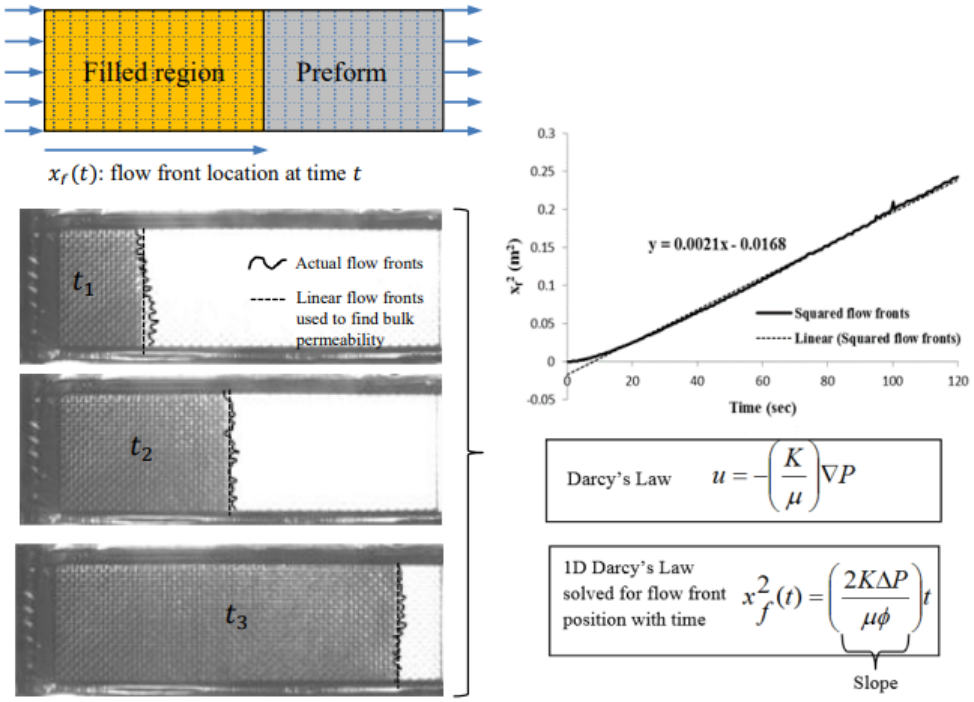

Figure 2.6: One-dimensional permeability characterization experiment to find the bulk permeability value in the direction of flow [61]

Radial flow

Radial flow is another transient technique for in-plane permeability measurement [42]. The fluid is injected on the center of the preform and a circular or elliptical flow profile is observed (Fig.2.13). If the preform is isotropic, the shape will be circular and as the anisotropy increases, so is the ratio between the major and minor axes of the ellipse [77]. A rotation of the ellipse with respect to the laboratory axes will allow the measurement of the main axes orientations.

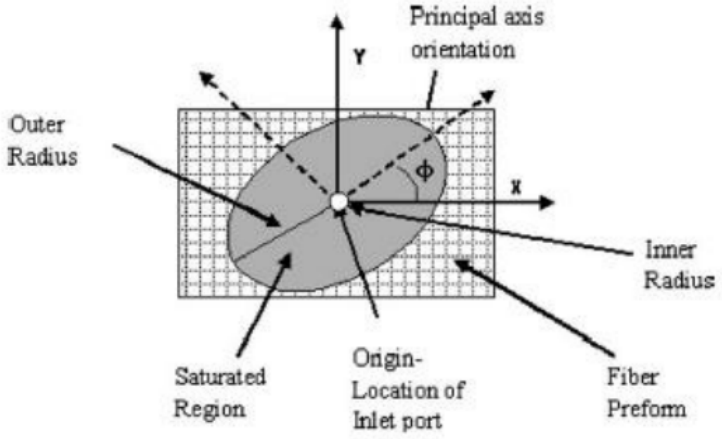

Figure 2.7: Radial flow pattern: Flow begins from the center and spreads in a circular or elliptical pattern [65].

Using the flow profile, Chan and Hwang proposed a procedure to obtain the principal in-plane permeability [14] then Weitzenbock et al [77] developed a method to calculate the anisotropic permeability of a reinforcement along the fabric's principal direction (K_1 and K_2) with a single experiment.

$$K_1 = \left\{ x_f^2 \left[2 \ln \left(x_f / x_o \right) - 1 \right] + x_o^2 \right\} \frac{1}{t} \frac{\mu \varepsilon}{4 \Delta P} \tag{2.4}$$

$$K_1 = \left\{ y_f^2 \left[2 \ln \left(y_f / y_o \right) - 1 \right] + y_o^2 \right\} \frac{1}{t} \frac{\mu \varepsilon}{4 \Delta P} \tag{2.5}$$

where x_f and y_f are the coordinates of the flow front position, x_o and y_o are the coordinates of the inlet radius, t is the time, μ the fluid viscosity, ε the porosity and ΔP the applied fluid pressure.

2.3.2.2 Techniques by saturated compression

In order to get detailed information of the permeability evolution to model LCM processes, techniques based on unidirectional compression of a saturated preform have been used. The technique can measure the evolution of the bulk permeability during compression (varying V_f). Buntain et al.[11] used the compression technique to calculate the isotropic permeability K_e. Then, an improved version of the technique was developed by Comas-Cardona [15] that allowed the determination of the through-thickness permeability during compression. Later, Martin et al.[41, 40] measured the two principal in-plane permeabilities K_1 and K_2 of an anisotropic fabric.

The technique uses the compression of a saturated fabric (Figure 2.8) to extract the fluid pressure evolution and then a numerical optimization methodology fits the experimental measurements to the consolidation equation:

$$\frac{K_e}{r} \frac{\partial}{\partial r} \left(r \frac{\partial P}{\partial r} \right) + K_z \left(\frac{V_f}{V_f^0} \right)^2 \frac{\partial^2 P}{\partial z^2} = -\mu \frac{\dot{V}_f}{V_f} \tag{2.6}$$

The saturated compression technique has the advantage of measuring the evolution of permeability over a wide range of V_f in a single test compared to the injection based techniques.

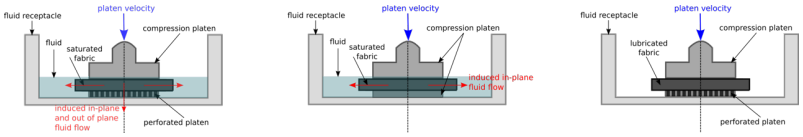

Figure 2.8: Unidirection compression of a saturated fabric to measure the transverse permeability (left), in plane permeability (center) and drained response to compression (right).

This technique will be used to measure the continuous intrinsic (saturated) permeability of the INCREASE06 interlock fabric and will be detailed in Chapter 4.

2.3.2.3 Measurement of the transverse permeability

Traditional in-plane permeability measurement methods are well tested and established. The same cannot be said for transverse permeability measurements. Specially for thick parts, the transverse permeability must be properly characterized.

Kim and Daniel [32] determined the three principal permeabilities of a reinforcement using an inverse parameter estimation technique. Later, Yun et al.[82] calculated the full permeability tensor of a thick 3D preform including the transverse skew terms by conducting a 3D flow experiment with a central injection gate and recording the top and bottom ellipses formed in a transparent RTM mold then matching the images to a simulated flow to extract the permeability tensor.

To date, only a limited number of studies have been published on the 3D permeability measurement of 3D fabrics. Umer et al.[2] and Endruweit et al.[19] measured the transverse permeability of an interlock fabric with a saturated unidirectional flow technique.

Weitzenbock et al [76] measured the full permeability of a reinforcement using a 3D radial flow test and pressure transducers. He observed that the permeability was influenced by the flow induced compaction and that the better option to obtain the transverse permeability is to use a steady-state (saturated) flow test.

2.4 Flow induced deformation

Increasing the fluid pressure during LCM process is a way to decrease the manufacturing cycle time of a part. However, if the fluid pressure is higher than the friction forces between the tows, due to the interactions of the fluid and solid phases, the tows can be transported by the fluid and the fiber reinforcement will be deformed. It is important to know the limiting factors in order to optimize the manufacturing time but also avoiding unwanted tow movement. In the C-RTM process, the mold closing speed $\dot{h}$ propels the resin into the fabric and controls the internal fluid pressure.

2.4.1 Compression of fiber reinforcements

Viscoelasticity

Reinforcement compression is an important step in many manufacturing processes. The compression deformation behavior of common LCM reinforcement has been studied by, among others, Bikerton et al.[6] and it showed that even without resin, the reinforcements have a viscoelastic response to transverse compression. Recently, an international benchmark exercise for the experimental characterization of the compaction response of a textile

was performed [81]. A quite large variation was observed that indicated the influence of the choice of experimental set-up for the compaction stress results.

Figure 2.9 shows the observed behavior for different compression modes.

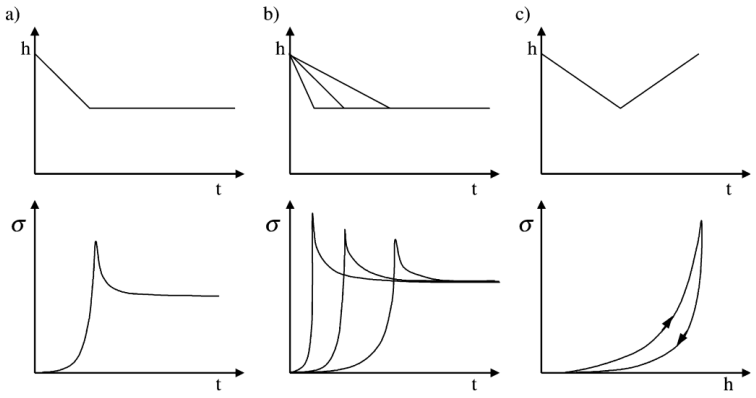

Figure 2.9: Viscoelastic behavior of fiber reinforcements under compression [6]

The stress relaxation (a) is the decrease of stress during compression once the final deformation is achieved. It occurs by the rearrangement of the fibers [27] and it is shown to majorly impact the compaction behavior [59]. Umer et al.[74] performed dry compaction experiments for different types of interlock fabrics and showed an immediate compaction stress drop after reaching the maximum value and also the influence of the different weaved architectures in the measurement of the compaction stress.

The processing parameter that has the strongest effect on the relaxation is the compression rate [58] and it was shown experimentally that the maximum stress increases with the augmentation of the compaction rate $\dot{h}$ (b) [31]. The loading/unloading of a fibrous reinforcement (cyclic loading) can generate a residual plastic deformation and an hysteresis response.

Lubrication

Some studies show that lubricating the fiber reinforcement with a low viscosity fluid can help its compression compared to dry state [31, 33]. Comas-Cardona et al. [16] performed transverse compression tests in both dry and lubricated twill fabrics. It was shown that the compression modulus of impregnated fiber reinforcements was lower in comparison to the dry ones. This can be explained since the fluid serves as lubricant decreasing the friction between the tows and facilitating the reorganization of the fibers.

2.4.2 Compression of saturated fiber reinforcements

Total stress constitutive equation

A fully saturated porous medium under compression follows Terzarghi's law [70] which states that the total stress response σ_z results from the combination of applied stress of the fibers σ_z^f and the hydrostatic fluid pressure P as given in Equation 2.7:

$$\sigma_z = \sigma_z^f + bP \tag{2.7}$$

with b as the Biot coefficient [8] described in Equation 2.8:

$$b = 1 - \frac{C_o}{C_s} \tag{2.8}$$

where C_o is the compression modulus of the porous medium and C_s the bulk modulus of the fibers.

Following Terzaghi's assumption $b = 1$, meaning that the fiber bulk modulus is higher than that of the reinforcement. Terzarghi's law allows to uncouple the behavior of the fluid and solid.

Kang et al. [30] showed that the saturated preform response to compression is higher than the dry and lubricated states and that the experimental fluid force F_{fluid} can be extracted by subtracting the lubricated fiber reinforcement $F_{\text{lub.}}$ contribution from the total applied force F_{tot} :

$$F_{\text{fluid}} = F_{\text{tot}} \ - F_{\text{lub.}} \tag{2.9}$$

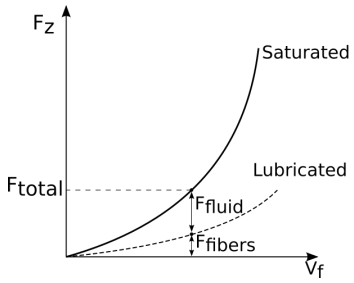

Figure 2.10: Compression response of a saturated fabric

The internal fluid pressure P in Equation 2.7 or F_{fluid} in Equation 2.9 is shown to increase with the augmentation of the fluid viscosity μ and compression speed $\dot{h}$ [16, 28].

2.4.3 Fluid flow in porous media

The phenomenon of fluid flow in deformable porous media is encountered in various engineering fields, including soil science and biomechanics. Methods developed in these disciplines have been effectively utilized in studies related to composite processing. Michaud et al. [45, 46] highlights the phenomena that governs the consolidation of a compressible preform and the influence that fluid viscosity, stress-strain behavior, saturation and permeability may have on the process.

Darcy's equation (Equation 2.1) describes the resin flow thought the fibrous reinforcement. We must keep in mind that $\boldsymbol{u_D}$ (Darcy's velocity) is the volume averaged flow velocity and $\boldsymbol{v_l}$ is the pointwise fluid velocity inside the pores (Figure 2.11). Darcy's velocity is obtained by the phase averaging of the pointwise velocity as [73]:

$$< \boldsymbol{v_l} >= \boldsymbol{u_D} = \frac{1}{\Omega} \int_{\Omega_l} \boldsymbol{v_l} d\Omega \tag{2.10}$$

where Ω is the total volume occupied by the fluid and fibers $\Omega = \Omega_l \cup \Omega_s$

When a saturated fibrous bed is compressed, Darcy's velocity is express as the difference between the intrinsic velocities of the fluid and solid phases.

$$< \boldsymbol{v_l} > - < \boldsymbol{v_s} >= -\frac{\mathbf{K}}{\mu\phi}\nabla P \tag{2.11}$$

The intrinsic velocities are defined by:

$$< \boldsymbol{v}_l^l >= \frac{1}{\Omega_l}\int_{\Omega_l} \boldsymbol{v_l} d\Omega_l \tag{2.12}$$

Both phase averaged and intrinsic phase velocities are related by the porosity as shown:

$$\phi < \boldsymbol{v_l}^l >=< \boldsymbol{v_l} > \tag{2.13}$$

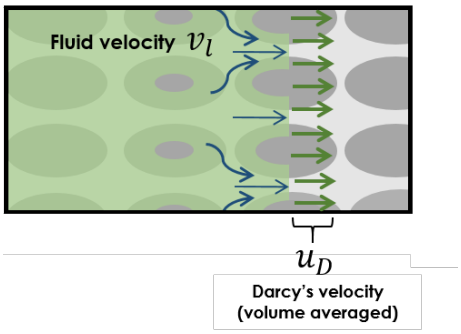

Figure 2.11: Representation of intrinsic fluid velocity $\boldsymbol{v_l}$ and Darcy's velocity $\boldsymbol{u_D}$

Assuming that the reinforcement only deforms in the transverse direction but is rigid in-plane, Pham [52] defined the continuity equation of a flow in a transversely deformable reinforcement for the C-RTM process from the conservation of both solid and liquid phases:

$$\dot{h} = \nabla.\left(h\frac{\boldsymbol{K}}{\mu}\nabla P\right) \tag{2.14}$$

where $\dot{h}$ is the mold closing speed and h the preform thickness. Hautefeuille et al. [28] integrated Equation 2.14 in cylindrical coordinates for the use of a circular compression platen with boundary condition $P(r) = 0|_{r=R}$ and $\frac{\partial P}{\partial r} = 0$ as seen in Figure 2.12:

$$P(r) = -\frac{\mu\dot{h}}{4hK_e}(R^2 - r^2) \tag{2.15}$$

The fluid F_{fluid} force can be then found by integrating Equation 2.15:

$$F_{fluid} = \int_0^R 2\pi P(r)dr = -\frac{\mu\dot{h}\pi R^4}{8K_e h} \tag{2.16}$$

In the case of a 3D flow analysis, Gutowski [24] developed the consolidation equation for an anisotropic material in cartesian coordinates (x, y, z):

$$K_x\frac{\partial^2 P}{\partial x^2} + K_y\frac{\partial^2 P}{\partial y^2} + K_z\frac{h_0^2}{h^2}\frac{\partial^2 P}{\partial z^2} = -\mu\frac{\dot{h}}{h} \tag{2.17}$$

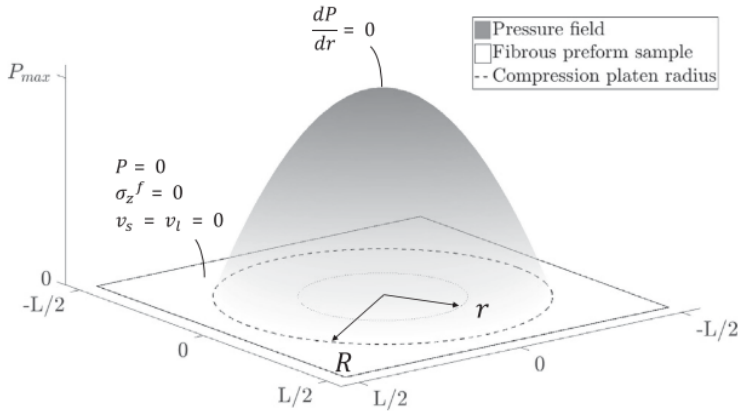

Figure 2.12: Pressure field from the resolution of Equation 2.14 with boundary conditions $P(r = R) = 0$ and $\frac{\partial P}{\partial r} = 0$ at $r = 0$ [28]

where K_x, K_y and K_z are the permeabilities in the x,y,z direction and h_0 is the initial thickness of the fabric

For the application of a circular compression platen, the consolidation equation is reduced in cylindrical coordinates:

$$\frac{K_e}{r}\frac{\partial}{\partial r}\left(r\frac{\partial P}{\partial r}\right) + K_z\left(\frac{V_f}{V_f^0}\right)^2\frac{\partial^2 P}{\partial z^2} = -\mu\frac{\dot{V}_f}{V_f} \tag{2.18}$$

Where K_e is the in-plane permeability and its equivalent to $\sqrt{(K_x K_y)}$

2.4.4 Fluid-solid interactions

Tucker and Dessenberger [73] defined the fluid-solid drag force $\mathbf{f}_d$ as the difference between the total interaction force $\mathbf{f}_T$, the forces due to the average fluid effective pressure $\mathbf{f}_p$ and the force by a gravity-induced pressure gradient $\mathbf{f}_g$ applied to a representative volume V with a fluid-solid interface surface S_{fS} :

$$\mathbf{f}_d = \mathbf{f}_T - \mathbf{f}_g - \mathbf{f}_p = -\frac{1}{V}\int_{S_{fS}} \sigma_f \cdot \mathbf{n}_{fs} dS - \frac{1}{V}\int_{S_{fS}} \rho_f g H \mathbf{n}_{fs} dS - < P_f >^f \nabla\phi \tag{2.19}$$

where $\sigma_f \cdot \mathbf{n}_{fs}$ is the traction exerted by the fluid on the solid, H the height above the reference level, g is the gravity acceleration, $< P_f >^f$ the fluid pressure, and $\nabla\phi$ the porosity gradient in the volume V.

2.4.5 Drag force $\mathbf{f}_d$

Slattery et al. derived the drag force $\mathbf{f}_d$ of a single-scale isotropic porous media [66] into the constitutive equation:

$$\mathbf{f}_d = \phi\mu\mathbf{K}^{-1}[< \boldsymbol{v}_l^l > - < \boldsymbol{v}_s^s >] = \phi\nabla P \tag{2.20}$$

Later Pillai [55] showed that the double-scale behaves like a single-scale porous media for the estimation of viscous drag force since the flow inside the tows is very small in comparison to the inter-tow flow.

2.4.6 Flow-induced deformation

Darcy's law describes the flow of a Newtonian fluid through a rigid (non-deformable) porous media. LCM processes, particularly the ones that produce an elevated internal fluid pressure for faster impregnation such as the RTM and C-RTM can end up deforming the fiber reinforcement. Aimé showed that there is a limiting injection pressure that can be used for RTM process. If this pressure is exceeded, flow-induced deformation occurs, leading to a significant local pressure drop [1]. Michaud and Månson [47] showed that during the impregnation of fiber mats, the fluid flow causes a significant compression of the fibrous reinforcement, followed by a long relaxation.

Previous studies have focused on investigating fiber washout during the RTM process (with constant cavity thickness). Richardson and Zhang investigated this phenomenon and established a correlation between washout and injection time. They also found that increasing the clamp force significantly improves fiber washout [57]. Similarly, Endruweit et al. [20] conducted visual observations of flow-induced deformation and quantified the maximum critical injection pressure for deformation as a function of the clamp force.

The friction between tows and mold needs to be higher than the viscous-drag forces to avoid fiber washout. Seong et al [62] measured the friction coefficients and observed the flow induced deformation in real time while also measuring the pressure and displacement of the tows during injection (Figure 2.13). It was confirmed that the deformation occurred when fluid force was larger than the friction between the fiber and the mold.

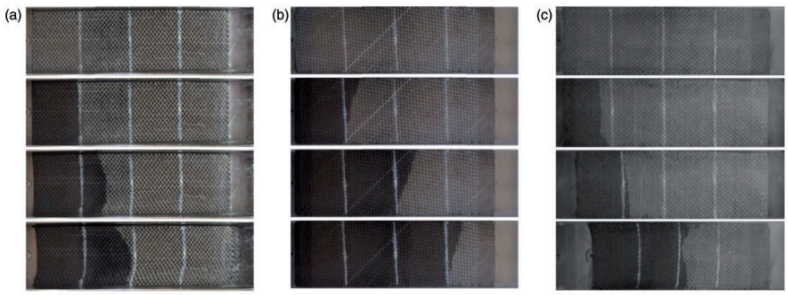

Figure 2.13: Flow induced deformation of a UD fabric injected at a orientation angle of: (a) 0°, (b) 45° and (c) 90° [62]

Hautefeuille et al.[27, 28] implemented a methodology to detect the occurrence of fiber washout during the compression of a saturated fibrous reinforcement. This methodology does not need the visualization of the flow nor post-consolidation observations. He compared the theoretical force derived from Darcy's law for static fibrous beds (Equation 2.4.3) and the experimental fluid force given by Equation 2.9.

Several compression tests were conducted using a 2D glass woven fabric impregnated with silicone oil with viscosities varying from $\mu = 0.09$ to $\mu = 9.63$ Pa.s. The results showed that under iso-speed conditions, the measured experimental fluid force aligns with the theoretical model (assuming the reinforcement to be rigid in-plane) when the viscosity is below 1 Pa.s (Figure 2.14 (a)). However, for higher viscosities, the experimental fluid forces deviate from the Darcian model (Figure 2.14 (b)), indicating a correlation between increased fluid pressure and the occurrence of deformation.

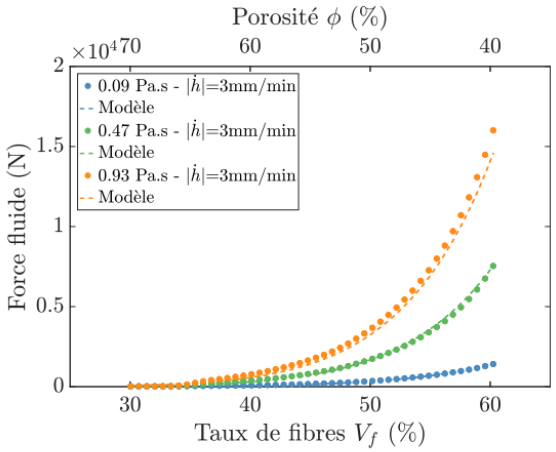

(a) $\mu = 0.09$, 0.47 et 0.93 Pa.s, $\dot{h} = 3$ mm/min

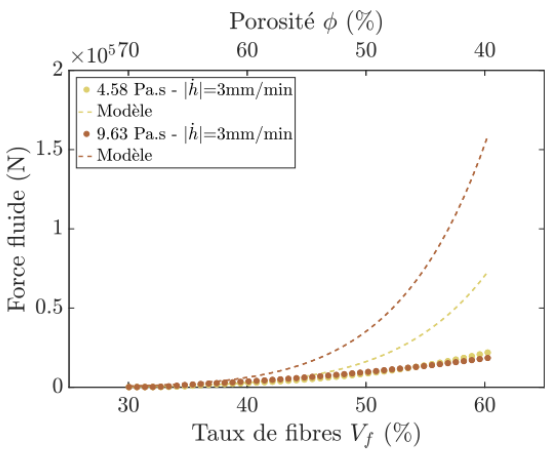

(b) $\mu = 4.58$ et 9.63 Pa.s, $\dot{h} = 3$ mm/min

Figure 2.14: Comparison between the theoretical and experimental fluid force for (a) lower viscosity ($\mu = 0.09$ Pa.s, 0.47 Pa.s and 0.93 Pa.s) and (b) higher viscosity ($\mu = 4.58$ Pa.s and 9.63 Pa.s at a compaction speed of $\dot{h}$= 3 mm/min) [27].

To better understand the nature of the deformation measured experimentally he then dynamically and optically tracked the in-plane motion of the tows during compression and compared it to the saturated compression test results.

The Figures 2.15 (a) and (b) show the in-plane tow displacement for the low and high fluid viscosity cases respectively. No considerable tow motion is observed for $\mu = 0.09$ Pa.s and the displacement is uniform (a). However, for $\mu = 4.58$ Pa.s we can observe tow motion of around 16 mm close to the edges of the sample (b).

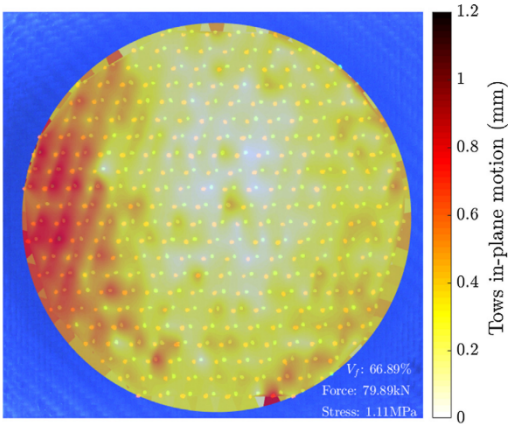

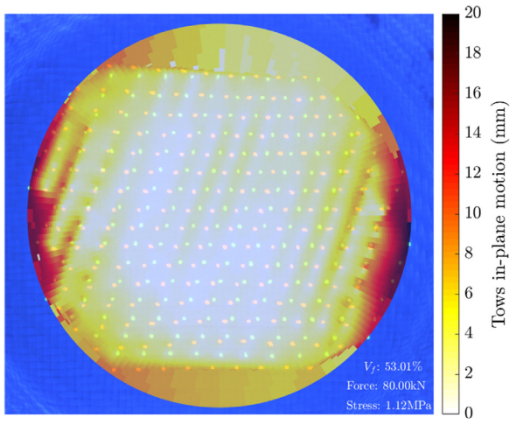

Figure 2.15: In-plane fiber-tow displacement field at the end of the consolidation: $\dot{h}$= 3 mm/min, $\mu = 0.09$ Pa.s (left) and $\dot{h}$= 3 mm/min, $\mu = 4.58$ Pa.s (right) [28].

2.5 Saturation measurement

Darcy's law (Equation 2.1) was established under certain conditions: laminar flow through a saturated granular media. The bulk permeability K is the saturated permeability [10, 46] intrinsic to the geometry of the porous medium, however, the porous medium used in LCM (fabric reinforcement) does not saturated instantaneously during the injection due to differences in pores sizes. Discrepancies between the model and what is observed

experimentally will happen if the degree of saturation is not taken into account.

2.5.1 Dual scale flow

Differently from the porous media studied by Darcy in soil mechanics, textile-based composites materials have two different pore sizes: the space within the individual tows, which is on the scale of micrometers, and the space between the tows, which is on the scale of millimeters (Figure 6.1). Because of this three orders of magnitude difference, the saturation does not happens instantaneously during the injection.

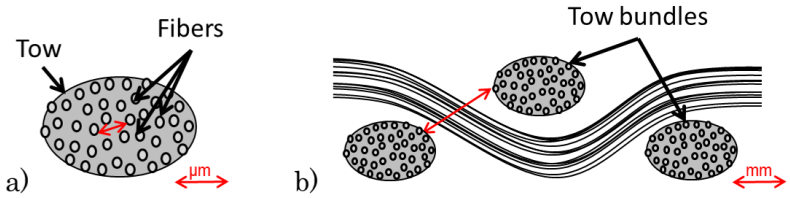

Figure 2.16: Schematic representation of (a) micropores between fibers and (b) mesopores between tow bundles

The filling pattern of a dual-scale flow depends on the relation between the viscous and capillary forces represented by the capillary number C_a:

$$Ca = \frac{\mu u_D}{\gamma} \tag{2.21}$$

where u_D is Darcy's velocity, μ is the fluid viscosity and γ the fluid surface tension.

At a lower impregnation speed (low Ca), the fluid is primarily governed by capillary forces, leading to the preferential filling of spaces within the tows. However, at higher impregnation speeds (high Ca), which is typically encountered in most LCM processes, the fluid flow is predominantly driven by viscous forces, resulting in the initial filling of the spaces between the tows. This can lead to inadequate impregnation of the tows themselves, as micro-pores within the tows may not be effectively filled.

Due to the double scale nature of the fabric, the visual observation and measurement of the flow front, which is typically used to calculate the permeability, do not necessarily indicate full saturation and therefore the permeability measured wont be the intrinsic saturated permeability but the unsaturated one. The difference between the two can distort significantly the analysis of the resin flow during injection [10]. Figure 2.17 shows that the saturated flow front comes after in the sense of the injection but it is not easily identifiable.

2.5.2 Saturation measurements techniques

The saturation S is defined by the ratio between the volume of fluid V_{fluid} and the total pore volume V_{total} of a given representative volume of interest and of porosity ϕ.

$$S = \frac{V_{fluid}}{\phi V_{\text{total}}} \tag{2.22}$$

Michaud [44] reviewed the experimental techniques used to measure the time-dependent saturation profile during injection. For translucent fabrics such as glass fiber reinforcements, Lebel et al. [38] uses visible light transmission to measure the real-time

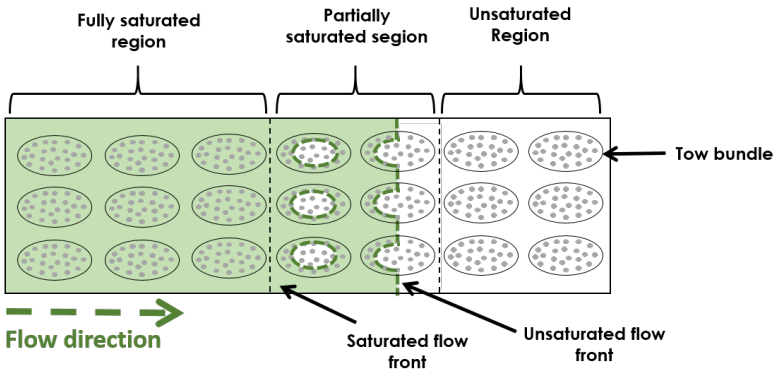

Figure 2.17: Schematic of unsaturated and saturated flow front during unidirectional injection

impregnation and void content. Direct image analysis have also been used when the flow visualization is possible [49, 64].

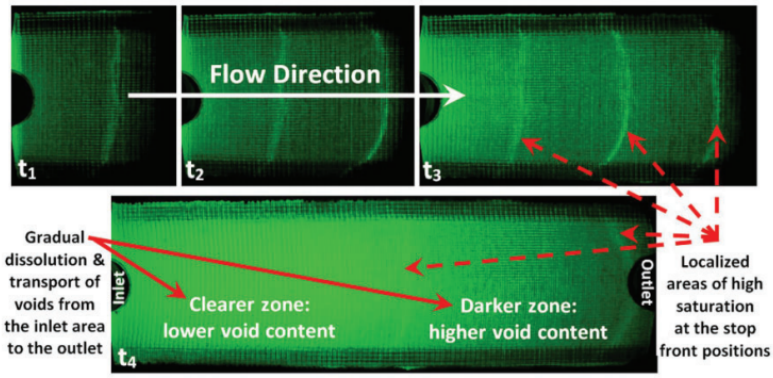

Figure 2.18: Flow during an RTM injection of a fiberglass reinforcement, the darker areas are less saturated [38].

Since the INCREASE06 interlock is made out of carbon fibers, direct optical monitoring of the flow is not possible. Recently, Pedarròs [69] used an in-situ X-Ray phase contrast technique to observe the flow progression through translucent and also non-translucent preforms such as carbon fiber preforms (Figure 2.19).

Labat et al.[36] used an conductivity sensor to measure blindly the saturation of the porous media using the difference in electrical conductivity between liquid air and fibers. Later, Guéroult et al. [23] adapted the sensor to measure the change in the impedance due to the change of dielectric properties during the impregnation of a fabric.

To measure the saturation of INCREASE06 fabric at various fiber volume fractions, the experimental set-up needs to meet specific requirements. It should be capable of producing elevated pressure (tens of bar) to compress the fabric while also allowing for the measurement of saturation in a non-translucent fabric. The dielectric sensor proposed by Guéroult et al. will be adapted for this particular case with appropriate electrical insulation and installed in an universal testing machine used for the compression of the fabric.

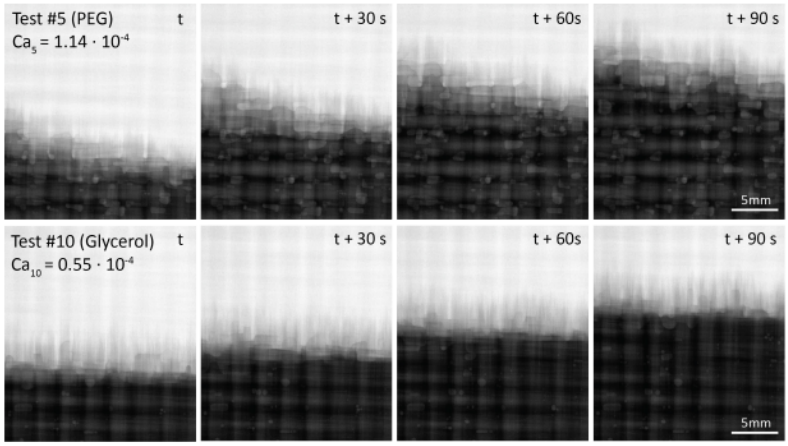

Figure 2.19: Fluid distribution of a twill carbon reinforcement using X-Ray absortion imaging [69]

2.5.3 Dielectic measurements

A dielectric sensor uses capacitance which is proportional to the dielectric permittivity of a surrounding medium. Capacitance C is the capability of a material to store electric charge. The capacitance is defined by the relationship:

$$Q = CV \tag{2.23}$$

Where Q is the is the charge in each capacitor and V the electric potential between plates. The capacitance is affected by geometric factors such as distance d between plates and the area A of the plates (Figure 2.20) and also the permittivity ε of any dielectric material between them.

$$C = \varepsilon \frac{A}{d} \tag{2.24}$$

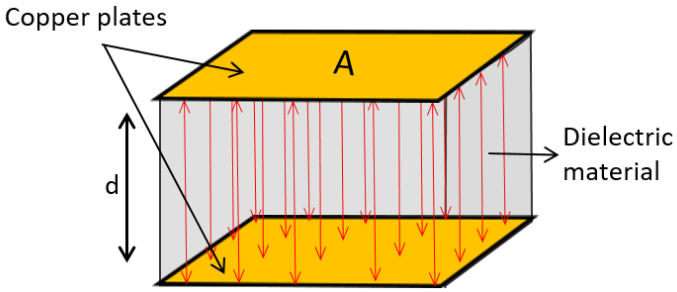

Figure 2.20: Parallel plate dielectric sensor with plate surface A and distance between plates d.

Permittivity ε express the ability of a material to polarize in response to an applied electrical field as seen in Figure 2.21. A higher permittivity allows the material to polarize more in response to the electrical field, therefore storing more energy in the material.

The relative permittivity ε_r, also known as the dielectric constant is the ratio of the permittivity of the dielectric material in relation to the permittivity of the vacuum ε_0.

$$\varepsilon_r = \frac{\varepsilon}{\varepsilon_0} \tag{2.25}$$

where $\varepsilon_0 = 8.854 \times 10^{-12} \frac{F}{m}$

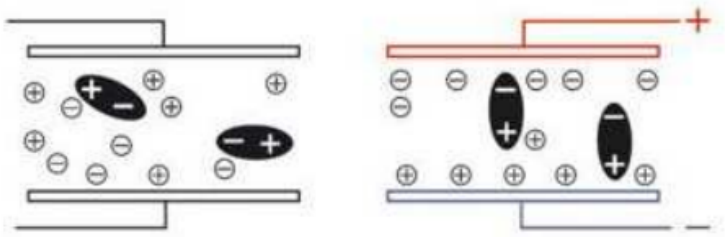

Figure 2.21: Dielectric medium showing the orientation of particles when unpolarized (left) and polarized by an electric field (right) [23].

The relative permittivity ε_r varies in alternating fields. As frequency increases, the polarization of the material (ε_r) drops since the dipoles do not have enough time to switch orientation as fast as the alternating field [50]. To measure the dielectric properties of a material, a frequency below the time for the dipole to adjust its orientation (relaxation time) is preferable (below 10^9 Hz as seen in Figure 2.22).

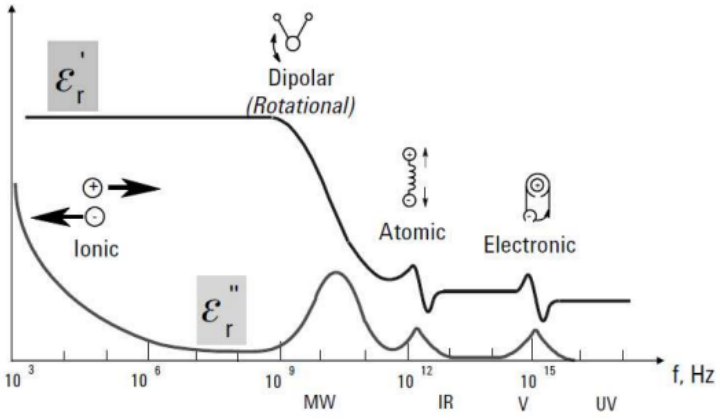

Figure 2.22: Evolution of permittivity ϵ_r in function of the frequency. ϵ_r' and ϵ_r'' represent the real and imaginary part of the permittivity respectively [23].

Chapter 6 provides a comprehensive description of the experimental setup designed for measuring the time-dependent saturation of the INCREASE06 interlock during injection using parallel plate dielectric sensors.

2.6 Conclusion and research plan

The use of 3D fabric reinforcements brings many performances advantages such as better transverse strength and reduced risk of delamination and so, they are good options for the manufacturing ot thick aeronautical parts. However, investigations regarding the characterization of such fabrics are limited. The permeability is an important tensorial parameter for the simulation of the flow therefore the experimental characterization of the fabric must be done with care. Due to the elevated thickness of interlock and 3D fabrics, the transverse permeability is of great importance for the simulation of the filling during

C-RTM. Both in-plane and transverse permeabilities need to be measured at various stages of compaction.

The non-translucent carbon fibers make the flow visualization difficult without added enhancement. An alternative must be encountered for the visualization of the radial flow front. The traditional permeability measurement techniques must be adapted in consideration of the specificity of the fabric.

In comparison to traditional RTM, the C-RTM process produces a higher internal fluid pressure at the latest staged of compression and also deforms transversely the reinforcement during compression. If the fluid pressure is higher than the friction between the tows, the fluid flow can displace and deform the original geometry of the reinforcement. If deformation happens, the nominal measured permeability is no longer valid and the desired mechanical properties will not be as expected because of the local gradients of tow orientations and of fiber volume fractions.

The presence of dense and twisted tows while also having large inter-tow space makes it particularly challenging to impregnate the interlock fabric. It was observed industrially that after the arrival of the resin to the vents, the fabric and specifically the intra-tow volume were still not fully saturated. While the intrinsic permeability depends only on the geometry of the fabric, an unsaturated permeability might vary in function of the degree of saturation [10]. It is important then to better understand the impregnation mechanisms and time necessary to achieve full impregnation of a part.

The objectives of this study can be divided in industrial and scientific :

Industrial:

- Experimental characterization of the evolution of the permeability tensor $\mathbf{K}$ in order to support simulation of C-RTM process.
- Creation of a processing window for the INCREASE06 interlock during C-RTM to limit the internal fluid pressure and avoid a textile architecture deformation.
- Measurement of the necessary time to fully saturate a region during injection.

Scientific:

- Detection of on-site flow-induced deformation and the mechanical signature during compression of the INCREASE06 interlock.
- Comparison between unsaturated and intrinsic permeability measured using different techniques.
- Experimental and numerical measurement of the unsaturated length during injection at different V_f

In order to achieve the above objectives, the following chapters will cover different parts of the INCREASE06 characterization (Figure 2.23):

Chapter 3: Describes the materials used in this study and the how to properly condition the samples for the different tests.

Chapter 4: Presents the experimental techniques used to characterize the permeability of the INCREASE06 fabric for the C-RTM process, therefore considering the permeability evolution during compression. The specificity of the fabric such as elevated stiffness makes it necessary the use of particular machinery that can apply tens of bar to reach the desired fiber volume fraction. Both in-plane and traverse permeability are equally important since the fabric has an elevated through thickness and transverse binding yarns.

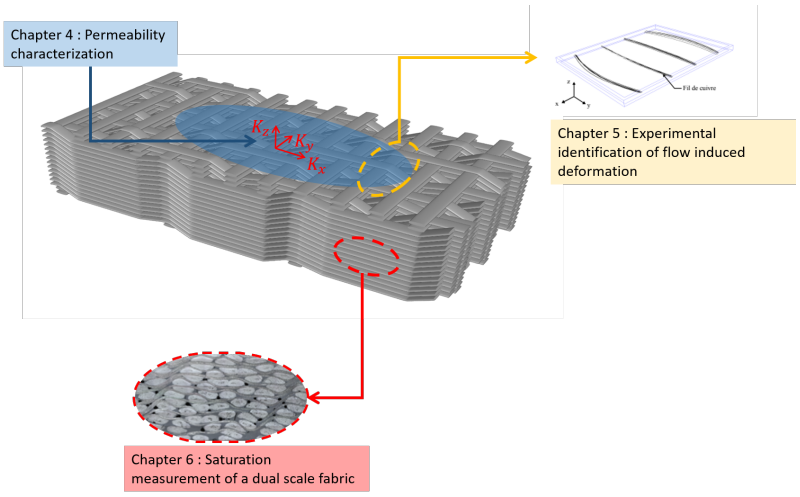

Figure 2.23: Charaterization plan of INCREASE06

A measurement protocol is proposed to be able to fully characterize the fabric using the least amount of material.

Chapter 5: This chapter identifies the occurrence of flow induced deformation due to an elevated fluid pressure that can occur during the C-RTM process. The interlock INCREASE06 behavior is compared to well studied traditional twill and quasi-UD fabrics. The deformation is identified when the experimental fluid pressure deviates from the theoretical quasi-static model. A processing window is created for the C-RTM process in which the closing mold speed $\dot{h}$ can be chosen for a particular resin with viscosity μ.

Chapter 6: This chapter describes the development of a sensor to measure the evolution of the saturation profile over time during injection of the INCREASE06 interlock. The saturation sensor uses dielectric measurements and its installation is adapted for the compression of the fabric at various V_f. The unsaturated length of the fabric and the time to fully saturate the sensor region are measured. Numerical simulations are run on a simplified geometry with representative tow proportions to understand the influence of unbalanced-sized tows have on the saturation evolution during injection.

Chapter 3

Materials and sample conditioning

This chapter provides an overview of the materials used in this study. Firstly the fabrics are introduced: the interlock fabric of interest that will be characterized. Additionally, we present the other fabrics that were extensively examined and will serve as points of comparison. Subsequently, we discuss the model fluids used in the tests and considerations regarding the conditioning of the samples.

Contents

3.1 Fabrics used in the study

3.1.1 Interlock

The fabric that will be characterized in this study is a layer-to-layer carbon interlock produced by Safran composites. It is an unbalanced fabric, with 64.4% of fiber tows are in warp direction and 35.6% are in weft direction (RCT:*Ratio chaîne/trame* seen on Table 3.1).

Two different geometries were provided initially for this study: Figure 3.1 shows the difference between the weaving pattern of the geometry named INCREASE 02 and INCREASE 06. This pattern was use to create a 3D representation of both fabrics using the geometric textile modeling software TexGen (Figure 3.2). The INCREASE06 geometry will be the only fully characterized due to limited sample availability of the INCREASE02 geometry.

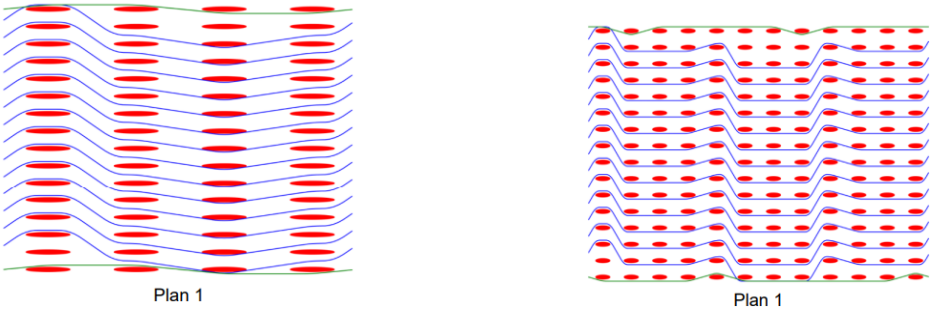

(a) (b)

Figure 3.1: Weaving plan of INCREASE02 (a) and INCREASE 06 (b) provided by Safran composites

(a) (b)

Figure 3.2: 3D model representation of INCREASE 02 (a) and INCREASE 06 (b) - made with TexGen

More details about the geometry and the tows used in the manufacturing of the both interlock geometries can be seen in Table 3.1

The surface mass density of both geometries were measured. The surface mass A_w is calculated as mass per unit area where m is the fabric's sample weight and A_e is the surface area of the sample:

$$A_w = \frac{m}{A_e} \tag{3.1}$$

Warp density (thread/cm)	2.36
Weft density (thread/cm)	2.61
RCT	64.4/35.6
Warp thread	48K IM7
Weft thread	24K IM7
Number of plies	16

Table 3.1: INCREASE02 and INCREASE06 manufacturing parameter - provided by Safran composites

The measured surface mass of the INCREASE02 and INCREASE06 were A_{w02}=11264 g/m^2 A_{w06} = 11184 g/m^2 respectively.

For comparison, two extensively studied conventional fabrics were employed: An isotropic twill and quasi-UD fabric. These fabrics, readily available within the laboratory, will serve as reference points for evaluating the mechanical characteristics observed in the interlock fabric.

3.1.2 Isotropic fabric

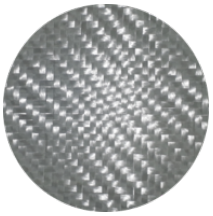

A 2D glass woven fabric G-Weave 600T PA produced by Chomarat was studied in depth by Hautefeuille at al. [27] and used as comparative. The surface mass provided by Chomarat is of A_w=600 g/m^2 with a balanced distribution between weft and warp (300 g/m^2 on each direction)

The permeability of the G-Weave 600T PA was calculated by Hautefeuille using the saturated compression technique developed by Comas-Cardona et al. [15]. This method allows to measure the in-plane equivalent permeability K_e evolution during compression. Figure 3.3 represents the in plane permeabilty of the fabric for a fiber volume fraction range of $35\% < Vf < 65\%$.

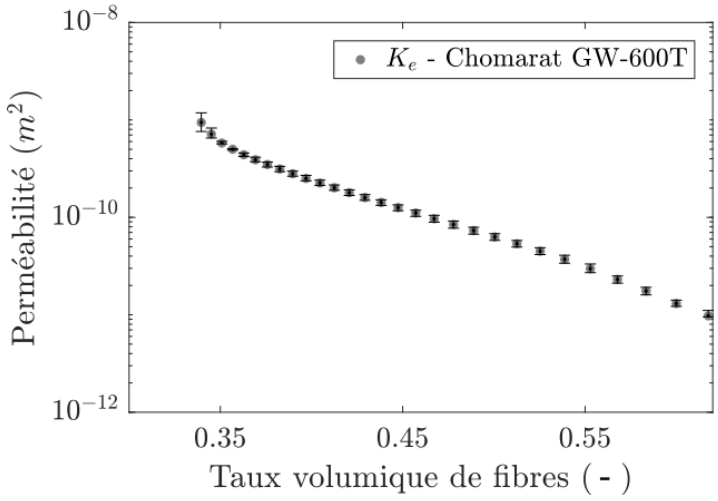

Figure 3.3: Equivalent permeability K_e of fabric G-Weave 600T PA [27]

3.1.3 Anisotropic fabric

The anisotropic fabric that will be used for the anisotropic permeability measurements is a UDT 400P produced by Chomarat. It has a unbalanced distributed structure (quasi-UD). The surface mass density provided by Chomarat is of A_w = 420 g/m^2 with 410 g/m^2 distrubted on the weft and 10 g/m^2 on the warp.

The permeability was calculated using the method described by Martin et al. [41] in which you can extract the permeability in the direction of the weft (K_x) and the warp (K_y) during compression. Figure 3.4 shows both the principal in-plane permeabilities of the fabric for a fiber volume fraction range of 40 % $< Vf <$ 60%.

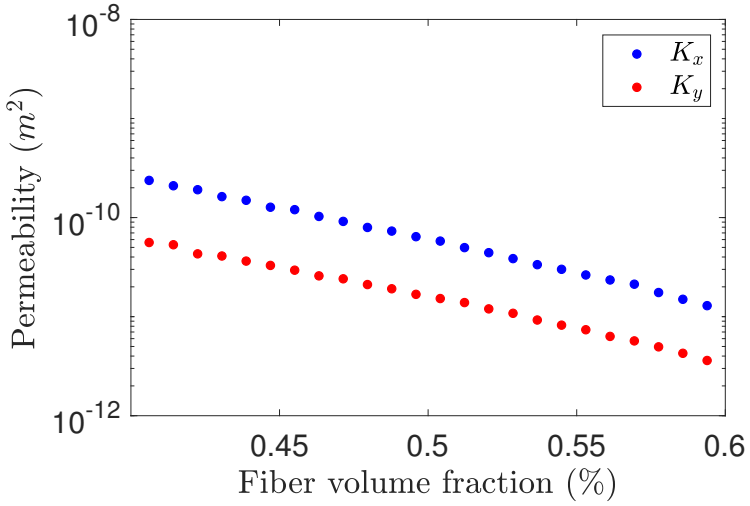

Figure 3.4: Permeability evolution of UDT 400P

3.1.4 Glass interlock

A glass Injectex 3D fabric was used for the dielectric sensor validation. Since the fabric is made of glass fibers, it allows the flow front visualization necessary for the sensor validation while also having an elevated dual scale behavior.

3.2 Fluids

Two model fluids were used for the impregnation of the fabrics in lieu of resin. Silicone oil was used for the saturated compression technique and a mixture of glycerol and water was used for the radial injection and dielectric measurements.

3.2.1 Silicone oil

The model fluid used in the continuous saturated compression experiments was silicone oil produced by Carl Roth. The viscosity range used on the experiments is described on Table 3.2:

Reference	Density (g/cm³)	Viscosity range (Pa.s)	Melting point (°C)
Silicone oil M 100	0.97	0.095-0.105	-55
Silicone oil M 500	0.97	0.475-0.525	-55
Silicone oil M 1000	0.97	0.95-1.05	-55
Silicone oil M 5000	0.98	4.75-5.25	-50
Silicone oil M 10 000	0.98	9.5-11	-50

Table 3.2: Silicone oil specifics - *https://www.carlroth.com*

3.2.2 Glycerol

The fluid used for the radial injection test was made using a mixture of Glycerol, water and fluorescent pigment (produced by Sennelier) to increase the contrast to the UV-light. The pigment concentration was 1.5% of mass and later water was added to decrease the fluid viscosity in the proportions seen on Table 3.3:

Water %	Viscosity (Pa.s) @ 24.3 ° C
0.82	1.3
2.6	0.63
3.2	0.57

Table 3.3: Glycerol + pigment (1.5% of mass) water concentration

Glycerol was also used for the dielectric measurements due to its higher relative permittivity ϵ_r. For the sensor validation (using the glass Injectex 3D fabric), pure glycerol (μ = 1.412 Pa.s at 20°C) was used with added violet pigment to increase the visual contrast of the test (Figure 3.5 (b)). The dielectric measurements of the INTERLOCK06 were made using a mixture of glycerol and 14% in weight of water to increase its ϵ_r and decrease fluid viscosity μ.

(a) Fluorescent pigment: Sennelier 502

(b) Violet pigment: Sennelier 909

Figure 3.5: Pigments used in the study

3.3 Sample conditioning

The saturated compression test is highly sensitive to the degree of saturation of the fabric, to ensure good repeatability of the test, the samples must be uniformly and adequately impregnated. A benchmark exercise to measure the compaction response of both wet and dry textiles showed that the wetting of the specimen significantly affected the scatter in results [81].

Open geometries with dense tows such as the interlock, cannot retain the injected fluid so to unsure good impregnation fluid loss must be avoided while setting up for the experiment. The most practical solution is to keep the fabric immersed in a bath of fluid until its ready to be compressed. The impregnation protocol is described as follows:

- The fabric is fully immersed in a container filled with fluid.
- The container is placed in a vacuum chamber overnight for degassing.
- The container is used to transport the sample and the fluid until it is time to be compressed, making sure the sample is always submerged.
- The sample and the fluid are then transferred to the receptacle where it is compressed using the universal testing machine.

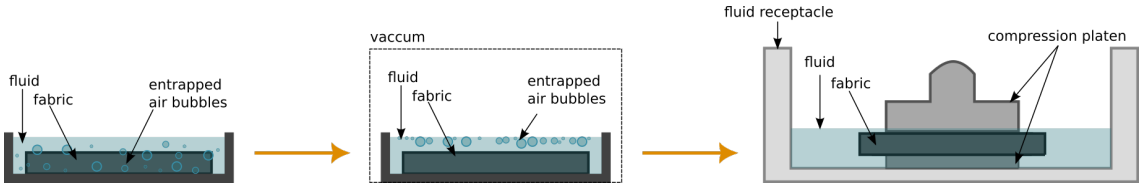

Figure 3.6: Impregnation protocol for saturated compression

The overnight degassing of the samples improved greatly the impregnation inside the tows. Entrapped air bubbles can be seen being expelled during compression of a seemingly well impregnated that was put into the vacuum chamber (Figure 3.7 (a)). Almost no air bubbles were left on the sample that was degassed overnight as seen on Figure 3.7 (b).

3.4 Conclusion

This chapter introduced the fabric that will be the subject of this study: a carbon layer-to-layer interlock produced for the INCREASE project by Safran composites. Three commercial fabrics were also introduced and will be used as comparative to the behavior observed with the interlock:

- An isotropic glass twill fabric G-Weave 600T PA produced by Chomarat that will be used during the saturated compression tests for the measurement of the in-plane equivalent permeability.
- An anisotropic quasi-UD glass fabric UDT 400P produced by Chomarat that will be used during the saturated compression tests for the measurement of permeabilities in the direction of the warp and weft (K_x and K_y respectively)

The mechanical signature of both fabrics when flow induced deformation occurs will also serve as comparative as described in Chapter 5.

This chapter also describes the model fluids that were used and the particular care that must be taken to properly prepare the samples for compression. Table 3.4 summarizes the materials used for each experiment.

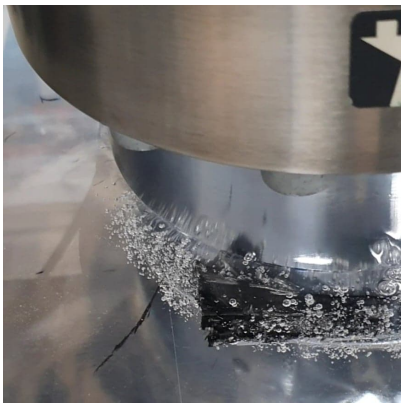

(a) Sample immersed in fluid overnight

(b) Sample immersed in fluid + degassing

Figure 3.7: Saturated samples being compressed ($\dot{h}$ = 6 mm/min and μ = 1 Pa.s)

Test	Fabric	Fluid	Viscosity range (Pa.s)	№of plies	Pigment
Saturated Compression	Interlock	Silicone	0.01-10	1	×
	Twill		0.01-5	6	
	quasi-UD		0.01-5	6	
Radial Injection	Interlock	Glycerol + water	0.53-1.07	1	Sennelier 502
Dieletric Measuement	Interlock	Glycerol + 14% water	0.17	1	×
	Injectex	Glycerol	1.4	10	Sennelier 909

Table 3.4: Materials used in the all experiments

Chapter 4

Permeability

This chapter will present the experimental techniques used to characterize the permeability of the INCREASE interlock geometries. The traditional permeability methods were adapted considering the specificity of a stiff carbon fiber reinforcement with elevated thickness. Later, a measurement protocol is proposed to be able to fully characterize the permeability tensor in a practical and material saving manner.

Contents

4.1 Introduction

The main objective of this chapter is to develop a reliable, easy to implement and material-saving technique to characterize the permeability of a thick interlock fabric for the C-RTM process.

Due to the particularities of this fabric, traditional permeability measurement techniques need to be revised and adapted in order to be implemented. Because of its elevated thickness and internal structure, several tens of bar are needed to compress the interlock to the desired fiber volume fraction (up to 50% of its initial thickness) making necessary the use of specific equipment suitable to apply such pressure. The production cost of complex 3D weaved fabrics such as the Interlock is elevated so the desired permeability measurement protocol is also conservative with a target of minimizing the total amount of material necessary for a complete characterization.

Elevated thickness also means that not only the in-plane permeability is important but also the through-thickness permeability needs to be measured. The complex open geometry may cause the permeability tensor to deviate from the fabric's main directions (weft, warp) and but also any transverse deviation must be investigated in order to fully characterize the permeability tensor.

First, a radial injection technique will be presented in order to calculate the in-plane permeability at a desired fiber volume fraction and also to measure the flow deviation angle. An easier to implement alternative is also described for industrial application.

Then, to measure both the transverse permeability and the continuous in-plane equivalent permeability, a saturated compression technique is used. This technique allows to continuously measure the evolution of the permeability during compression (comparable to what happens during the C-RTM process). It is a practical technique that can measure the permeability both in-plane and transverse with 3 experimental configurations. It should minimize the amount of fabric necessary for the characterization since it covers the whole fiber volume fraction range.

4.2 Radial injection

When a fabric is injected through a gate perforated in the center of a platen, the flow will spread radially impregnating the preform in a circular or elliptical shape. If the preform is isotropic, the flow front profile is circular and as anisotropy increases the major to minor axes ratio also increases [77] (Figure 4.1).

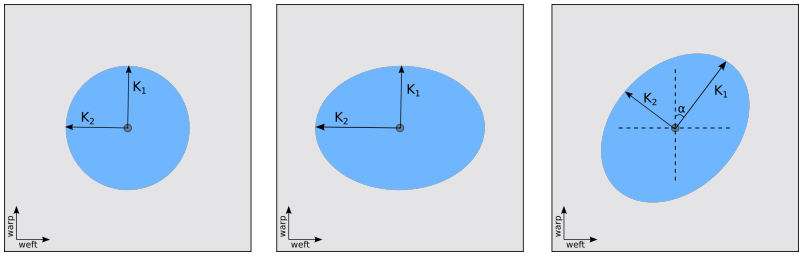

Figure 4.1: Radial flow front of an isotropic (a), anisotropic (b) and an anisotropic fabric with non-zero skew terms (c)

The ellipses' major and minor axes are proportional to the in-plane permeability and the axes are align with the principal directions of the flow. If the principal direction of the flow coincides with the material's principal direction (weft and warp) then the permeability

of the weft and warp directions can be measured directly. If there is a deviation (non-zero skew terms) then the deviation angle α with respect to the material principal directions (x,y) must be measured. Figure 4.2 is a scheme that represents the material main direction (x and y) and the flow main directions (1 and 2) deviated by α degrees in plane.

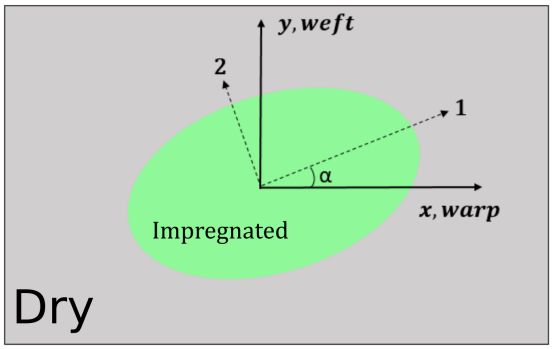

Figure 4.2: Schematic of an anisotropic radial front flow profile deviated in the plane by an angle α

4.2.1 In-plane permeability calculation

Weitzenbock [77] proposed a methodology to obtain the two in-plane permeabilities in the material principal direction (x,y) by measuring the flow front position at a time t. Equations 4.1 and 4.2 provide the in-plane permeability in the principal axis directions. Both equations were derived integrating Darcy's law and the conservation of fluid in 2D cartesian coordinates when there is no in-plane deviation:

$$K_x = \left\{ x_f^2 \left[2 \ln \left(x_f / x_o \right) - 1 \right] + x_o^2 \right\} \frac{1}{t} \frac{\mu \phi}{4 \Delta P} \tag{4.1}$$

$$K_y = \left\{ y_f^2 \left[2 \ln \left(y_f / y_o \right) - 1 \right] + y_o^2 \right\} \frac{1}{t} \frac{\mu \phi}{4 \Delta P} \tag{4.2}$$

where x_f and y_f are the coordinates of the flow front position, x_o and y_o are the coordinates of the inlet radius,ϕ the porosity,μ the fluid viscosity and ΔP the injection pressure.

4.2.2 In-plane and transverse deviation angle

The in-plane deviation angle α is the angle between the ellipse major axis and the reinforcement warp direction (x).

Due to the interlock's elevated thickness and complex geometry, it can't be assumed that there is no transverse deviation occurrence. Before further transverse permeability measurements, the direction of the transverse flow will be investigated. In order to measure the transverse deviation angle θ, the radial injection method was adapted so the orientation of the transverse flow was also measured. This is done by measuring the distance between the projection of the top injection point and the center of the ellipse formed at the bottom of the fabric as it will be described in detail in the next section.

4.2.3 Experimental set-up description

The fabric is compressed to the desired fiber volume fraction using a hydraulic press INSTRON 8805. The compression system consists of a steel chassis with an transparent

platen composed by three tempered glass of 19 mm. The bottom plate is 60 mm thick and it allow us to see the bottom of the fabric. A camera is positioned under the chassis to record images from the bottom up as seen in Figure 4.3.

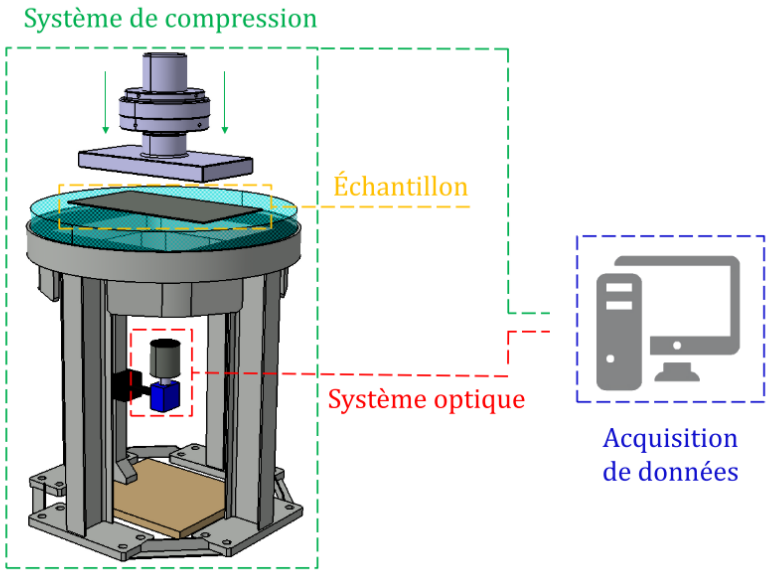

Figure 4.3: Experimental set up used for the radial injection of INCREASE interlock [27]

The top platen is metallic and it has a lateral perforation in which a pressure sensor and a valve are plugged into to limit and control the fluid flow as shown in Figure 4.4. The feeding tube is connected to a pressure bucket that will pressurize the fluid at a constant pressure.

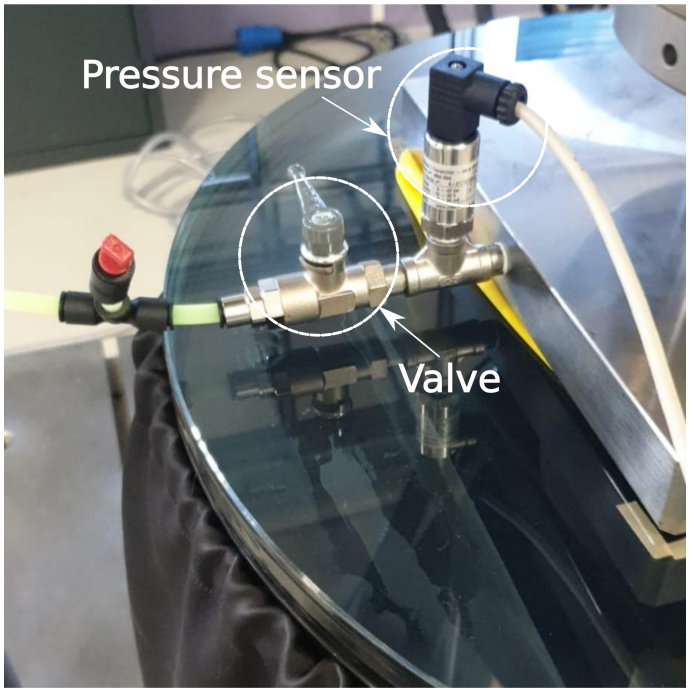

Figure 4.4: Valve and pressure sensor installed on top rectangular platen

4.2.4 Experimental procedure

The experimental procedure consists in placing the fabric over the 60 mm thick glass platen. The fabric is compressed to the desired thickness using a rectangular platen with a central injection from which a mixture of glycerol and UV pigment (as described in Section 3.2.2) will be injected. A camera positioned below the glass platen will record the evolution of the ellipse that is formed at the bottom of the fabric during the injection as shown in Figure 4.5. The semi-axes of the ellipses will be used to calculate the in-plane permeability using Equation 4.1 and 4.2 and the in plane deviation angle α.

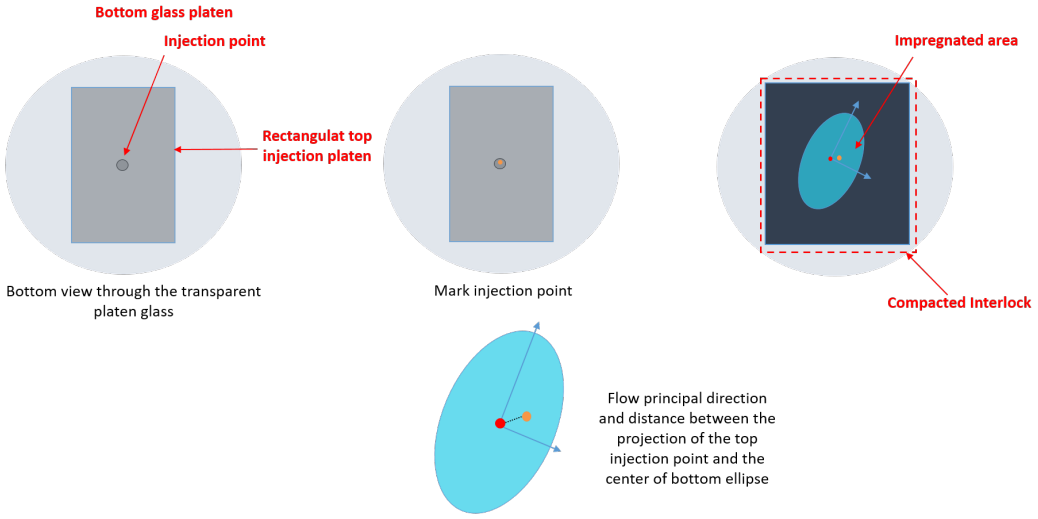

Figure 4.5: Experimental scheme for the in-plane permeabilities and deviation angle measurements.

The injection gate is located at the center of the rectangular mold. The effects of the transverse skew terms can be seen by comparing the distance from the center of the ellipse formed at the bottom (B) and the projection (C) of the injection point (A). The point (B) will shift towards the x direction with respect to the injection point (A) with the presence of a non-zero K_{xz} term and in the y direction when a non-zero K_{yz} skew appears [61]. The angle θ (shown in Figure 4.6) represents the transverse deviation angle of the flow through the thickness of the preform.

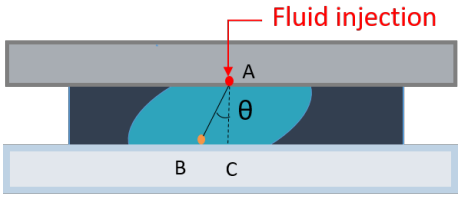

Figure 4.6: Scheme of transverse deviation angle θ

4.2.5 Flow visualization

Flow visualization on carbon fabrics like the INCREASE interlocks is very difficult since the carbon is not translucent and dark. To increase the contrast between the injected fluid and the fabric, UV lights and fluorescent pigment were used to allow a better visualization of the flow.

A number of different pigments were tested and the best contrast was achieved using

the commercial powdered pigment Fluo Yellow 502 by Sennelier (Figure 3.5). A pigment concentration comparison was done to determine the amount of pigment necessary to obtain a good contrast. A concentration of 1.5% of pigment was sufficient for good visualization of the flow as seen in Figure 4.7:

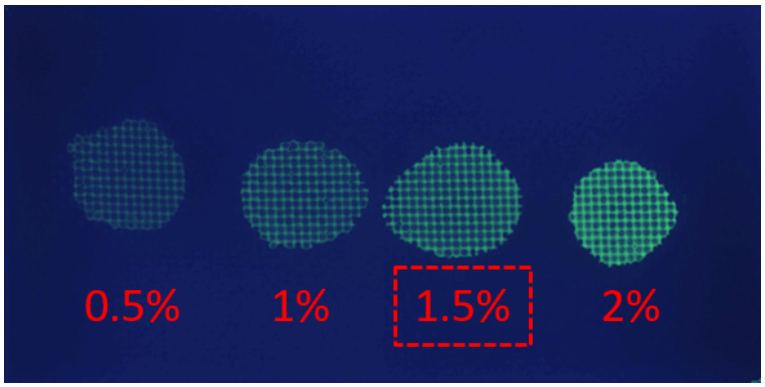

Figure 4.7: Pigment concentration test to increase flow contrast over carbon fibers

4.2.6 Image and pressure acquisition

The pressure at the injection point is measured using a pressure sensor. A computer with data acquisition software (LabVIEW) was used to record the injection pressure and save pictures of the bottom plate taken with the camera at chosen time intervals.

The images were processed using MATLAB Image Processing Toolbox to create a binary image of the fluorescent flow front. The measurements of the center and radii of the binary image were done using MATLAB's *regionprops* function. Figure 4.8 (a) shows the raw image captured with the camera and Figure 4.8 (b) the binary image and the ellipse and main axes fitted with the *regionprops* function.

The length (in pixels) of the major and minor axes of the ellipse are then measured and also the angle between the x-axis and the major axis of the ellipse (deviation angle α as shown in Figure 4.2).

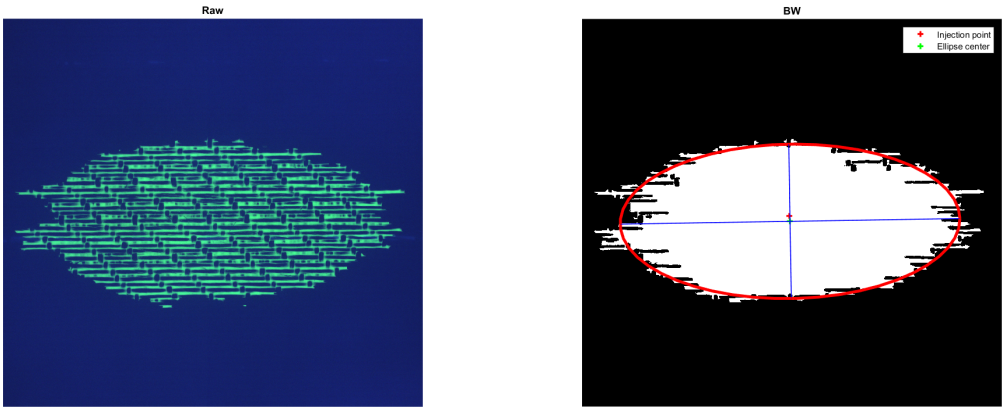

(a) (b)

Figure 4.8: INCREASE 06 radial injection flow pattern: Closing force 50 kN; $V_f = 55\%$; Injection pressure: 2 bar; $\mu_{glycerol} = 0.69$ Pa.s; Deviation angle $\alpha = 0.943$

The conversion from pixels to cm is made by measuring a reference photo taken in

the same configuration as the tests with a calibration chess board with know dimensions as seen in Figure 4.9.

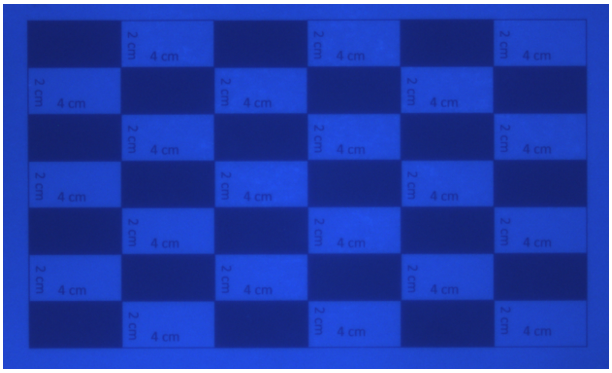

Figure 4.9: Conversion board used for conversion of pixels to cm

4.2.7 Experimental parameters

Three tests were preformed for both interlock configurations INCREASE 02 and INCREASE 06. The samples were compressed until a targeted V_f of 50%, 55% and 60%. Figures 4.10 and 4.11 show the raw images captured of each radial injection experiment of the INCREASE 02 and INCREASE 06 geometries respectively and Table 4.1 describes the used parameters of each test.

Geometry	Target V_f (%)	Real V_f (%)	Fluid viscosity (Pa.s)	Injection Pressure (bar)
INCREASE 02	50	49.1	0.53	1.7
	55	53.2	0.82	2.1
	60	59.8	0.65	2.1
INCREASE 06	50	48.4	0.53	1.7
	55	54.7	0.69	1.7
	60	59.0	0.53	1.7

Table 4.1: Radial injection test parameters

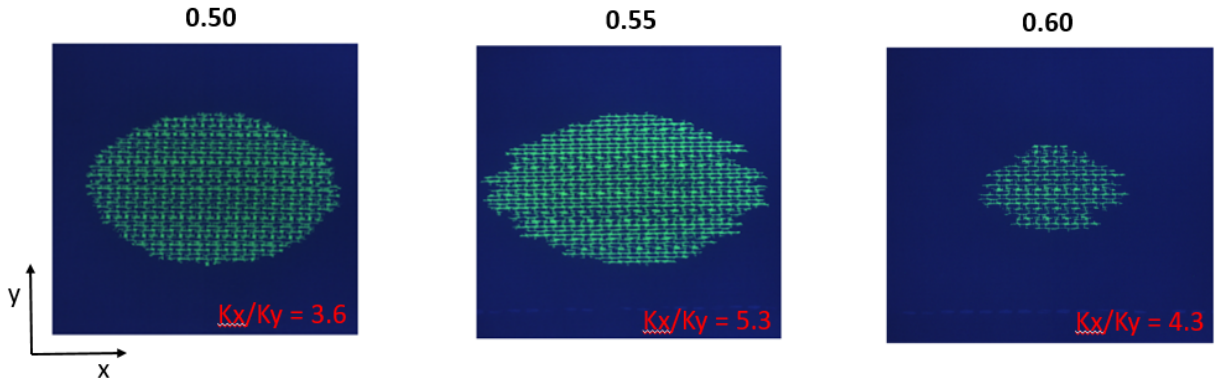

Figure 4.10: INCREASE 02 radial injection tests at different V_f (50% left, 55% center and 60% right)

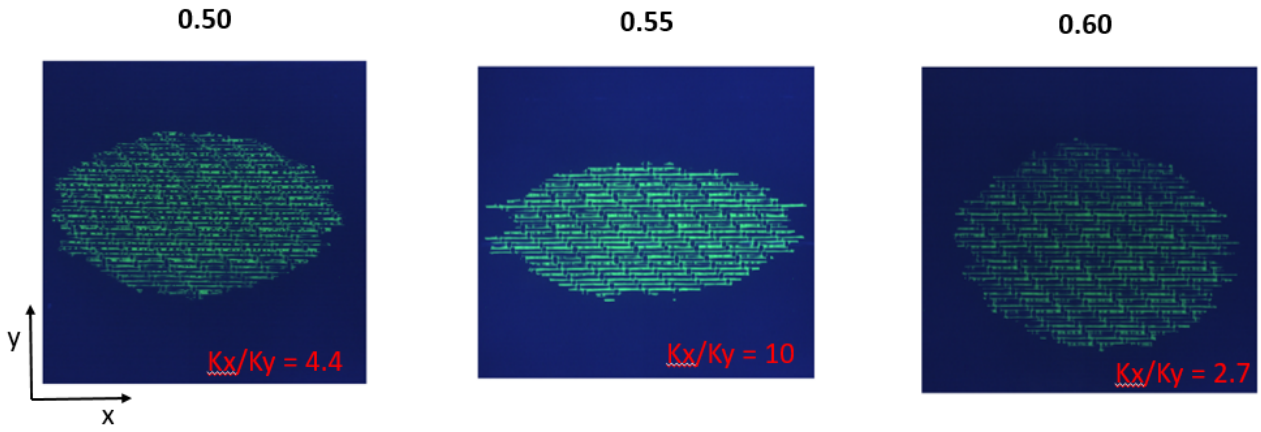

Figure 4.11: INCREASE 06 radial injection tests at different V_f (50% left, 55% center and 60% right)

4.2.8 Results of permeability tensor orientation

In Plane orientation

The in-plane orientation angle α observed was very small in all test (except α = -5° for the test of INCREASE06 at $V_f = 60\%$). The flow principal direction can be considered to coincide with the material's principal direction (weft, warp) and the permeabilities in the weft and warp direction K_x and K_y can be calculated directly using Equations 4.1 and 4.2.

Geometry	Target V_f (%)	Real V_f (%)	α(°)
INCREASE 02	50	49.1	0
	55	53.2	-0.5
	60	59.8	0
INCREASE 06	50	48.4	-1
	55	54.7	0.5
	60	59.0	-5

Table 4.2: In-plane orientation angle α measured during radial injection

Transverse orientation

The projected distance BC between the injection point and the center of the ellipse formed at the bottom of the fabric was measured and with the fabric thickness (AC) the transverse deviation θ was calculated.

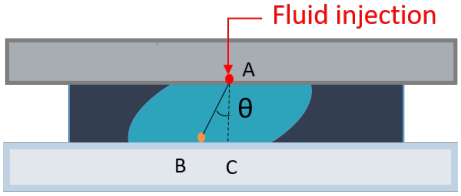

Figure 4.12: Scheme of the transverse deviation angle θ

The deviation angle θ measured during the INCREASE06 injections at different V_f can be seen in Table 4.3.

As shown in Figure 4.13 and Figure 4.14, in the first stages of the injection, the projected distance between the injection point and the center of the bottom ellipse is the most elevated. As the injection continues, the distance decreases and then it stabilizes until the end of the injection.

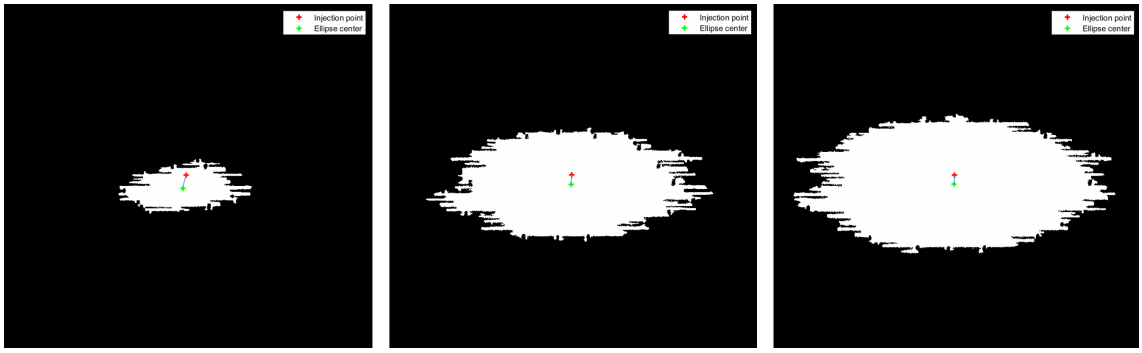

Figure 4.13: Projected distance over time between injection point (red cross) and bottom ellipse center (green cross) of INCREASE 06 at $V_f = 55\%$

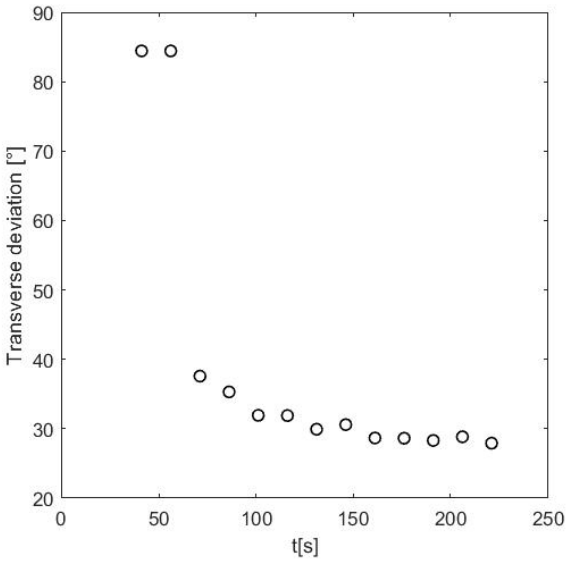

Figure 4.14: Transverse deviation θ of INCREASE 06 at $V_f = 55\%$

The measured transverse deviation θ is significantly higher than the in-plane deviation α. Table 4.3 shows that θ is 35° in average. A series of incomplete RTM tests were preformed to measure the both top and bottom ellipses and the transverse deviation was found to be much smaller and considered negligible (see Section 4.3 for more detail). This difference may be due to measurement inaccuracies when calculating the image center of mass using the *regionprops* function. The ellipse has an approximate fit since the flow front contour is not smooth due to the very dense tows and large inter tow-spacing.

It is also an hypothesis that the injection point is also the center of the top ellipse. Since only the bottom of the fabric is visible, it cannot be affirmed with certainty that the injection point and the top center coincides.

Material	Target V_f (%)	Real V_f (%)	θ(°)
INCREASE 06	50	48.4	32
	55	54.7	30
	60	59.0	43

Table 4.3: Transverse orientation angle θ

4.2.9 In plane permeability

The in-plane permeabilities K_x and K_y were calculated using Equations 4.1 and 4.2. Table 4.4 shows the permeabilities calculated for each experiment:

Geometry	Target V_f (%)	Real V_f (%)	K_x (m^2)	K_y (m^2)
INCREASE 02	50	49.1	1.46×10^{-10}	4.32×10^{-11}
	55	53.2	2.07×10^{-11}	3.42×10^{-12}
	60	59.8	1.29×10^{-11}	1.01×10^{-11}
INCREASE 06	50	48.4	1.20×10^{-10}	2.74×10^{-11}
	55	54.7	9.61×10^{-11}	9.03×10^{-12}
	60	59.0	2.38×10^{-11}	8.75×10^{-12}

Table 4.4: Radial injection test parameters

Figure 4.15 shows that the permeability of the INCREASE02 geometry lower than of the INCREASE06 at a higher V_f. Measured permeability decreases when the fabric is compressed and the anisotropy ratio K_x/K_y of the INCREASE06 decreases while the ratio of the INCREASE02 geometry stays constant for the fiber volume fraction range observed.

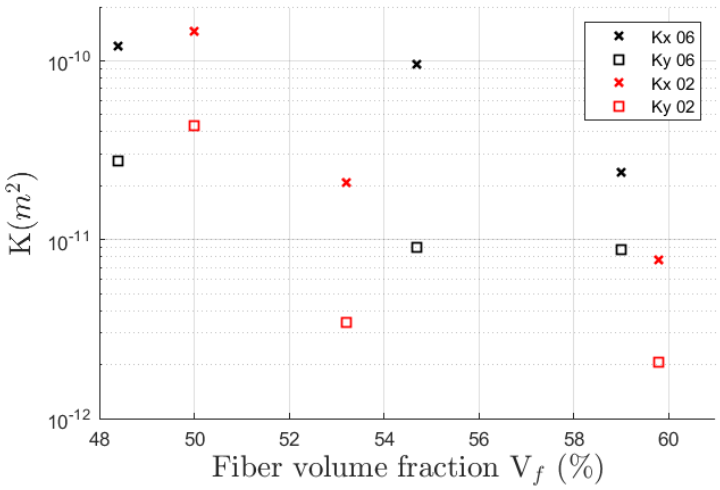

Figure 4.15: Permeability of INCREASE 02 and INCREASE 06 over a range of V_f between 50 and 60 %

4.2.10 Partial conclusion

The radial injection technique here described was successful in extracting the main in-plane permeabilities K_x K_y and both in-plane and transverse deviation angle. The in-plane deviation angle α was negligible so the calculated permeability directions coincide with the reinforcement's main directions of warp and weft. The transverse permeability deviation angle θ is shown to be larger (around 35°). A limitation of this method is that only the bottom ellipse is visible an therefore it cannot be affirmed with certainty that the injection point is the actual center of the top ellipse.
This technique requires special equipment such as a hydraulic press to apply up to 40 bar pressure, 60 mm thick transparent bottom platen and a UV optical acquisition set-up. An alternative method that can be used to calculated the permeability in a similar manner (measuring the flow front position) and easier to implement industrially will be here described.

4.3 Incomplete RTM filling

4.3.1 Introduction

To complement the measurements done at a laboratory scale using the radial injection technique, an incomplete RTM filling test was proposed and performed at IRT-M2P Pôle composites. The idea is to inject 1/3 of the total volume of resin necessary to fully impregnate a plate in order to visualize the ellipses formed at the top and bottom of the plate. The in-plane deviation angle can be measured using the ellipse axes (Figure 4.16) and also the transverse deviation angle by comparing the distance between centers of the top and bottom ellipses.

Since the fabric's geometry is very open, in order to freeze the flow and conserve the ellipses shape during injection, a fast cure resin (EP06170/EK06170 produced by HEXION) is used. Table 4.5 describes the experimental parameters used for the three incomplete RTM filling test:

$V_f(\%)$	Fabric weigth (g)	Initial thickness (mm)	Injection flow (g/s)	Total injected weight (g)	Final thickness (mm)
45	2902	21	50	3610	14.3
55	2929	21	50	3390	11.7
65	2938	21	50	3243	9.8

Table 4.5: Incomplete RTM filling tests parameters

4.3.2 Permeability calculation

By knowing pressure at the injection or at an arbitrary point, the in-plane permeability can be calculated without the need of visual inspection. Weitzenbock et al. presented an unified approach [78] to calculate the principal permeability using radial injection with different boundary conditions and data acquisition. Unfortunately, the pressure sensors used in the incomplete experiment were not adapted for the RTM process and therefore, the permeability could not be extracted via the tests due to lack of pressure data. This method is, however, recommended due to easier implementation and practicality in comparison to the radial injection technique done at a laboratory scale.

4.3.3 Anisotropic ratio

As we can see in Figures 4.17, 4.18 and 4.19 the incomplete RTM filling tests were successful in preserving the both top and bottom ellipses. Even though the pressure sensor at the injection was not functional at the time of the RTM incomplete tests, the permeability anisotropic ratio K_x/K_y can be calculated since the semi-major and minor axes of the ellipse represent the square roots of the principal permeabilities as seen in Equation 4.3 [77]:

$$\frac{x_f}{y_f} = \sqrt{\frac{K_x}{K_y}} \tag{4.3}$$

where x_f and y_f are the coordinates of the flow front (semi-major and minor axes). This anisotropy ratio will complement the ones measured with the radial injection technique described in section 4.2.

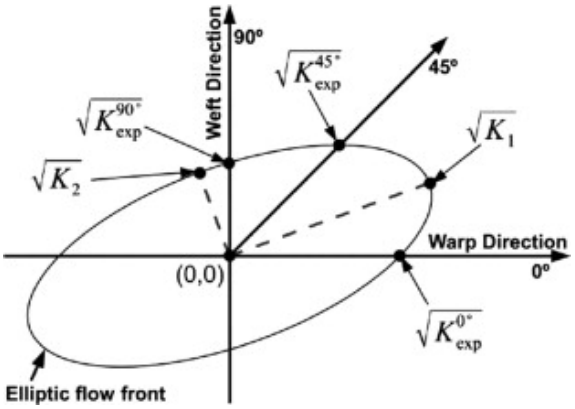

Figure 4.16: Elliptic pattern of a fluid flowing through a fibrous reinforcement [75]

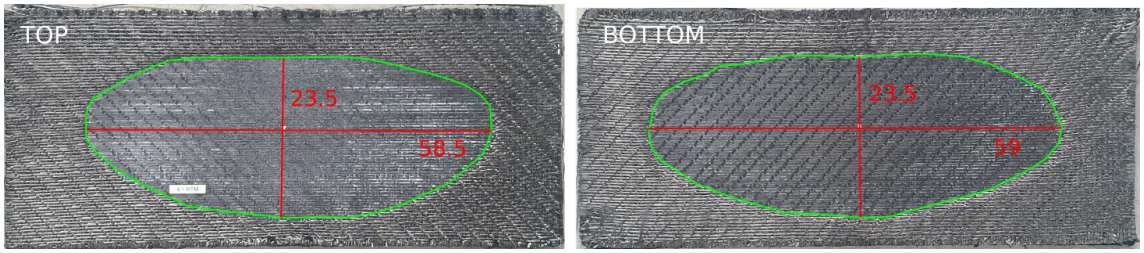

Figure 4.17: Incomplete RTM filling plate using the geometry INCREASE 06 at $V_f = 45$ %

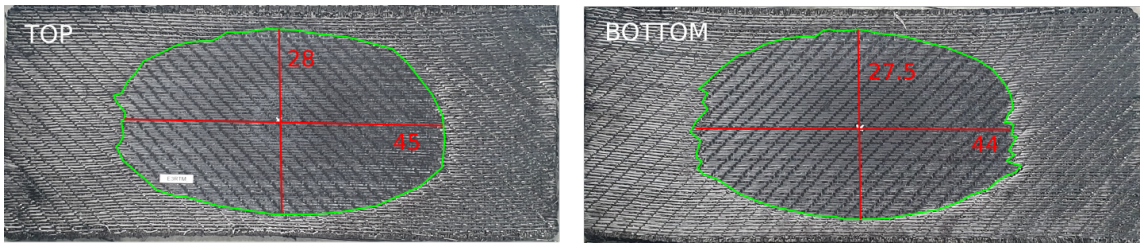

Figure 4.18: Incomplete RTM filling plate using the geometry INCREASE 06 at $V_f = 55$ %

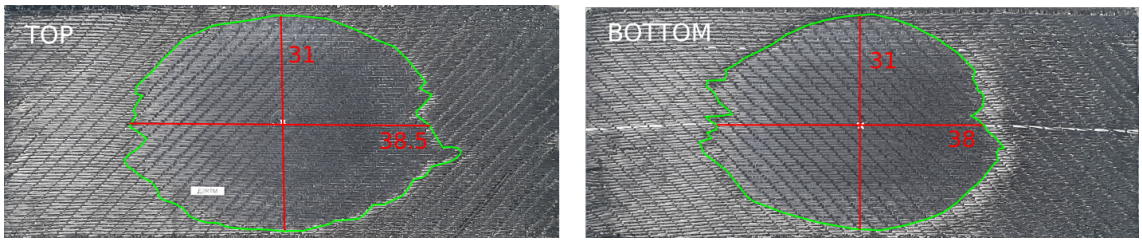

Figure 4.19: Incomplete RTM filling plate using the geometry INCREASE 06 at $V_f = 65$ %

Figures 4.17, 4.18 and 4.19 show the top and bottom ellipses formed. In all tests both top and bottom ellipses have close dimensions. Table 4.6 describes the measured axes and the anisotropic ratio calculated for each experiment.

V_f (%)	Top major axis x_f^t(cm)	Bottom major axis x_f^b (cm)	Top minor axis y_f^t(cm)	Bottom minor axis y_f^b (cm)	Top aniso. permeability ratio $\frac{x_f^{t_2}}{y_f^{t_2}}$	Bottom aniso. permeability ratio $\frac{x_f^{b_2}}{y_f^{b_2}}$
45	58.5	59	23.5	23.5	6.19	6.30
55	45	44	28	27.5	2.58	2.56
65	38.5	38	31	31	1.54	1.50

Table 4.6: Incomplete RTM filling tests parameters for INCREASE 06

When combining the anisotropic ratio measured with the radial injection technique and the incomplete RTM filling tests we can observe a decrease in anisotropy ratio with the augmentation of V_f. The values of both techniques were fitted in a polynomial curve that represents the anisotropy evolution during compression as seen in Figure 4.20. The ratio of the radial injection at $V_f = 55$ % (Figure 4.11) was abnormally high and was then excluded from the fit.

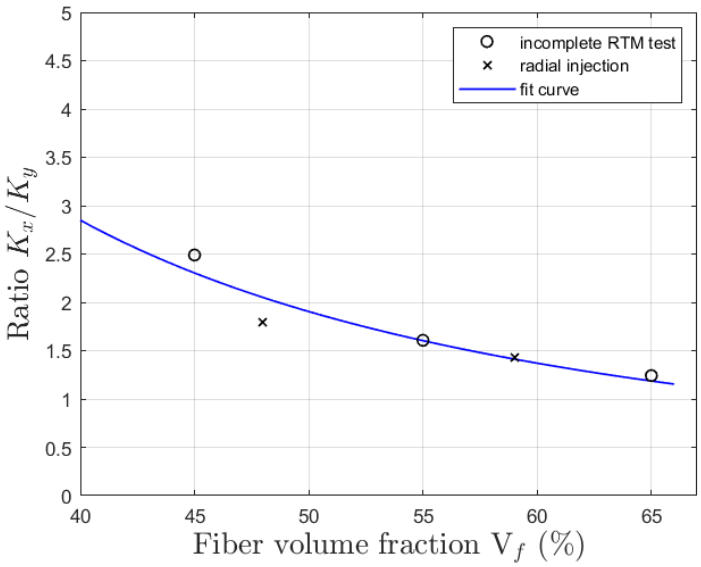

Figure 4.20: Permeability anisotropic ratio K_x/K_y for the INCREASE 06 for V_f ranging from 45% to 65%

4.3.4 Transverse deviation

No considerable transverse deviation was observed during the incomplete RTM fill tests. Figure 4.21 shows the bottom of the plate at $V_f = 55\%$. The green cross represents the injection point at the top and the red cross is the center of mass of the bottom ellipse (dotted red line). Both centers are very close, no considerable deviation was observed in all tests. The flow can be then, considered fully transverse.

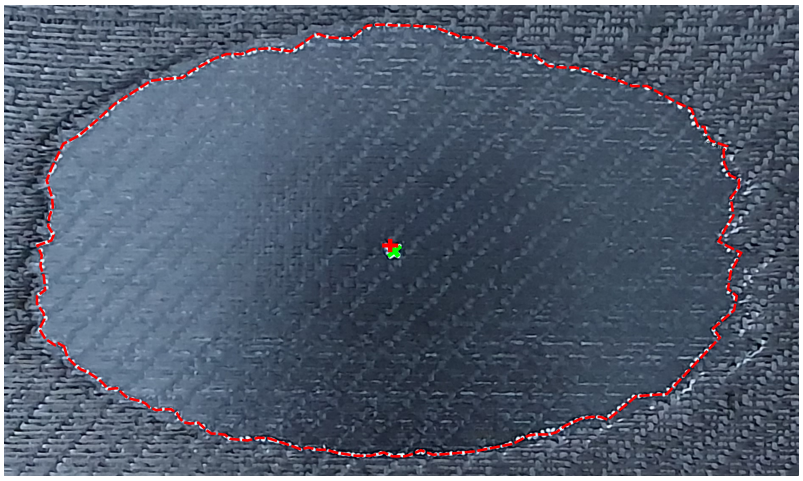

Figure 4.21: Bottom ellipse of incomplete RTM filling at $V_f = 55$ %, the red cross is the center of the bottom ellipse and the green cross is the position of the inlet gate

4.3.5 Partial conclusion

The radial injection with UV optical set-up provided measurements of the permeability in-plane tensor including in-plane anisotropy ratio and deviation angles (in-plane and out-of-plane). The incomplete RTM filling test have validated the measurements of in-plane anisotropy ratio and of both deviation angles.
From both test benches it was observed that the in plane deviation angle α is very small therefore the main permeabilities coincide with the weft and warp directions. The transverse deviation angle θ (Figure 4.12) was larger for the radial injection measurements but that was not observed when comparing the center of the top and bottom ellipse made with incomplete RTM filling as the centers of top and bottom ellipses coincide.
Performing an incomplete volume RTM filling is an easier to implement measurement technique that allows to calculate the in-plane permeability and deviation angle with appropriate pressure acquisition. It does not, however measure the transverse permeability. For that, a saturated compression technique is proposed in the following.

4.4 Saturated compression

4.4.1 Introduction

The saturated compression technique allows to continuously calculate the in-plane and transverse permeability during compression. Three independent test configurations are necessary for the full permeability characterization, being practical and saving material (limiting the quantity necessary). The principle of this method consists in compressing a saturated fabric and extracting the in-plane and transverse fluid pressure to then calculate

the permeability evolution during compression [15]. This is a steady-state method that measures the saturated permeability of a fabric. The continuous compression also mimics what happens during C-RTM and gives the permeability evolution at a large range of V_f.

By combining the saturated compression technique with the anisotropy ratio and deviation angle that were measured with the injection techniques previously described a full 3D permeability tensor can be obtained.

4.4.2 Consolidation of a saturated porous material

Total stress constitutive equation

When impregnated fiber reinforcements are compressed, the total stress applied over the sample σ_z results from the stress applied onto the fiber reinforcement σ_z^f and the hydrostatic fluid pressure P [70, 8] as given in Eq. 4.4.

$$\sigma_z = \sigma_z^f + bP \tag{4.4}$$

where b is the Biot coefficient [8]. Following Terzaghi's assumption ($b = 1$ meaning that the fiber bulk modulus is higher than that of the reinforcement), the experimental fluid force $F_{\text{fluid,exp}}$ can be extracted by subtracting the lubricated fiber reinforcement $F_{\text{lub.}}$ contribution from the total applied force F_{tot} :

$$F_{\text{fluid,exp}} = F_{\text{tot}} - F_{\text{lub.}} \tag{4.5}$$

The fiber reinforcement contribution is lubricated and not dry since all internal friction is lubricated with a low viscosity fluid. To obtain the total stress σ_z and the effective stress applied onto the fiber reinforcement σ_z^f (both in-plane and transverse cases) three different experimental configurations are necessary in order to measure the specific contributions:

Total stress measurement F_{tot}

The goal of this experiment is to measure the total stress that comes from the response of both fibers and fluid. The fiber reinforcement is properly impregnated (as recommended in Section 3.3) then placed into a receptacle filled with fluid. This step is particularly important for open structures such as the INCREASE interlock to avoid fluid loss since this method is sensitive to the degree of saturation. To generate an in-plane flow, a filled platen is placed below the sample as seen in Figure 4.22. In order to sense the fluid response when out-of-plane (transverse) flow occcurs, the compression setup is modified. A perforated bottom platen is positioned to let the fluid flow in both transverse and the in-plane directions (Figure 4.23). The fluid pressure measured in this configuration will be sensitive to the value of the transverse permeability K_z.

Effective stress measurement F_{lub}

In order to measure the fiber reinforcement lubricated compression response σ_z^f the reinforcement is lubricated with a low viscosity fluid ($\mu = 0.01$ Pa.s) and placed on a perforated platen (Figure 4.24) to zero the fluid pressure (drained configuration).

4.4.3 In-plane equivalent permeability of a fiber reinforcement

Darcy's law describes the fluid flow through a porous media [17]:

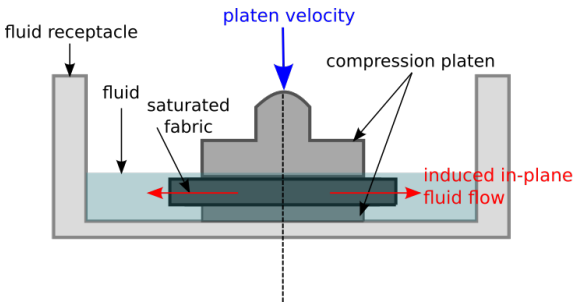

Figure 4.22: Experimental set-up for in-plane flow

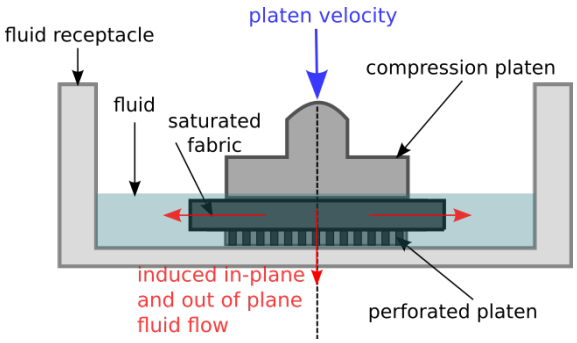

Figure 4.23: Experimental set-up for a combined in-plane and transverse flow

$$\boldsymbol{u_D} = -\frac{\mathbf{K}\left(V_f\right)}{\mu} \cdot \nabla P \tag{4.6}$$

Where $\boldsymbol{u_D}$ is the Darcy velocity, $\mathbf{K}$ is the permeability tensor, μ is the fluid viscosity, V_f is the fiber volume fraction and ∇P the fluid pressure gradient. By combining Darcy's law with the mass conservation equation and considering that the deformation occurs only transversely (the reinforcement is rigid in-plane) [25] we have the continuity equation:

$$\nabla \cdot \left[h \frac{\mathbf{K}\left(V_f\right)}{\mu} \nabla P\right] = \dot{h} \tag{4.7}$$

Where h is the sample thickness and $\dot{h}$ is the closing speed. Using a circular compression platen to calculate the in-plane quasi-isotropic permeability K_e, the Equation 4.7 can be integrated in cylindrical coordinates with the boundary conditions $P(r) = 0|_{r=R}$ and $\frac{\partial P}{\partial r} = 0|_{r=0}$ and leads to the fluid pressure profile seen in Equation 4.8:

$$P(r) = -\frac{\mu \dot{h}}{4 h K_e\left(V_f\right)} \left(R^2 - r^2\right) \tag{4.8}$$

Integrating Equation 4.8 over the platen area will provide the fluid force from Equation 4.9:

$$F_{\text{fluid},th} = \int_0^R 2\pi r P(r) dr = -\frac{\mu \dot{h} \pi R^4}{8 K_e\left(V_f\right) h} \tag{4.9}$$

The equivalent isotropic in-plane permeability K_e can be calculate with both experimental measurements of F_{tot} and F_{lub}:

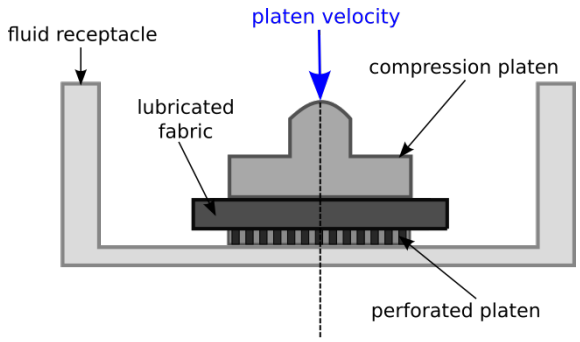

Figure 4.24: Experimental set-up for drained compression

$$K_{\mathrm{e}}(h) = -\frac{\mu \dot{h} \pi R^4}{8h\left(F_{tot} - F_{lub}\right)} \tag{4.10}$$

4.4.4 Transverse permeability

The combined in-plane and transverse flow configuration can be represented with the proper boundary conditions given in Figure 4.25 and the transverse permeability K_z can be calulated via the Equation 4.11 presented by Gutowski [25].

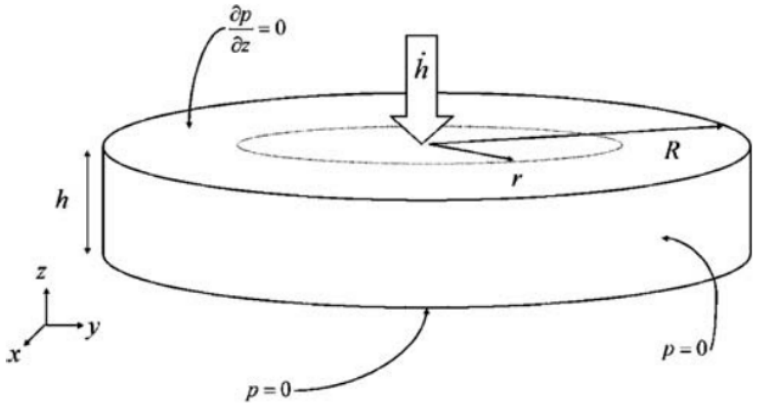

Figure 4.25: Boundary conditions to solve for the through thickness permeability measurements [15]

.

$$\frac{K_e}{r}\frac{\partial}{\partial r}\left(r\frac{\partial P}{\partial r}\right) + K_z\left(\frac{V_f}{V_f^0}\right)^2\frac{\partial^2 P}{\partial z^2} = -\mu\frac{\dot{V}_f}{V_f} \tag{4.11}$$

4.4.5 Compression test results

A series of compression tests were performed using the INCREASE06 interlock fabric. In order to generate enough fluid pressure to measure the permeability (Equation 4.5), the total stress σ_z measured must be higher than the effective stress of the fibers σ_z^f.

The fluid pressure increases via augmenting the fluid viscosity μ or the compression speed $\dot{h}$. For convenience and to not increase the time duration of the tests, a constant closing speed of $\dot{h} = 6$ mm/min was fixed and the tests were done varying the fluid viscosity.

The chosen model fluid was silicone oil produced by Carl Roth and the viscosity range varied from $\mu = 0.5$ Pa.s to $\mu = 10$ Pa.s. Figure 4.26 shows that the total stress response σ_z increases with the augmentation of the fluid viscosity. All of the tests produced a fluid pressure higher than the lubricated test and can be used to calculate the equivalent permeability K_e using Equation 4.10.

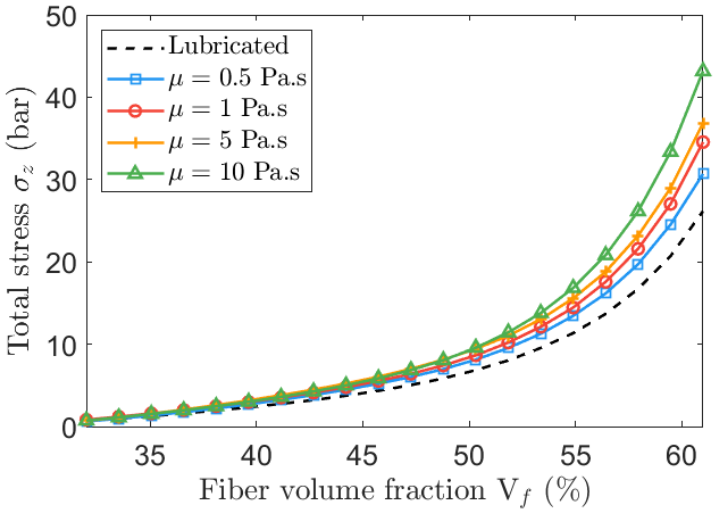

Figure 4.26: Saturated compression stress σ_z at iso-speed $\dot{h} = 6$ mm/min and varying fluid viscosity μ ranging from 0.5 to 10 Pa.s

4.4.6 Influence of saturation level

The proper sample impregnation protocol was described in Section 3.3. Figure 4.27 show three tests using the transverse set-up configuration described in Figure 4.23. All tests were done with closing speed $\dot{h} = 6$ mm/min and fluid viscosity $\mu = 10$ Pa.s.

Two samples were immersed in the fluid overnight and one sample was immersed and degassed using a vacuum chamber overnight. The degassing allowed a better impregnation which is particularly difficult using higher viscosity fluids.

Even though the samples were impregnated slowly then left overnight under fluid they still produced significance less stress when compared to the sample that was degassed overnight. The immersed samples did not generated enough fluid pressure until around $V_f = 50\%$ and therefore the permeability below this V_f wont be measured. The degassed sample was much better saturated and produced an elevated response during the whole compression showing the importance of proper sample conditioning for this measurement method.

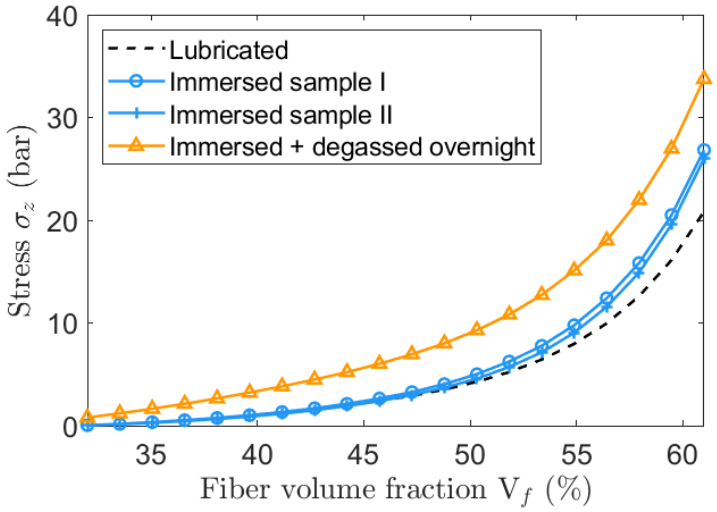

Figure 4.27: Influence of saturation level on the total stress σ_z response

4.4.7 Permeability results

Figure 4.28 shows the stress responses of the lubricated ($\mu = 0.01$ Pa.s), total in-plane equivalent ($\mu = 0.5$ Pa.s) and transverse tests ($\mu = 10$ Pa.s) used to calculate the equivalent in-plane and transverse permeability K_e and K_z.

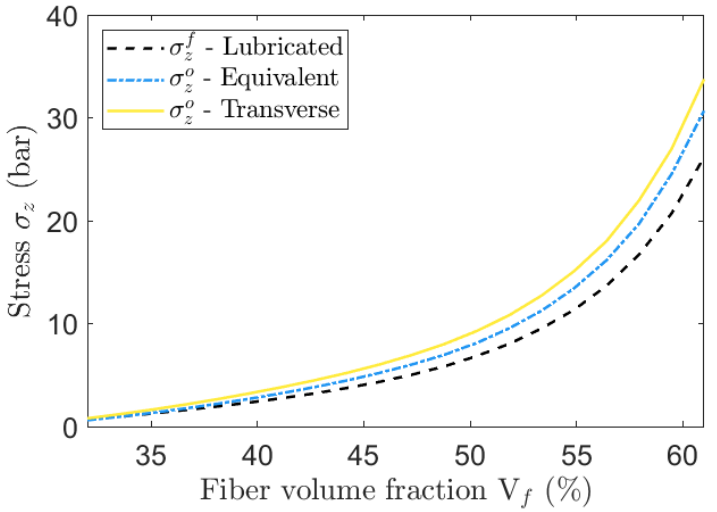

Figure 4.28: Response to compression of the INCREASE06 interlock saturated fabric, all tests were performed with $\dot{h} = 6$ mm/min

As seen in Figure 4.29 the transverse permeability is higher than the in-plane permeability in the beginning of the compression. This is a specificity of these interlock fabrics. They have a very open structure and because of the fiber tow weaved through the thickness, the transverse permeability is much higher than of a 2D woven fabrics. As the compression continues, the transverse permeability decreases at a higher rate than the in-plane permeability.

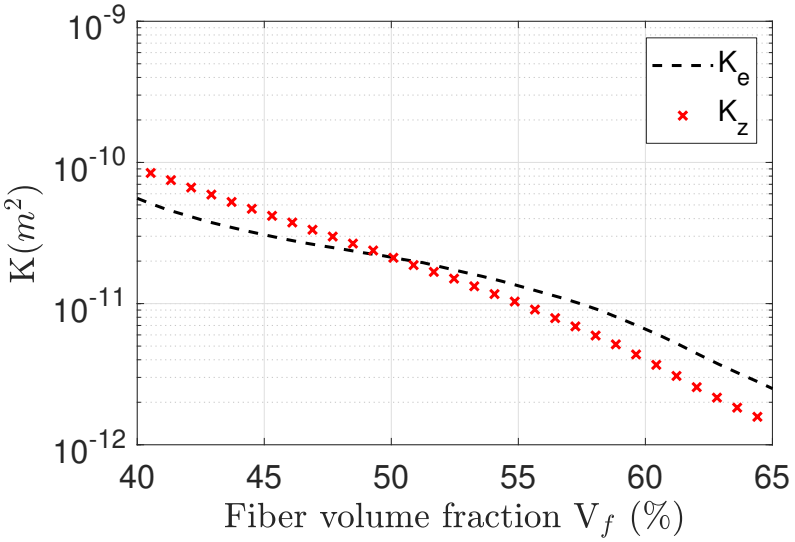

Figure 4.29: In-plane K_e and transverse K_z permeability of INCREASE 06, all tests were performed with $\dot{h} = 6$ mm/min

4.5 Anisotropy ratio and in-plane permeability

The saturated compression technique previously described provided the evolution of the in-plane equivalent permeability K_e. In anisotropic materials such as the interlock the anisotropic ratio is important to identify the permeabilities in the fabric's main direction (weft and warp).

The anisotropic ratio measured with the radial injection technique and the incomplete RTM filling test will be used to estimate the permeabilities in the warp K_x and weft K_y directions continuously. The fit curve shown in Figure 4.20 is used as the anisotropic ratio R. K_x and K_y are calculated as follows:

$$K_x = K_e\sqrt{R} \tag{4.12}$$

$$K_y = \frac{K_e}{\sqrt{R}} \tag{4.13}$$

With $K_e = \sqrt{K_x K_y}$ and $R = \frac{K_x}{K_y}$.

Figure 4.30 shows the permeabilities K_x (warp direction) K_y (weft direction) and the equivalent permeability $K_e = \sqrt{K_x K_y}$. The permeability ratio decreases during compression as K_x approaches K_y at a higher V_f.

The K_x and K_y were used to simulate the incomplete RTM filling tests using the resin injection software PAM-RTM. The comparison between the experimental resin flow front and the simulated with PAM-RTM can be seen in Figure 4.31. The permeability ratio used is very close to what was observed experimentally. The difference if the flow front advancement between both experimental and simulated can be explained by the dual scale nature of the fabric and the degree of saturation during the experiment.

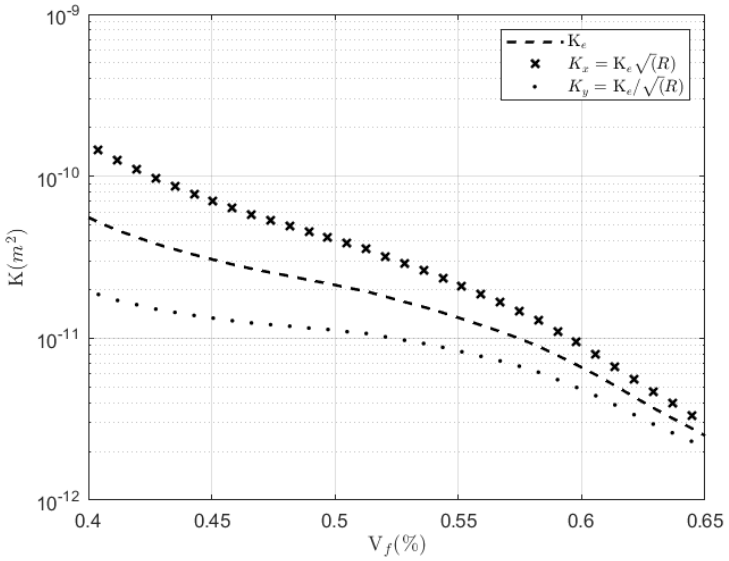

Figure 4.30: In-plane saturated permeability values K_x and K_y of the INCREASE06 geometry considering the anisotropic ration R from Figure 4.20 and the equivalent isotropic permeability K_e from Figure 4.29.

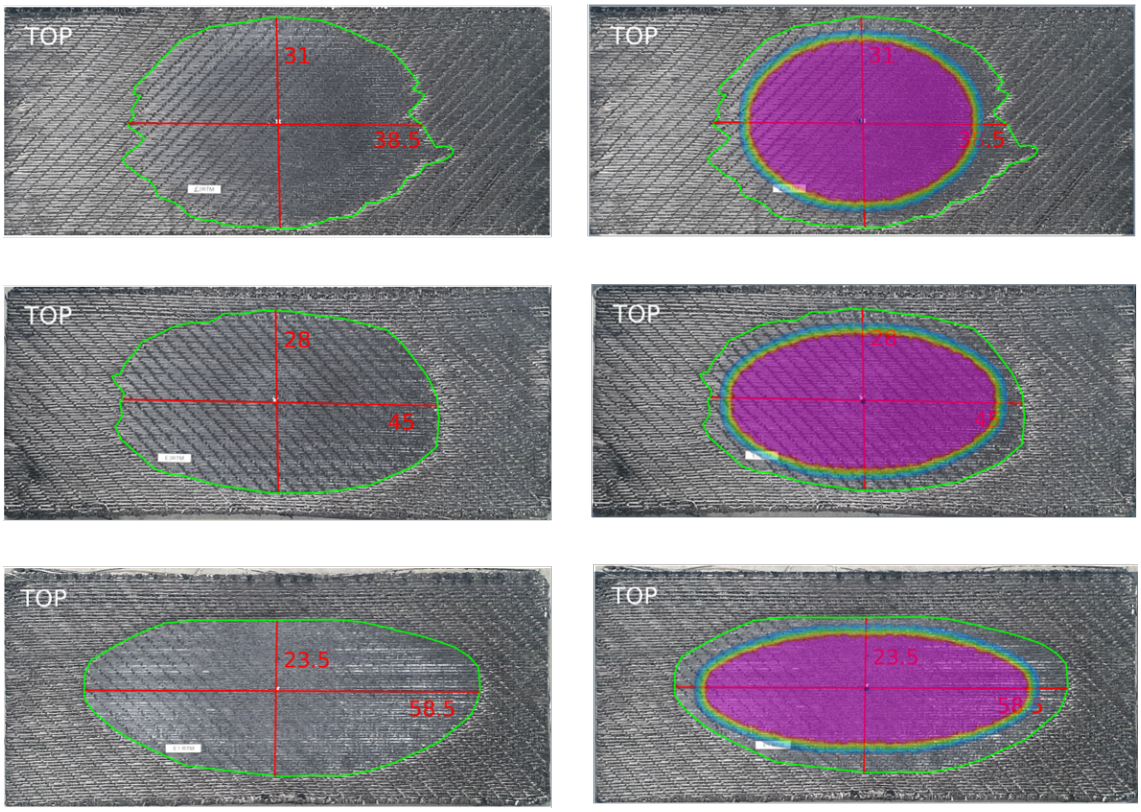

Figure 4.31: Comparison between experimental flow front and flow front calculated using PAM-RTM

4.6 Dual scale

A specificity of the interlock geometries presented in this study is that they have a quite open geometry (large inter-tow spacing) and are made with dense and twisted tows that are difficult to impregnate. The meso-pores (the spaces between the tows) are then filled much faster than the tow itself (Figure 4.32).

The dual porosity characteristic of fabrics can be higher or lower depending on the ratio between the bulk permeability and the tow permeability. A very prominent dual scale behavior was noticed in both INCREASE02 and INCREASE06 geometries. This phenomenon is quite clear when analyzing the flow front contour observed during the radial injection (Figure 4.33). The channels between tows are filled fast which creates a non-smooth contour of the flow front.

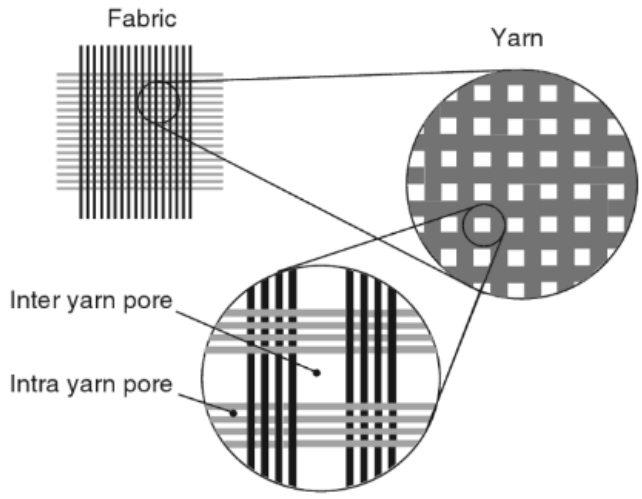

Figure 4.32: Inter and intra-yarn pores in fabrics [48].

A high dual scale behavior can implicate that the flow front observed is not fully saturated which can explain the difference in size between the experimental ellipses and the simulated ones since the simulation does not take into account the contrast between the bulk and tow permeability.

The saturation evolution of the INCREASE06 during injection will be investigated in Chaper 6.

4.7 Comparison between permeability measurement techniques

By comparing the continuous equivalent permeability (K_e) obtained through the saturated compression technique with the permeability measured via radial injection at three different fiber volume fractions, it is evident that the radial injection permeability is constantly higher than the saturated compression permeability (Figure 4.34).

Three key differences between techniques may contribute for this variation:

- During the radial injection, the fabric is compressed to a desired fiber volume fraction and then injected. This allows more time for the fabric to relax than during the

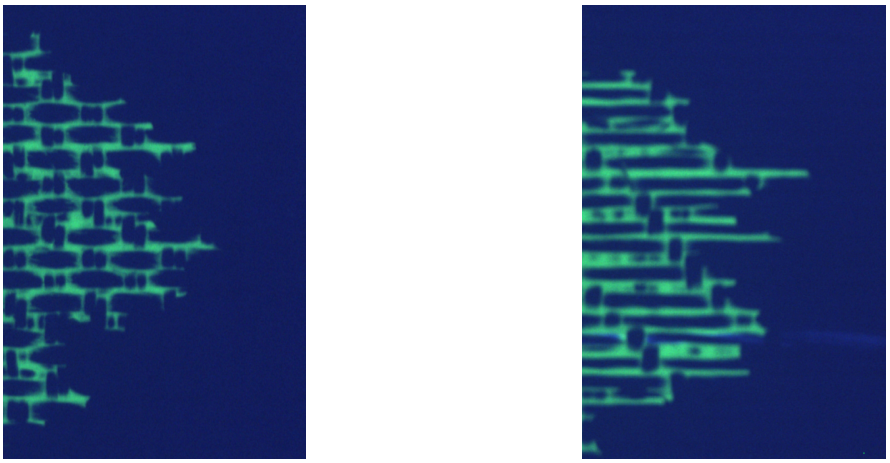

Figure 4.33: Flow front detail during radial injection of INCREASE02 (left) and INCREASE06 (right)

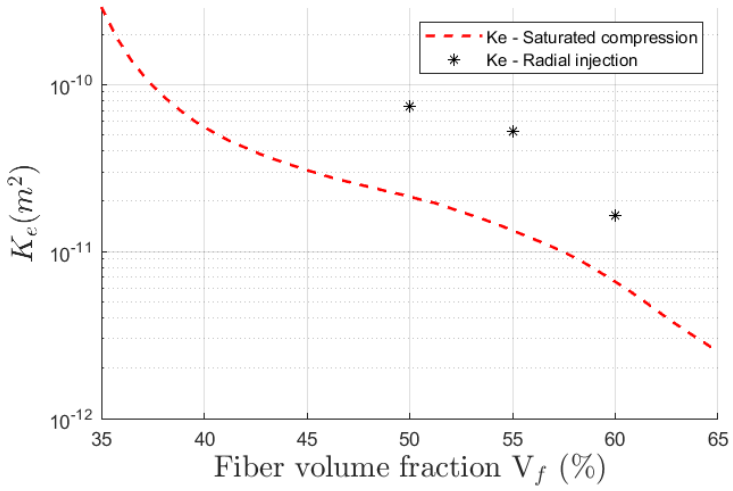

Figure 4.34: Equivalent in-plane permeability Ke of INCREASE06 calculated using saturaded compression and radial injection techniques.

saturated continuous compression. The decrease in force due to the fabric relaxation can be seen in Figure 4.35. The permeability may increase due to the rearrangement of the fibers during relaxation.

- The fabric is compressed in its dry state during radial injection and in its fully saturated during the saturated compression. The silicone oil lubricates and decreases the friction between fibers therefore the relaxation behavior of a lubricated and dry fabric will differ [31]. Since during the C-RTM we have both dry and saturated fabric (Figure 4.36) both permeability values are interesting to represent the different states.
- Due to the elevated dual-scale behavior observed in the INCREASE 06 fabric, the flow front position used to calculate the permeability is not fully saturated. The saturated flow front is somewhere behind the unsaturated front but it cannot be easily identified visually. Since the unsaturated front position is used to calculate the permeability using Equations 4.1 and 4.2 the apparent permeability appears

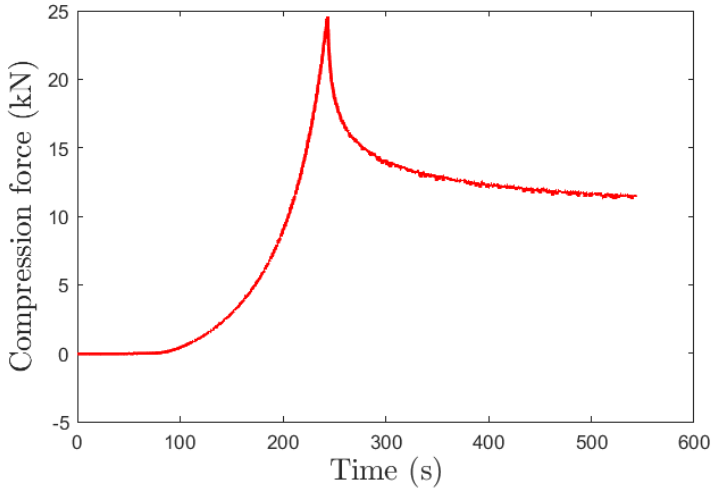

Figure 4.35: Compression force evolution during fabric compression (from $t = 0$ to $t = 550$ s) and relaxation observed in radial injection technique (INCREASE 06 $F_{max} = 25$ kN, $V_f = 50$ %)

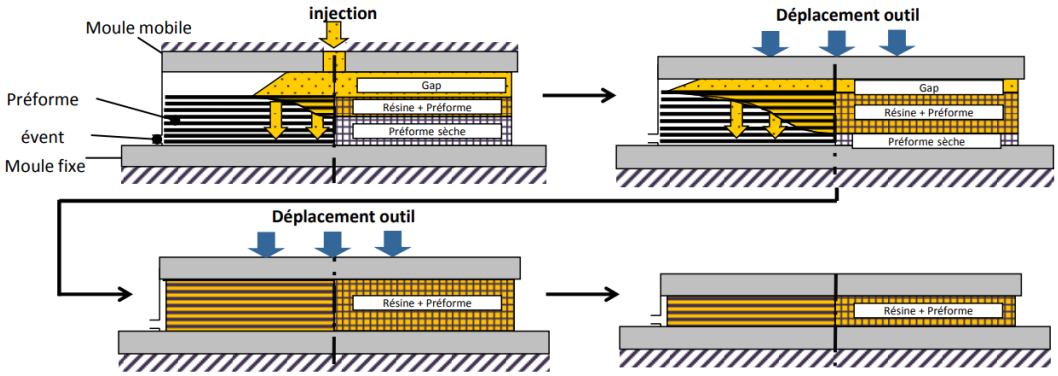

Figure 4.36: Description of C-RTM process [18]

higher since the axes of the unsaturated ellipse are larger than the ellipse axes if the fabric was fully saturated.

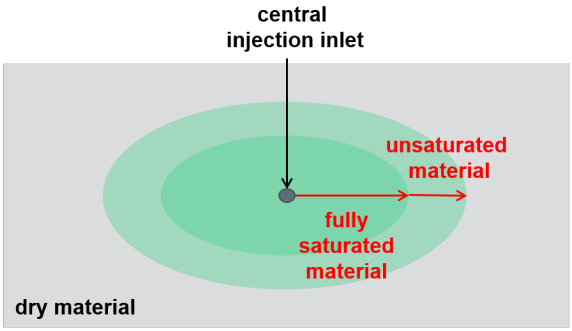

Figure 4.37: Schematic of the flow front observed during radial injectio. If the fabric has an elevated dual scale, the flow front observed is not fully saturated.

4.8 Conclusion

Two complementary techniques were adapted to measure the in-plane and transverse permeabilities of a interlock fabric with elevated thickness and stiffness:

- The Radial injection technique can be used to calculate the permeability in both warp K_x and weft K_y direction and also the in-plane and transverse deviation angle with a single experiment.
- The compression saturated technique can continuously measure the in-plane equivalent permeability K_e and the transverse permeability K_z during compression.

An alternative to the radial injection technique that does not require a transparent platen and optical measurement equipment is to perform incomplete volume RTM filling tests at different fiber volume fractions. By measuring the injection pressure at the injection gate the permeability in both main directions and in-plane deviation angle can be calculated and also the transverse deviation angle canbe measured by comparing the center of the top and bottom ellipse.

To continuously calculate the transverse permeability and the equivalent in-plane permeability the saturated compression technique is proposed. The permeability anisotropic ratio measured with both radial injection and incomplete RTM filling was used to approximate the values of K_x and K_y in a continuous way, similar to what is observed during the C-RTM process.

The differences in results between techniques come from the different state of the fabric itself since for the radial injection the fabric is compressed dry and kept on hold, which allow a larger relaxation time than the saturated continuous compression. The dual scale nature of the fabric also contributes to this difference since the ellipse axes used to calculate the permeability represents the unsaturated flow front and not the saturated one, which would have given a lower permeability result.

For a complete characterization of the interlock permeability both techniques should be used. The industrial protocol proposed is:

- Two or more (preferred three) incomplete RTM filling tests one at a low and one at a high fiber volume fraction with appropriate injection pressure sensor to calculate the two main permeabilities.
- Three saturated compression tests to measure the in-plane and transverse permeabilities with appropriate sample conditioning to ensure good saturation (vacuum degassing).
- The anisotropic ratio measured during injection can be used to calculate the two main in-plane permeabilities continuously using Equations 4.12 and 4.13.

This proposal is enough for a full characterization of the permeability tensor. The minimum amount of material necessary for the full characterization is less than 1 m^2 (0.89 m^2) making this approach complete and economical given the production cost of interlocks.

Chapter 5

Experimental identification of induced deformation

This chapter will describe a technique used to identify the occurrence of flow induced deformation during the compression of a saturated interlock fabric with no need of visual inspection. The compression signature behavior will be analyzed and compared to different well known fabrics and a processing window will be created for the interlock during the C-RTM process in order to avoid tow movement during compression.

Contents

5.1 Introduction

Chapter 3 of this study presented the experimental techniques used to characterize the permeability tensor of a thick interlock fabric. One of the assumptions made in applying Darcy's law to calculate the in-plane and transverse permeability is that the fibrous architecture remains rigid in-plane and only deforms transversely during compression. However, in reality, this assumption is not always valid.

During compression of a saturated fibrous reinforcement the flow can, under certain conditions, create a phenomenon known as fiber-tows washout (in-plane displacement of fiber-tows) due to the hydrodynamically induced drag force onto the fibrous reinforcement [28]. If there is an in-plane displacement of tows, the structure undergoes deformation and therefore the rigidity hypothesis is no longer valid and the calculated apparent permeability is no longer representative of the nominal fabric properties.

It is crucial to prevent flow-induced deformation such as fiber-tows washout, as it alters the intended configuration of the reinforcement and consequently impacts the desired mechanical properties. Moreover, it can lead to defects in the final part, as certain regions will become more densely packed with fibers than others.

To optimize the manufacturing process and reduce processing time, higher compression velocities and flow rates are often utilized increasing the fluid-solid interactions and therefore these parameters need to be appropriately chosen to avoid fiber-tows washout.

Visualizing the displacement of tows is challenging in carbon fabric reinforcements such as the interlock geometries of this study. In this chapter a technique to mechanically identify the occurrence of flow induced deformation without the need of visual inspection will be described.

To unsure the geometric integrity of the INCREASE interlock fabric during the C-RTM process, a processing window is created. This window serves to restrict the process parameters (closing mold speed $\dot{h}$) within specific limits to ensure that the viscous forces exerted on the interlock fabric won't cause deformation.

5.2 Identification of type of flow

The fluid-solid coupling during the compression of a saturated fibrous reinforcement can create two scenarios depending if the viscous-drag force induced by the flow are higher or lower than the friction between the tows. If the viscosity of the resin and the mold closing speed are sufficiently low, the drag force generated will not be sufficient to convect the fiber-tows and a filtration flow occurs as seen Figure 5.1 (a) [28].

If, however the fluid viscosity or the mold closing speed are too elevated, the viscous-drag forces will surpass the friction between tows and the fiber-tows will be convected. In this case, the induced fiber-tow in-plane washout deforms the fiber reinforcement mesostructure (Figure 5.1 (b)).

The identification of the type flow regime (filtration or convection) is very important for an optimal calibration of the process parameters while maintaining the fabric's desired structure.

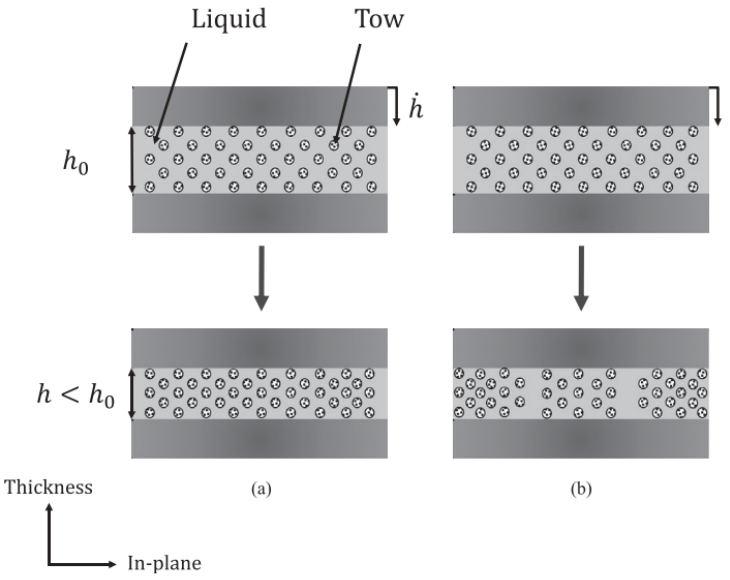

Figure 5.1: Representative scheme of the filtration (a) and convection (b) phenomenon [28].

5.3 Theory of composite consolidation

The approach to identify the occurrence of in-plane fiber-tow washout is to compare the experimental fluid force $F_{\text{fluid,exp}}$ seen in Equation 5.1 and measured with the saturated compression technique described in Section 4.4 with the theoretical fluid force $F_{\text{fluid},th}$.

The theoretical fluid force is calculated by integrating Darcy's law in conjunction with the conservation of mass (Equation 5.2), assuming the fabric to be static in-plane and only deforming transversely from compression.

$$F_{\text{fluid,exp}} = F_{\text{tot}} - F_{\text{lub}} \tag{5.1}$$

$$F_{\text{fluid},th} = \int_0^R 2\pi r P(r) dr = -\frac{\mu \dot{h} \pi R^4}{8 K_e (V_f) h} \tag{5.2}$$

Where h is the fabric thickness, R the compression platen radius, K_e the in-plane equivalent permeability and μ and $\dot{h}$ the fluid viscosity and mold closing speed respectively. The occurrence of in-plane movement can be identified when the experimental fluid force deviates from the quasi-static model.

5.4 Influence of fluid viscosity

The compression force of the saturated fabric F_{tot} must be higher than the compression force of the lubricated fabric F_{lub} in order to generate enough fluid pressure $F_{\text{fluid,exp}}$ to extract the in-plane equivalent permeability K_e (Equation 5.2). The total stress σ_z is the total force F_{tot} divided by the compression platen area S. The total stress can be increased by either increasing the fluid viscosity μ or the mold closing speed $\dot{h}$.

Figure 5.2 shows five saturation compression experimental tests: the lubricated sample is impregnated with a low viscosity silicone oil ($\mu = 0.01$ Pa.s) and positioned on top

of a perforated platen as seen in Figure 4.24 to measure the effective stress of the fibers ($\sigma_z^f = \frac{F_{\text{lub}}}{S}$).

The other four tests were performed varying the silicone oil viscosity: 0.5, 1, 5 and 10 Pa.s. A circular compression platen of diameter D = 150 mm was used to compress the samples at the same closing speed $\dot{h}$ = 6 mm/min. The samples were appropriately impregnated with fluid and then degassed overnight as described in the Section 3.3.

All of the tests generated a high enough fluid pressure necessary to calculate the in-plane equivalent permeability. The tests will now be analyzed in order to identify what is the limiting fluid viscosity to avoid in-plane deformation.

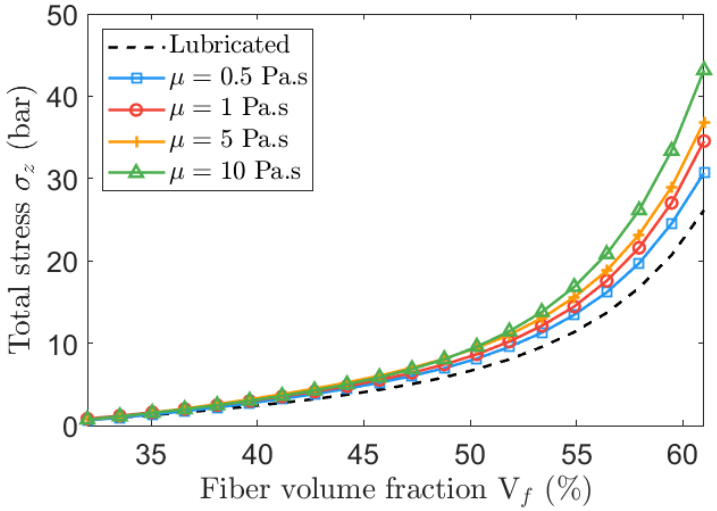

Figure 5.2: Saturated compression stress σ_z of INCREASE06 at iso-speed $\dot{h}$ = 6 mm/min and varying fluid viscosity μ.

5.5 Deformation identification

The visualization of the local deformation is very difficult for tows made out of carbon such as the interlock used in this study. Since carbon fibers are non-translucent and dark it is hard to quantify the tow displacement as it was previously done optically by Hautefeuille [27] with a glass twill G-Weave 600T PA (Figure 2.15).

The experimental fluid force $F_{\text{fluid,exp}}$ from the experiments shown in Figure 5.2 were compared to the theoretical fluid force $F_{\text{fluid},th}$ using Equation 5.2. The comparison results can be seen in Figure 5.3:

For lower fluid viscosity (μ = 0.5 Pa.s and μ = 1 Pa.s), the experimental fluid force is closely aligns to the theoretical one (Figure 5.3 (a)). The deviation increases above μ = 1 Pa.s (μ = 5 Pa.s and μ = 10 Pa.s) as seen in Figure 5.3 (b).

The force deviation ΔF is the difference between the theoretical fluid force $F_{\text{fluid},th}$ calculated using the Darcy model in Equation 5.2 and the experimental fluid force $F_{\text{fluid,exp}}$ from Equation 5.1 measured using the saturated compression method. The results can be seen in Figure 5.4:

The curves show that the deviation between the experiments and the theoretical fluid force increases drastically with a fluid of viscosity μ = 5 Pa.s and higher. The difference

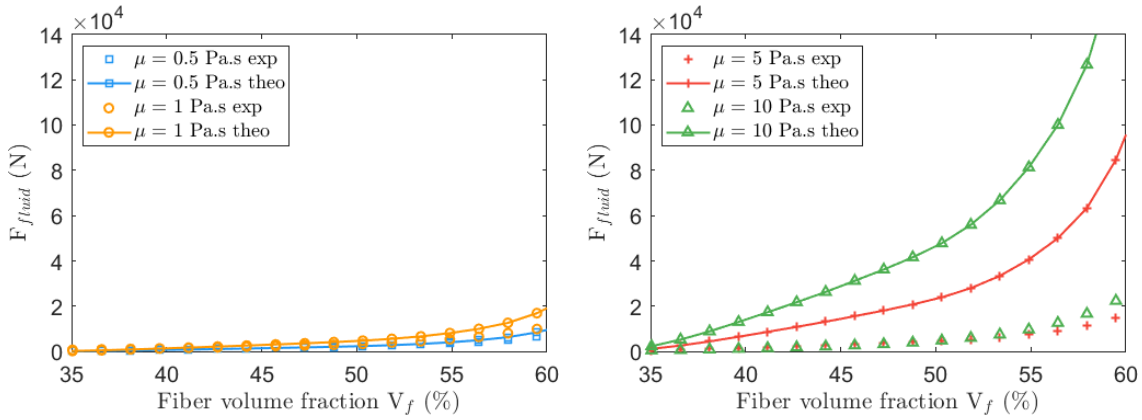

Figure 5.3: Theoretical and experimental fluid force measure at iso-speed $\dot{h} = 6$ mm/min and varying viscosity

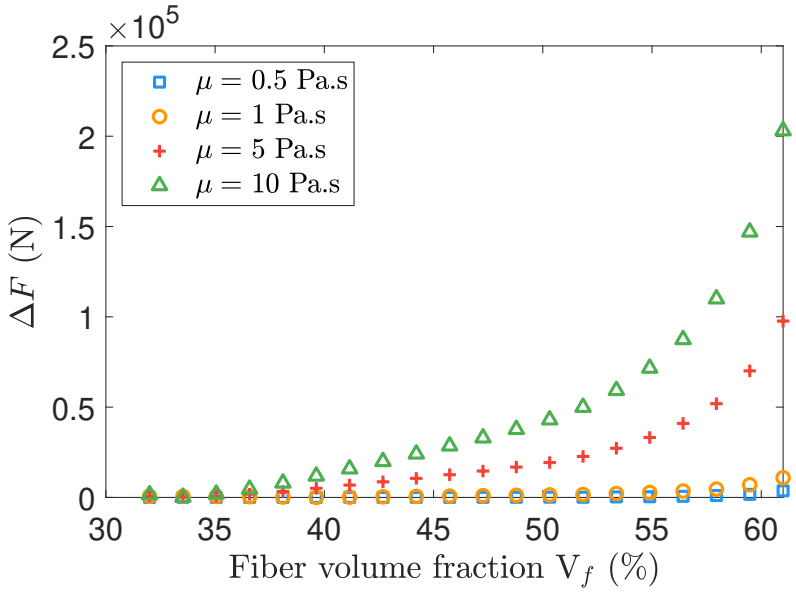

Figure 5.4: Deviation ΔF between theoretical $F_{\text{fluid},th}$ and experimental $F_{\text{fluide,exp}}$ fluid force at $\dot{h} = 6$ mm/min for the INCREASE06 interlock fabric

ΔF also increases during compression, which means that the deformation continues to happen during the test.

Table 5.1 shows the mean absolute error during compression $\xi_{\Delta F}$ between $32\% < V_f < 61\%$ and the error at the end of compression $\xi_{\Delta F,end}$. For the closing speed of $\dot{h} = 6$ mm/min, a fluid viscosity of $0.5 < \mu < 1$ Pa.s would be the choice to avoid deformation. Above this value, the error increases drastically, representing a larger fiber-tow washout.

Fluid viscosity (Pa.s)	0.5	1	5	10
Closing mold speed (mm/min)	6	6	6	6
$\xi_{\Delta F}(\%)$	9	48	401	809
$\xi_{\Delta F,end}(\%)$	45	87	516	676

Table 5.1: Mean absolute error between experimental tests and theoretical Darcy's model for the INCREASE06 interlock

5.5.1 Apparent permeability K_e of the deformed interlock

If the fluid force extracted from a deformed state is used to calculate the equivalent in-plane permeability of the fabric using Equation 5.3 it will lead to an overestimation of the permeability since the structure will be more open in comparison to its undeformed nominal state.

$$K_{\mathrm{e}}(h) = -\frac{\mu \dot{h} \pi R^4}{8h\,(F_z^{\text{saturated}} - F_z^{\text{lubricated}})} \tag{5.3}$$

Figure 5.5 shows the equivalent in-plane permeability calculated using the saturated compression tests previously described. At the same iso-speed of $\dot{h} = 6$ mm/min the higher the fluid viscosity used, the more the apparent K_e deviates from the reference value (calculated with a fluid viscosity of $\mu = 0.50$ Pa.s). Hence it is important to verify and ensure that the compression test will not generate in-plane deformation thus changing and opening the fabric's structure.

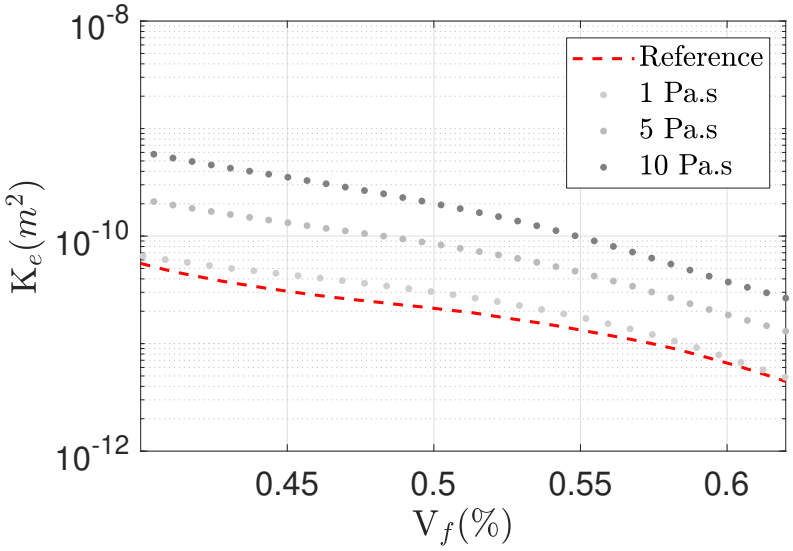

Figure 5.5: Equivalent permeability of Interlock INCREASE06 at iso-speed $\dot{h}$= 6 mm/min and varying fluid viscosity μ.

The lowest fluid viscosity value that was still able to generate a higher total force F_{tot} than the lubricated test F_{lub} (Equation 5.1) was $\mu = 0.50$ Pa.s, therefore creating the least amount of flow induced deformation. A compromise has to be found between high enough fluid pressure for sensitivity of the method and low enough fluid pressure not to deform the preform.

5.5.2 Partial conclusion

The theoretical model based on conservation of mass and Darcy's equation considers that the reinforcement fabric does not deform in-plane, only transversely due to compression. In reality, the fiber-tow washout will occur if the fluid viscous-drag forces are larger than the friction between the tows.
The drag force increases with the augmentation of the fluid viscosity or closing mold speed. The occurrence of in-plane deformation manifests when the experimental fluid force measured deviates from the theoretical fluid force calculated using Darcy's law. The higher the drag force, in this case due to the increase on fluid viscosity μ, the more the experimental results deviate from the theoretical model.
The apparent isotropic in-plane permeability calculated using a deformed fiber reinforcement will appear larger than of its nominal state since the tow's washout will increase the spacing between the tow (Figure 5.6).

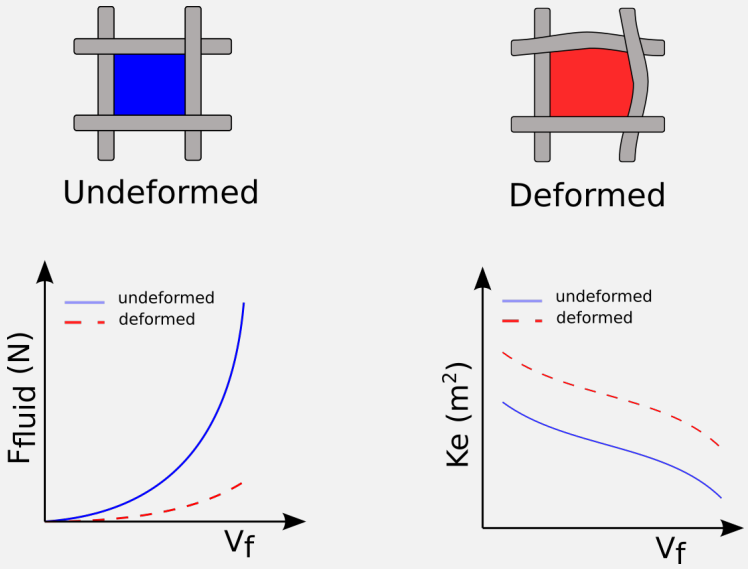

Figure 5.6: Schematic comparison of fluid force response during compression and equivalent permeability of un-deformed and deformed saturated fabrics

For a specific resin viscosity, the process parameters such as the closing mold speed must be chosen accordingly in order to preserve the desired fabric structure and to not generate a too high internal fluid pressure. For that, the limiting drag force must be calculated to create a processing window for the interlock fabric.

5.6 Process window definition

After collecting the data from the saturated compression tests a processing window for the saturated compression technique can be created. This window represents the process limits (closing mold speed $\dot{h}$) for a range of model fluid viscosity. The maximum drag force $\mathbf{f}_d$ generated without in-plane fiber tow washout (deviation from theoretical model) will serve as limiter of the processes.

5.6.1 Drag force

In fluid dynamics, drag is a force acting opposite to the relative motion of any object moving with respect to a surrounding fluid. The drag force is proportional to the velocity for a laminar flow.

Slattery et al.[66] described the drag force $\mathbf{f}_d$ of a single-scale porous medium as the constitutive relation:

$$\mathbf{f}_d = \phi\mu\mathbf{K}^{-1}[< \boldsymbol{v}_l^l > - < \boldsymbol{v}_s^s >] \tag{5.4}$$

where ϕ is the fiber reinforcement porosity (1-V_f), $< \boldsymbol{v}_l^l >$ and $< \boldsymbol{v}_s^s >$ are respectively the intrinsic phase average velocities of the fluid and solid phases and $\boldsymbol{K}$ is the permeability tensor.

Pillai [55] showed that the same relation can be used for a double-scale reinforcement. Using Darcy's Law [17], this drag force can be directly linked to the pressure gradient and porosity of the the fabric as seen in Equation 5.5:

$$\mathbf{f}_d = \phi\nabla P \tag{5.5}$$

where P is the fluid pressure.

In liquid composite molding (LCM) such as the C-RTM process, the fluid pressure P can increase by augmenting the fluid viscosity μ and the mold closing speed $\dot{h}$.

Today, to minimize processing time, high compaction velocities and flow rates are applied and a wide variety of resins are in use, therefore increasing the fluid–solid viscous drag force. As a consequence, it is important to ensure that the force generated will not deform and modify the fiber reinforcement mesostructure during the process.

5.6.2 Process window for saturated compression tests and for industrial C-RTM process

Figure 5.7 shows the processing window for the saturated compression technique. The dotted line is represented by the function:

$$\dot{h} = \alpha \cdot \mu^{-1} \tag{5.6}$$

It limits the transition from a filtration flow regime (no deformation) to a flow induced convection of the tows (deformation). The coefficient α is the product of the compression speed $\dot{h}$ and fluid viscosity μ.

To calculate the maximum drag force $\mathbf{f}_d$ using Equation 5.5, firstly the maximum fluid pressure P of the limiting combination $(\dot{h}, \mu)$ before deformation will be calculated with Equation 5.7:

$$P = \frac{\mu\dot{h}R^2}{K_e h} \tag{5.7}$$

The limit $\mathbf{f}_d = 2.4 \times 10^{07}$ N/m^3 is calculated using with the reference values of $\mu = 0.5$ Pa.s and and the equivalent isotropic permeability K_e and thickness h at $V_f = 60\%$ since

any higher viscosities created a deviation from the theorical Darcy's model as quantified in Table 5.1.

Below this line (green area) the closing mold speed $\dot{h}$ and fluid viscosity μ generate a smaller drag force $\mathbf{f}_d$ than the limit to avoid fiber-tows washout.

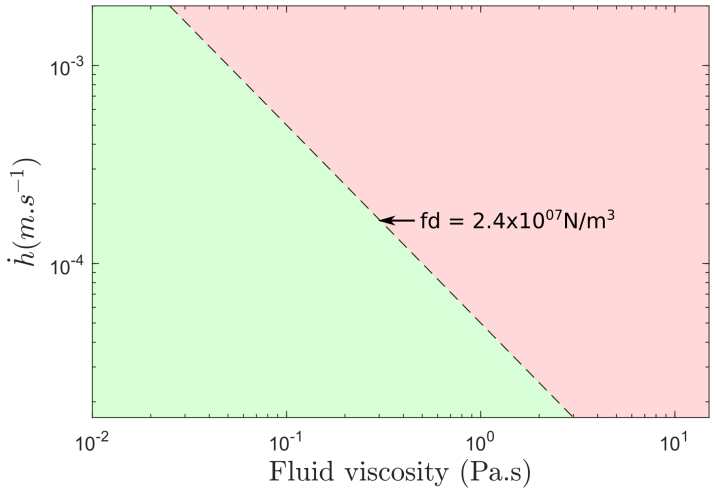

Figure 5.7: Process window for the saturation compression tests of INCREASE06. The combination of $(\dot{h}, \mu)$ in the green area maintains no transport of tows whereas in the red area the process parameters will induce fiber-washout.

To transpose the process to the industrial manufacturing of a C-RTM plate the processing window was adapted to the size of the component and can be seen in Figure 5.8. The dimensions of the component are 800mm×340 mm and the viscosity of the resin used in the process is of approximately $\mu = 0.02$ Pa.s. The proposed closing speed that generates a drag force $\mathbf{f}_d$ below the limit is of $\dot{h} = 0.6$ mm/s.

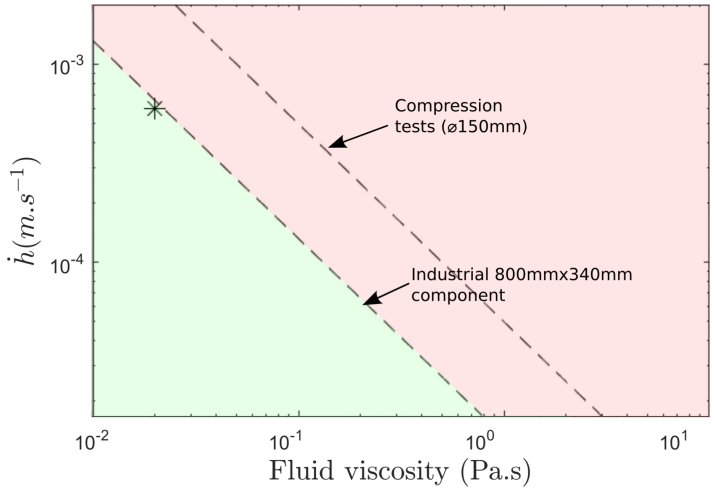

Figure 5.8: Process window of INCREASE06 for C-RTM process of a plate with dimensions 800×340.

5.6.3 Partial conclusion

The saturated compression tests can be used to create a processing window that bounds the parameters to avoid the occurrence of flow induced deformation.

The limit corresponds to the couple μ and $\dot{h}$ that generated the highest drag force $\mathbf{f}_d$ without deforming the fiber-reinforcement structure (smallest deviation ΔF from experimental $F_{\text{fluid ,exp}}$ and theoretical fluid force $F_{\text{fluid},th}$)

This processing window can be adapted industrially to the dimensions of the interlock plate and the resin viscosity $\mu = 0.02$ Pa.s. A maximum closing speed of $\dot{h} = 0.6$ mm/s is proposed to avoid tow-washout during the C-RTM process.

5.7 Signature and interpretation of compression blind tests

Traditional 2D weaving is done by interlacing two sets of orthogonal yarns (the weft and the warp) intersected at right angles (Figure 5.9). In an interlock fabric, the interlacing happens as well between two adjacent layers (Figure 5.10). The warp (or weft) yarns are used to bind several layers of the structure together, increasing the stiffness and strength in the thickness direction [5].

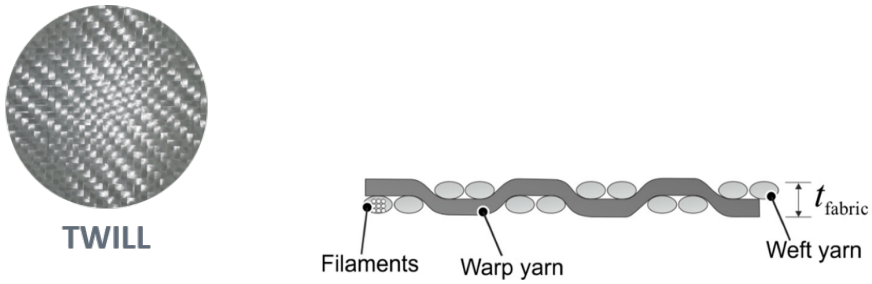

Figure 5.9: Top view (left) and schematic cross section of a twill weave (right) [43]

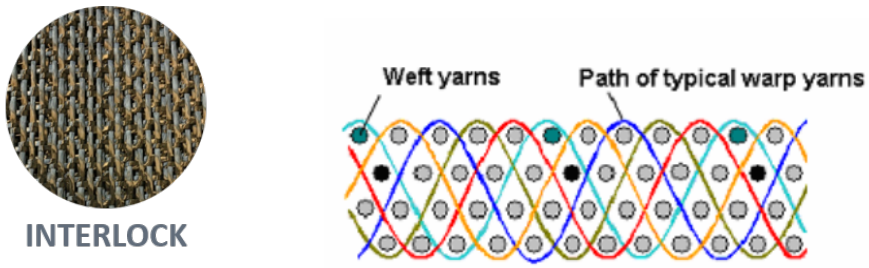

Figure 5.10: Top view (left) and schematic cross section of an interlock weave (right) [5]

When examining the permeability signature curves of the twill weave and the interlock fabric, as depicted in Figure 5.11 (a) and (b) respectively, key differences can be observed in terms of how the weaving pattern influences the movement of the fiber tows.

Figure 5.11 (a) shows the characteristic shape of the compression tests for the twill weave (G-Weave 600T PA) at different viscosities. At the initial stage of compression, regardless of the viscosity, the equivalent permeability of the 2D twill weave remains consistent, representing an undeformed configuration (point A). However, as the compression

progresses and the fiber volume increases, the equivalent permeability of the twill weave deviates further from the reference value (moving from point C to point B with increasing viscosity).

The twill weave's simple weave pattern and the lack of binding yarns allow the tows to move freely, particularly at the edges of the sample as seen in Figure 2.15. As a result, the deformation continues and intensified during the compression and increases with the augmentation of fluid viscosity.

The mechanical signature observed for the interlock fabric differs significantly from that of the twill weave. The tows of the interlock fabric exhibit high mobility in an uncompacted state, even for low viscous drag forces possibly due to a looser weaving structure, as shown in Figure 5.11 (b). In the initial stages of compression, there is a notable deviation between the reference uncompressed permeability and the permeability calculated using higher viscosity fluids (point D).

However, the tows are less prone to movement since the transverse yarns that bind the structure can hold the tows to a determined position. Consequently, as the compression progresses, the deviation between the permeability curves does not evolve anymore, resulting in a characteristic "S" curve. Notably, at approximately Vf = 50%, the curves tend to converge towards a locked deformed configuration (point E), indicating a more stable and consistent behavior during compression.

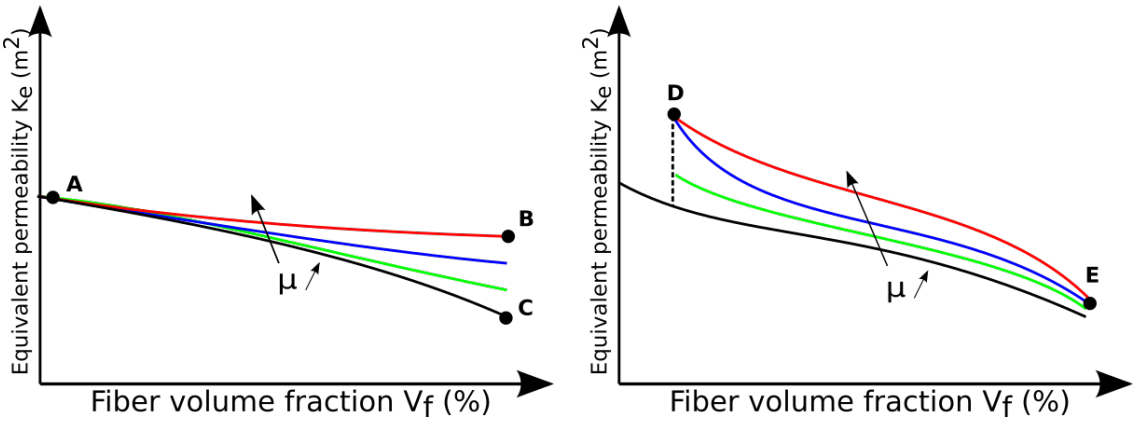

Figure 5.11: In-plane deformation signature of a 2D weave (a) and a 3D weave (b) during saturated compression with increase in viscosity μ

It appears that the binding yarns do not only increase the stiffness of the structure in the thickness direction but also serve as barrier to hold the tows in-plane. It is clear that tow movement occurs during the compression when a higher viscosity fluid is used however, due to the binding yarns, the displacement might not be as extensive for the interlock fabric as it was observed with the 2D weave.

Direct optical visualization is not feasible for carbon fiber reinforcement as it was done for the twill glass (Figure 2.15) so the combination of glass fiber tow tracers and a micro CT scan is proposed to observe the type of deformation and quantify it in the future. This experiment is explained in details in Section 5.10.

5.7.1 Partial conclusion

The mechanical signatures to compression differ between different materials. The twill weave is free to deform indefinitely due to lack to binding yarns and it shows how the apparent permeability behaves during compression.

The interlock fabric has transverse binding yarns that "lock" the reinforcement to a deformed position, this behavior can be seen on its characteristic signature when compared to the twill.

The binding yarns might not only serve to increase the transverse stiffness of the fabric buts also to keep hold the structure in position. A complementary test such as a micro-CT scan should be performed in order to assess visually what is the final degree of deformation at the end of compression and how it would affect the final part.

5.8 Consolidation of an anisotropic fabric

The previous section used the saturated compression technique to calculate the in-plane equivalent permeability K_e. By exchanging the circular compression platen for a rectangular one as illustrated in Figure 5.12 two independent tests can be performed and the permeability in the fabric's main directions (weft and warp) can be measured.

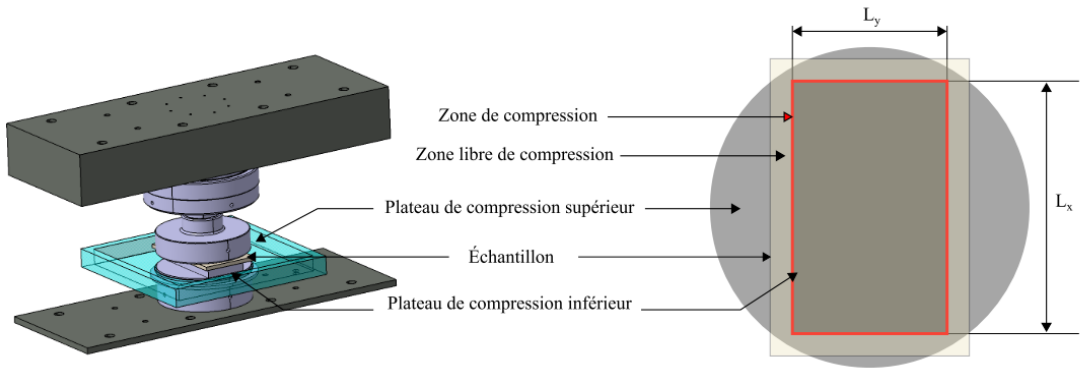

Figure 5.12: Saturated compression set-up for the extraction of the main permeabilities K_x and K_y of an anisotropic fabric [27])

The rectangular samples used in the experiments were cut in orthogonal orientations to one another. In the "F_x" test configuration, the longer side of the rectangular platen (L) is aligned parallel to the warp tows. On the other hand, in the "F_y" configuration, the longer side of the rectangular plate is aligned parallel to the weft tows, as shown in Figure 5.13.

The difference in permeability between the warp and weft directions, represented by K_x and K_y respectively, results in distinct responses to compression.

The two test configurations are used to extract the fluid pressure P and then the permeabilities are calculated using an inverse method [41] by comparing the experimental fluid pressure ($F_{\text{fluid,exp}}$ integrated over the rectangular platen area) and P calculated from the 2D consolidation equation [25]:

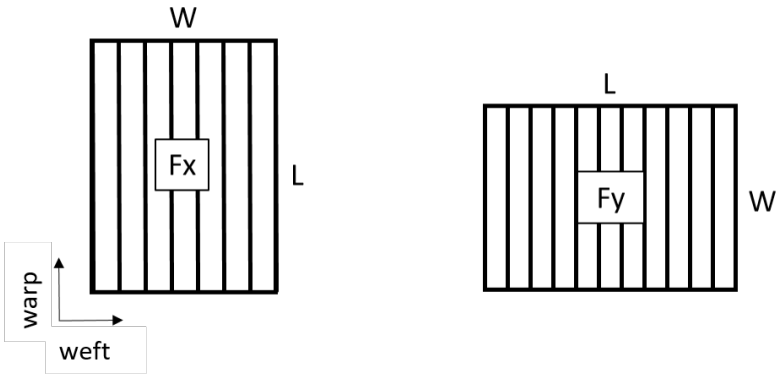

Figure 5.13: Sample configuration for F_x and F_y tests

$$K_x \frac{\partial^2 P}{\partial x^2} + K_y \frac{\partial^2 P}{\partial y^2} = -\mu \frac{\dot{h}}{h} \tag{5.8}$$

5.8.1 Influence of viscosity

Due to the permeability anisotropy of the interlock, the pressure field generated is different between the F_x and F_y testing configurations. The drag force $\mathbf{f}_d$ is, therefore, also different between tests. As described previously, the viscous-drag force should be lower than the tow's friction to avoid flow-induced deformation. If deformation occurs, the hypothesis of in-plane rigidity is no longer valid and Equation 5.8 cannot be solved.

Figure 5.14 shows the compression results for the F_x and F_y testing configurations. The mold closing speed is $\dot{h} = 6$ mm/min and the viscosity $\mu = 0.5$, 1 and 5 Pa.s. The response of the F_x configuration (Figure 5.14 (a)) did not increase with increasing the fluid viscosity, on the contrary, the highest response was of the lowest viscosity $\mu = 0.5$ Pa.s. That behavior can be explained if both $\mu = 1$ Pa.s and $\mu = 5$ Pa.s deform the fiber reinforcement structure and therefore the fluid response is much lower. The same is not observed for the F_y configuration, the increase in response is more coherent to the augmentation in fluid viscosity. Both graphs indicate that the pressure fields produced are different and the fabric's deformed state are not comparable.

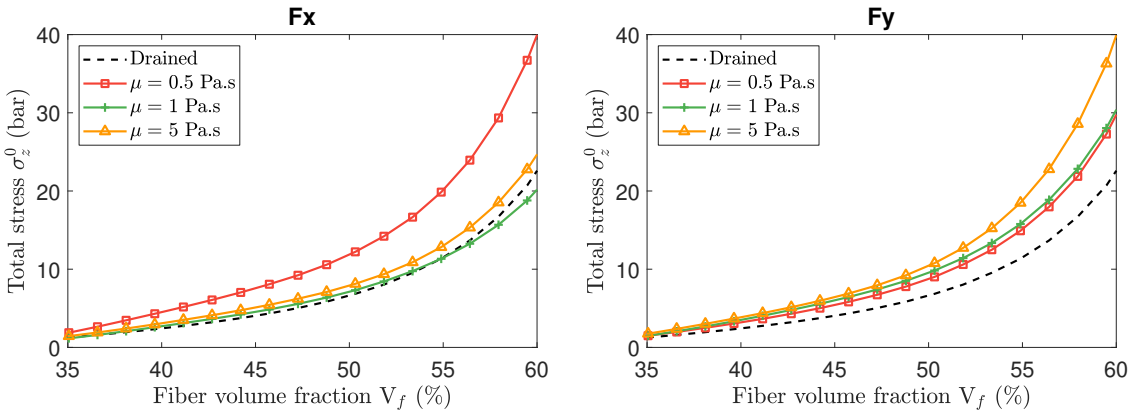

(a) (b)

Figure 5.14: Saturated compression stress σ_z of INCREASE06 at iso-speed $\dot{h} = 6$ mm/min and varying fluid viscosity μ for F_x and F_y configuration

5.8.2 Comparative quasi-UD fabric

A quasi-UD fabric (described in Section 3.1.3) will serve as comparative reference of anisotropic behavior under compression and it will be tested the same way as the interlock fabric. Both the mechanical response and respective deformation field were fully characterized in the work of Hautefeuille [27].

5.8.3 Influence of viscosity

The quasi-unidirectional glass fabric (UDT-400P) was compressed using the same platen configuration and fluid viscosity of $\mu = 0.1$, 0.5, 1 and 5 Pa.s. Figure 5.15 (a) shows that the response to compression in the F_x configuration did not increase as much as the F_y one. Like the interlock, the permeability od the quasi-ud in the warp direction K_x is higher than on the weft direction K_y (Figure 3.4).

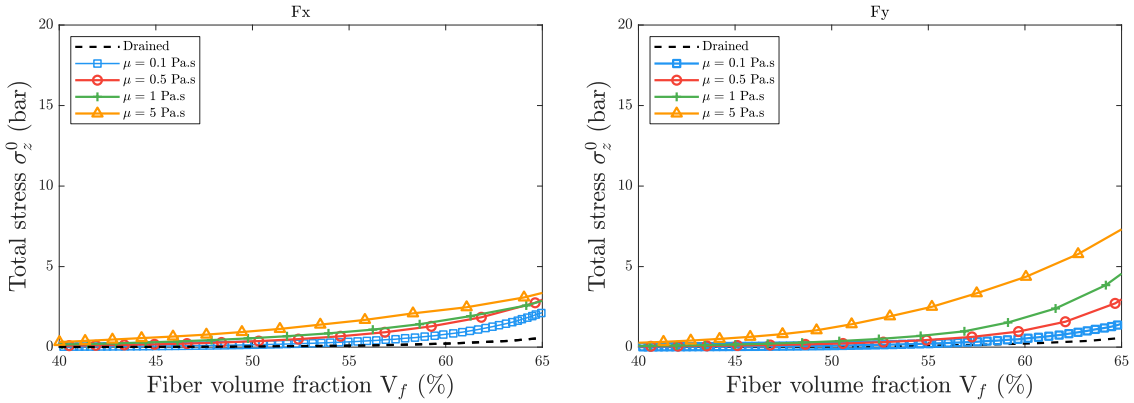

(a) (b)

Figure 5.15: Total compression stress σ_z of UDT-400P at iso-speed $\dot{h} = 1$ mm/min and varying fluid viscosity μ. F_x (a) and F_y (b) configurations

The experimental tests were compared to the theoretical static Darcy's model, solving Equation 5.8 using finite differences. The results for the testing configurations F_x and F_y are shown in Figure 5.16:

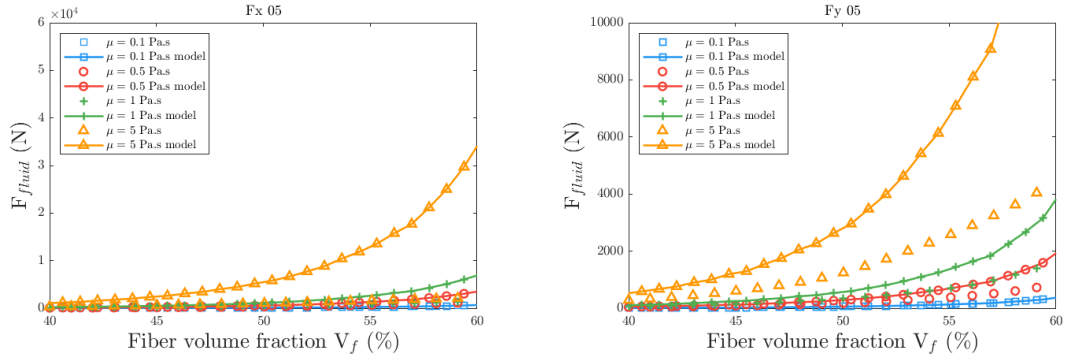

(a) (b)

Figure 5.16: Theoretical and experimental fluid force of the UDT-400P fabric measured at iso-speed $\dot{h} = 1$ mm/min and varying viscosity μ for F_x (a) and F_y (b) configurations using a rectangular compression platen of aspect ratio 0.5.

The deviation from the theoretical model increases with the augmentation of fluid viscosity. When comparing the deviation ($\Delta F = F_{\text{fluid},th}$ - $F_{\text{fluid,exp}}$) between both F_x and F_y configurations it is clear that the F_x configuration deforms more than the F_y one as shown in Figure 5.17. Table 5.2 show the mean absolute error $\xi_{\Delta F}$ for $40\% < V_f < 60\%$.

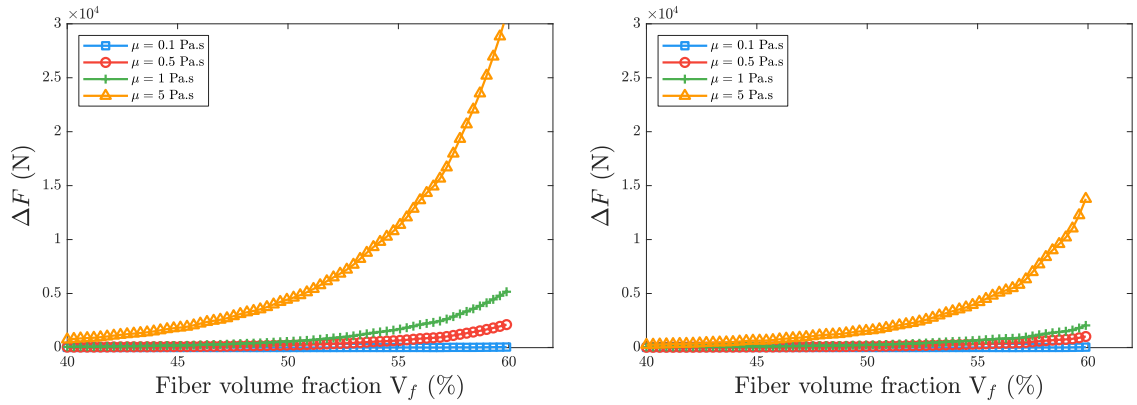

Figure 5.17: Deviation ΔF between theoretical $F_{\text{fluid},th}$ and experimental $F_{\text{fluid,exp}}$ fluid force at $\dot{h} = 1$ mm/min of the UDT-400P fabric. F_x (a) and F_y (b) configurations.

The difference in deviation between the F_x and F_y configurations means that one configuration is more deformed than the other at the same fiber volume fraction. The samples are then not comparable and the main permeabilities K_x and K_y cannot be extracted.

Fluid viscosity (Pa.s)	0.1	0.5	1	5
Closing mold speed (mm/min)	1	1	1	1
$\xi_{\Delta F_x}(\%)$	4	74	127	533
$\xi_{\Delta F_x,end}(\%)$	5	164	330	1382
$\xi_{\Delta F_y}(\%)$	5	63	76	142
$\xi_{\Delta F_y,end}(\%)$	8	118	123	313

Table 5.2: Mean absolute error between experimental curve and theoretical Darcy's model for UDT-400P

5.8.4 Displacement field

Hautefeuille [27] measured the displacement of the UDT-400P fabric in plane. He observed that at V_f= 59% there is a larger area deformed in the F_x configuration in comparison to the F_y configuration as seen in Figure 5.18. This result is coherent with the measurements shown in Figure 5.17 and Table 5.2.

To decrease the differences in deviation between both configurations, a new compression platen will be produced.

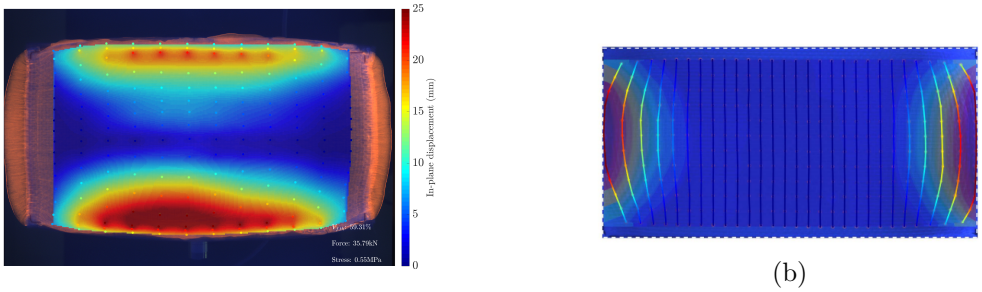

(a) (b)

Figure 5.18: UDT-400P displacement field F_x (a) and F_y (b) configurations [27]

5.8.5 Partial conclusion

During the consolidation of a saturated anisotropic reinforcement material, the fluid pressure P is influenced by the fabric's anisotropy. A rectangular compression platen can be used to create two independent tests in order to calculate the permeability in the weft and warp directions. The equation 5.8 can then be solved via inverse method to calculate the principal permeabilities K_x and K_y.

The fiber tow-washout happens when the viscous-drag forces $\mathbf{f}_d$ are larger than the friction between tows. Since the pressure field differs between the F_x and F_y test configurations, if the fluid viscosity or mold closing speed are high enough the samples will deform differently, making test results non comparable and therefore the permeabilities K_x and K_y cannot be extracted.

A new rectangular platen that has a lower aspect ratio will be tested with the purpose of attempting the decrease of the differences between the pressure fields while still maintaining 2 distinct aspect ratios to keep the tests independent.

5.8.6 New compression platen with lower aspect ratio

The theoretical pressure field of a quasi-UD fabric (UDT-400P) during saturated compression was calculated using finite differences. The fluid pressure field generated using a compression plate of aspect ratio 0.5 is shown in Figure 5.19:

The maximum fluid pressure ratio, $P_{\max}$, between the F_x and F_y configurations is 2.2 (Table 5.3), leading to a larger deformation in the F_x configuration compared to the F_y one (Figure 5.18). To minimize this difference, a new platen with a lower aspect ratio of 0.8 is analyzed. The fluid pressure profile for this platen is shown below in Figure 5.20:

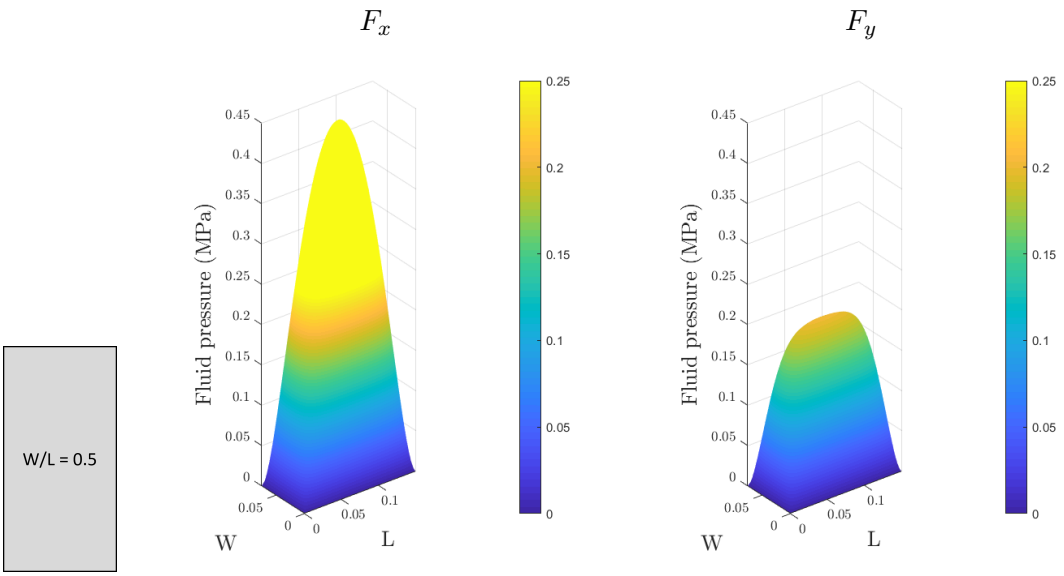

Figure 5.19: Pressure field of F_x (left) and F_y (right) test configuration of a saturated quasi-UD fabric UDT-400P and rectangular compression platen of dimensions 150×75 mm at $V_f = 60\%$

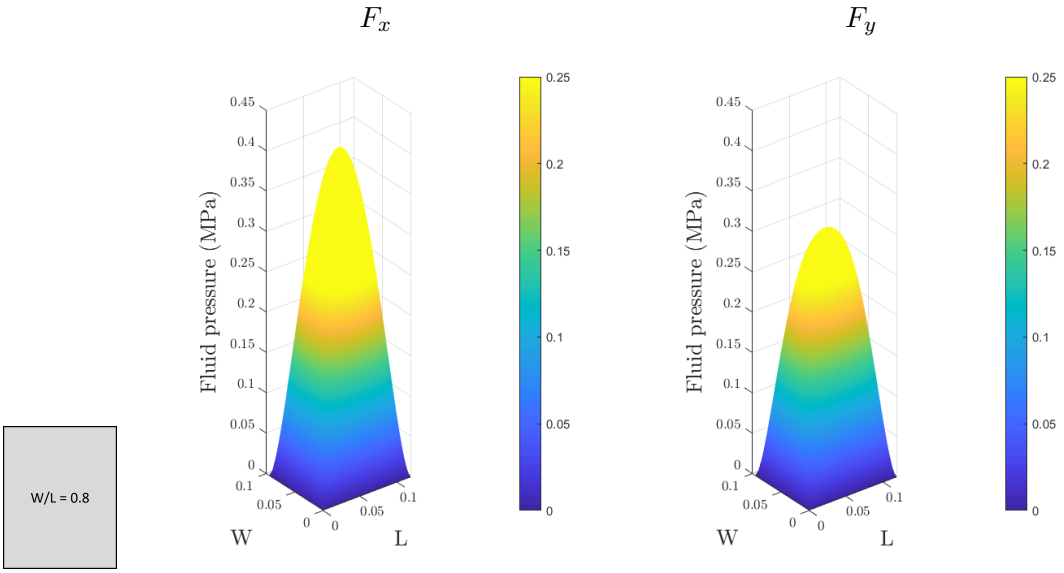

Figure 5.20: Pressure field of F_x (left) and F_y (right) test configuration of a saturated quasi-UD fabric UDT-400P and rectangular compression platen of dimensions 118.5×94.9 mm at $V_f = 60\%$

Table 5.3 shows the values of the maximum pressure P_{max}, average pressure P_{ave} and the pressure ratio between the configurations. The ratio of P_{max} and P_{ave} have decreased with the change in the platen aspect ratio.

The same tests were repeated using the quasi-UD fabric UDT-400P, closing speed $\dot{h}$ = 1mm/min and fluid viscosity of μ = 0.1, 0.5, 1 and 5 Pa.s but now with the new platen with aspect ratio 0.8.

Figure 5.21 shows that with the new platen, now the F_x configuration increases in response to the increase of fluid viscosity in similar way as the F_y configuration does.

Platen aspect ratio	Test configuration	P_{max} (bar)	$\frac{P_{max,x}}{P_{max,y}}$	P_{ave} (bar)	$\frac{P_{ave,x}}{P_{ave,y}}$
0.5	F_x	4.4	2.2	2.1	1.9
	F_y	2		1.1	
0.8	F_x	4	1.33	2	1.25
	F_y	3		1.6	

Table 5.3: Maximum P_{max} and average P_{ave} fluid pressure for F_x and F_y configurations and compression platens with 0.5 and 0.8 aspect ratio

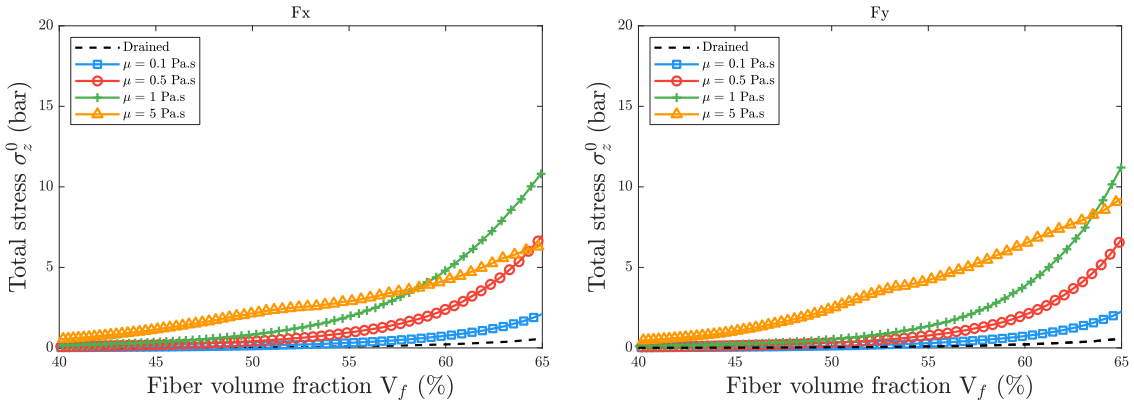

(a) (b)

Figure 5.21: Saturated compression stress σ_z of UDT-400P at iso-speed $\dot{h} = 1$ mm/min and varying fluid viscosity μ for F_x (a) and F_y (b) configurations

When comparing the experimental fluid force with the theoretical force derived from the static Darcy's model (Equation 5.8), it is evident that the deviation has been reduced for both the F_x and F_y test configurations. The implementation of a lower aspect ratio platen has minimized the pressure difference between the two configurations and resulted in a more balanced response.

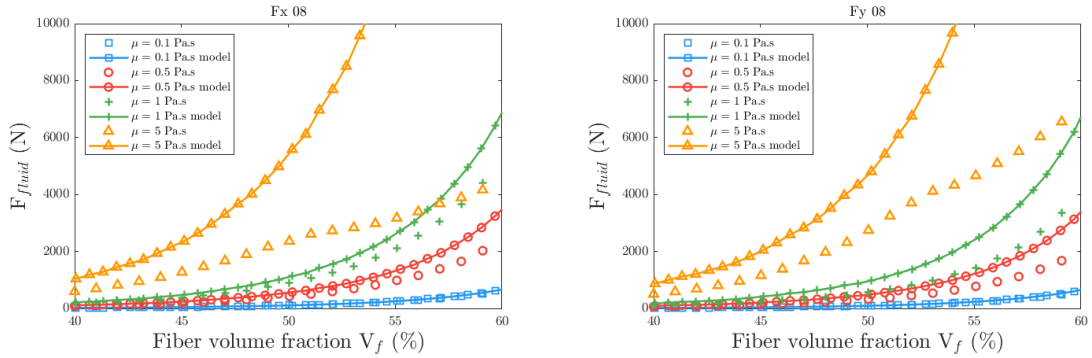

(a) (b)

Figure 5.22: Theoretical and experimental fluid force of the UDT-400P fabric measured at iso-speed $\dot{h} = 1$ mm/min and varying viscosity μ for F_x (a) and F_y (b) configurations using a platen of aspect ratio 0.8.

Figure 5.22 shows the experimental fluid force $F_{\text{fluid,exp}}$ and the theoretical fluid force

$F_{\text{fluid},th}$ calculated with Equation 5.8. The deviation ΔF between the theoretical and experimental fluid forces can be seen in Figure 5.23 and the absolute mean error at the end of compression from $40\% < V_f < 60\%$ can be seen in Table 5.4.

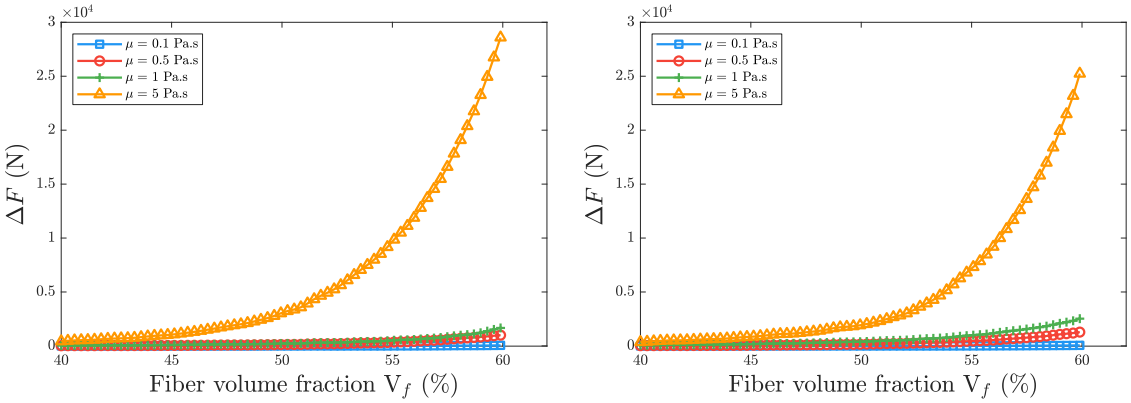

Figure 5.23: Deviation ΔF between theoretical $F_{\text{fluid},th}$ and experimental $F_{\text{fluid,exp}}$ fluid force at $\dot{h} = 1$ mm/min of the UDT-400P fabric for F_x (a) and F_y (b) configurations using a platen of aspect ratio 0.8.

The deviation decreased with the new platen of aspect ratio 0.8 (Table 5.4) in comparison to the one with ratio 0.5 (Table 5.2).

Fluid viscosity (Pa.s)	0.1	0.5	1	5
Closing mold speed (mm/min)	1	1	1	1
$\xi_{\Delta F_x}(\%)$	3	30	24	210
$\xi_{\Delta F_x,end}(\%)$	8	41	33	640
$\xi_{\Delta F_y}(\%)$	3	52	59	123
$\xi_{\Delta F_y,end}(\%)$	9	63	62	360

Table 5.4: Mean absolute error between experimental curve and theoretical Darcy's model for a rectangular platen of aspect ratio W/L = 0.8

Table 5.5 compares the $\Delta F_x/\Delta F_y$ error between both platens. For the lowest viscosity $\mu = 0.1$ Pa.s, the deviation between the F_x and F_y tests is small. While as the fluid viscosity increases, the difference between both configurations is less pronounced with the new platen of aspect ratio 0.8.

The results suggest that utilizing a platen closer to a square shape for the UDT-400P reinforcement material can effectively reduce the disparity in flow-induced deformation between the F_x and F_y configurations. This reduction in deformation difference enables the extraction of the permeabilities K_x and K_y from a more similarly deformed configuration and also allows for the possibility of using higher fluid viscosities, if necessary, while maintaining a balanced deformation response between the two configurations.

	Fluid viscosity (Pa.s)	0.1	0.5	1	5
	Closing mold speed (mm/min)	1	1	1	1
W/L = 0.5	$\xi_{\Delta F_x/\Delta F_y}(\%)$	0.82	1.17	1.66	3.75
	$\xi_{\Delta F_x,end/\Delta F_y,end}(\%)$	0.74	1.39	6.67	4.41
W/L = 0.8	$\xi_{\Delta F_x/\Delta F_y}(\%)$	0.93	0.59	0.35	1.70
	$\xi_{\Delta F_x,end/\Delta F_y,end}(\%)$	0.95	0.66	0.52	1.77

Table 5.5: Mean absolute error between experimental curve and theoretical Darcy's model

5.9 INCREASE06 compression tests with platen of W/L = 0.8

After the deformation analysis done on the anisotropic fabric UDT-400P and the production of a new compression platen, the INCREASE06 test were redmade with the lowest viscosity $\mu = 0.5$ Pa.s and the compression platen with the aspect ratio 0.8. The test results can be seen in Figure 5.24:

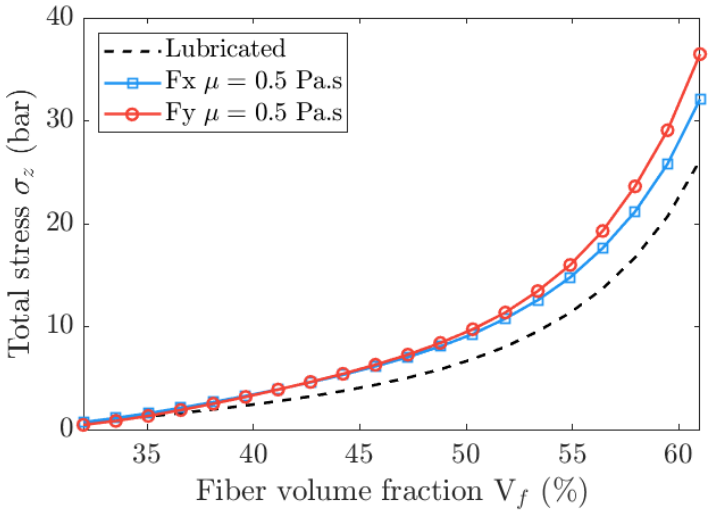

Figure 5.24: Total saturated compression stress σ_z of INCREASE06 at iso-speed $\dot{h} = 6$ mm/min and $\mu = 0.5$ Pa.S for the F_x and F_y configurations and compression platen of aspect ratio 0.8.

To asses the improvement of utilizing the new compression plate of aspect ratio 0.8, the equivalent isotropic permeabilities K_e will be compared. The reference K_e was calculated with Equation 5.3 (circular platen) and the lowest possible fluid viscosity of $\mu = 0.5$ Pa.s. The equivalent permeability from the anisotropic tests is calculated as the square root of the product of the main permeabilities ($K_e = \sqrt{K_x K_y}$).

Figure 5.25 shows that even though the use of a lower platen ratio improved the results of the quasi-UD fabric and allowed the use of a higher fluid viscosity without major deformation, the same was not observed during the compression of the INCREASE06 interlock.

Both permeabilities measured with the rectangular platen appear smaller than the isotropic K_e measured with the circular platen. It was already established the the tows

of the interlock fabric are quite mobile specially at the beginning ot the compression and this change in ratio was not sufficient to avoid movement. Therefore, to calculate the K_x and K_y continuously the protocol proposed in Section 4.8 using the anisotropic ratio of the radial injection still remains.

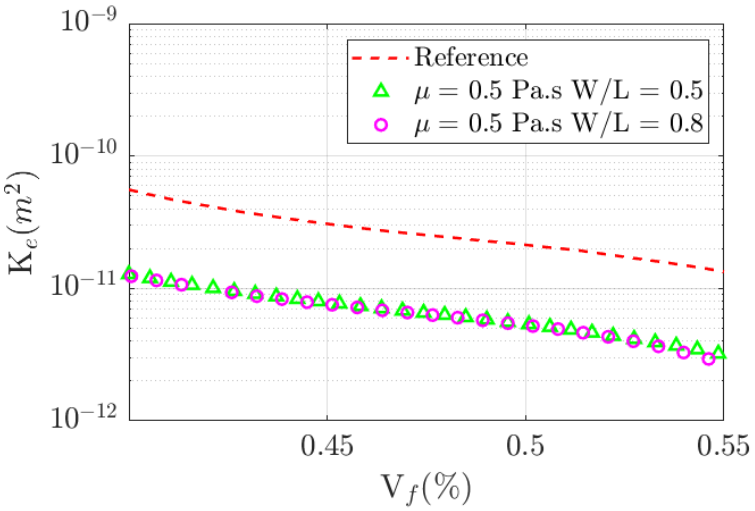

Figure 5.25: Equivalent permeability K_e calculated with a circular platen (reference) and $K_e = \sqrt{K_x K_y}$ calculated with the rectangular platen with aspect ratio 0.5 and 0.8. $\dot{h} =$ 6 mm/min and $\mu = 0.5$ Pa.s

5.10 Proposed experiment

The blind tests utilizing the saturated compression technique are effective in identifying the occurrence of fiber-tow washout during compression. However, the exact extent and type of deformation that takes place remain unknown.

To address this, an experimental approach is proposed to observe the effects of deformation in the final position of the tows of a finished part. Since carbon fiber reinforcements such as the INCREASE06 interlock are difficult to visually track and measure, the deformation can be observed with the use of tracers.

The idea is to incorporate glass tows as tracers during the weaving process of the interlock fabric. These glass tows can be strategically placed at specific locations, as illustrated in Figure 5.26 (a). Given the disparity in density between carbon and glass fibers, when the consolidated part is scanned using a Micro-CT, the internal structure can be visualized (Figure 5.26 (b)), allowing for a comparison between the deformed and undeformed states. Moreover, the contrast between carbon and glass would allow the optical tracking of the tows during compression with the the experimental set-up used for the radial injection tests [27, 28].

With this experiment, it will be possible to determine if the extent of deformation and in which location is more pronounced. The Micro-CT scans will provide valuable insights into the deformation behavior of the interlock fabric and help further understand its structural changes during compression.

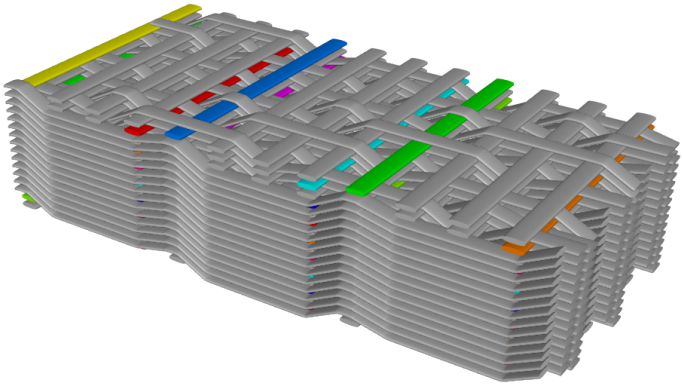

(a) INCREASE 06 with proposed warp traces. - made with Texgen

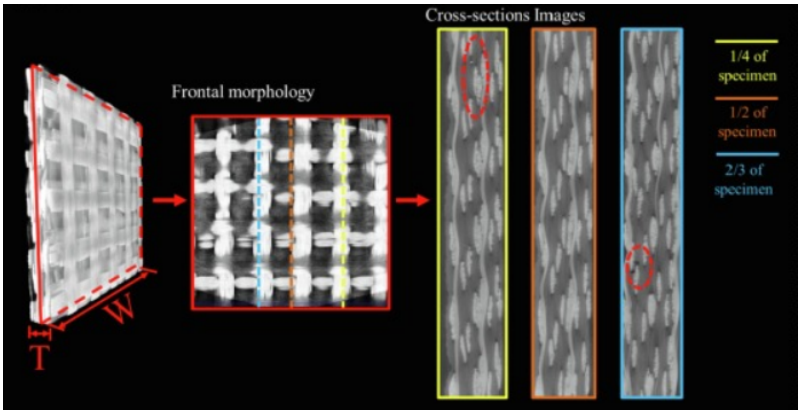

(b) Tomographic frontal morphology and the cross-section of a carbon-glass hybrid fabric [83]

Figure 5.26: Proposed flow-induced deformation experiment

5.10.1 Partial conclusion

The saturated compression technique can be used to extract the isotropic in-plane permeability K_e when a circular compression platen is used and for an anisotropic fiber reinforcement the main permeabilities K_x and K_y can be calculated by created two independent compression tests (rectangular platen).
Due to fabric's anisotropy, the pressure field generated between the two independent tests differs and the flow induced deformation will occur differently. A platen will a ratio closer to 1 (0.8) will generate a more uniform pressure field and therefore the deformation between tests will be more similar for the main permeability extraction using Equation 5.8.

5.11 Conclusion

In this chapter, a technique to blindly identify flow induced deformation was presented. For carbon fiber reinforcements, the visualization of deformation is difficult therefore the comparison of the experimental response to compression of a saturated fabric to the theoretical static darcean model can identify the occurrence of flow induced deformation without the need of visual assessment.

A processing window can be created using the compression tests to find the drag force $\mathbf{f_d}$ that limits the choice of closing mold speed $\dot{h}$ for a range of resin viscosity μ to guarantee that process parameters wont generate a high enough fluid pressure that will change the nominal fiber reinforcement structure.

To observe the extent and the location of the deformation, an experiment in which glass tows are added into the fabric is proposed. The glass tows will be uniformly spaced and after the consolidation of the part, then a micro-CT scan can be used to show the final position of the tows and which areas are criticality affected by the flow induced deformation deformation.

Chapter 6

Saturation rate measurement of a dual-scale fiber reinforcement

6.1 Introduction

In order to produce a good quality composite part, the interlock textile needs to be properly impregnated with resin and have the least amount of air bubbles or poorly impregnated regions. 3D geometries such as the interlock of this study requires complex processing conditions to ensure the impregnation quality of the part, i.e a part without residual porosity.

It was observed in-site during the C-RTM process that the part was not fully impregnated once the injection was completed. The macroscopic resin front reaches the vents while there are still air bubbles and partially impregnated volumes. A bleeding process was added at the end, in which the injection pressure is increased and kept high even after the arrival of the macroscopic flow front at the outlet.

Dense and twisted tow are particularly hard to impregnate during injection. Also, the large spacing between the tows creates a very pronounced double scale feature for this particular fabric.

In LCM processes, the majority of reinforcements have a dual-scale structure characterized by two distinct pore sizes that leads to two different impregnation mechanisms: micro-pores and meso-pores. Micro-pores refer to the spaces between individual fibers, typically on the scale of micrometers. On the other hand, meso-pores are the spaces between tows, which are larger in size, typically in the order of millimeters as shown in Figure 6.1:

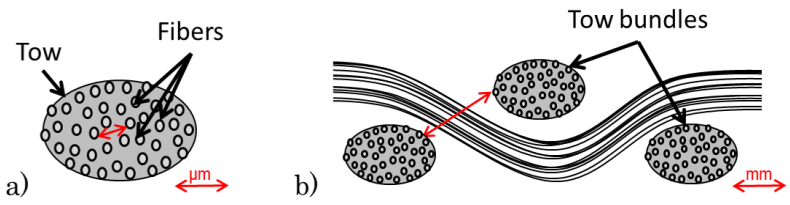

Figure 6.1: Schematic representation of (a) micropores between fibers and (b) macropores between tow bundles

Depending on the impregnation speed of the flow, different flow patterns can arise

and create an non uniform flow pattern. The capillary number Ca represents the relative effect of viscous drag forces versus surface tension forces.

$$Ca = \frac{\mu v_f}{\gamma} \tag{6.1}$$

where v_f is the fluid speed, μ is the fluid viscosity and γ the surface tension.

At a lower impregnation speed (low Ca), the flow is mostly driven by the capillary pressure and the tows are filled first which can cause air to be trapped between the tows (meso-porosity). On the contrary, at high impregnation speed (high Ca), which is the case during the C-RTM process, the viscous forces dominates the flow and the spaces between tows are filled first and micro-porosity can be created inside the tow bundles which are filled at last (Figure 6.2).

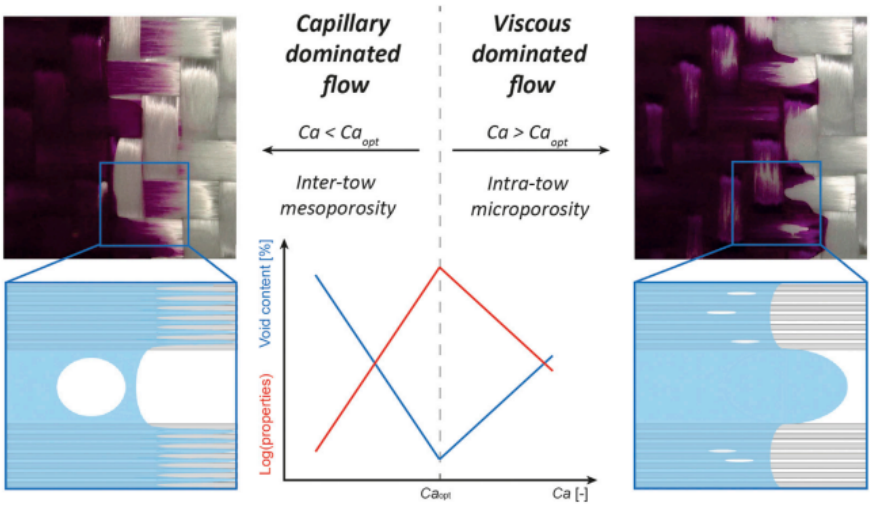

Figure 6.2: Influence of the capillary number on the void formation and final part properties during infiltration based on fluid paths in a glass twill fabric under capillary-and viscous-dominated flow regimes [68].

An uniform impregnation is desired to avoid any porosity due to the entrapment of air bubbles. Both porosity scales are considered as defects on the final composite part (Figure 6.3) and can compromise its desired mechanical properties.

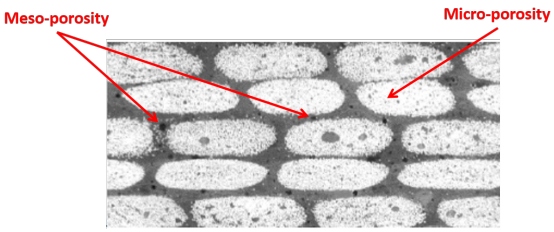

Figure 6.3: Mesoscopic and microscopic porosity in a double scale fabric [23].

In addition to what was observed industrially, the dual scale nature of the INCREASE06 fabric was clear during the permeability measurements described in Chapter 4. Observing the radial injection photos of INCREASE06 in Figure 6.4, it is clear that the large spaces between tows are being rapidly filled creating a non uniform flow front.

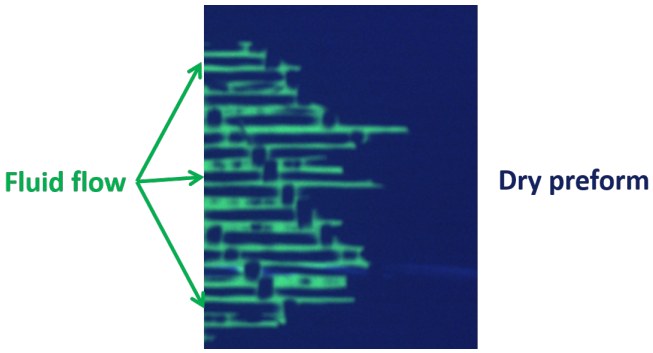

Figure 6.4: Zoom of flow front location during radial injection of INCREASE06 at $V_f = 60\%$.

It is very important to consider the different flows that occur during an impregnation of a dual scale fabric. Because of it, the extra time during bleeding is necessary for the C-RTM process.

Furthermore, when measuring the permeability of a dual-scale fabric using techniques that rely on visual observations of the flow front, it is important to note that the obtained permeability values correspond to unsaturated permeability (Figure 6.5).

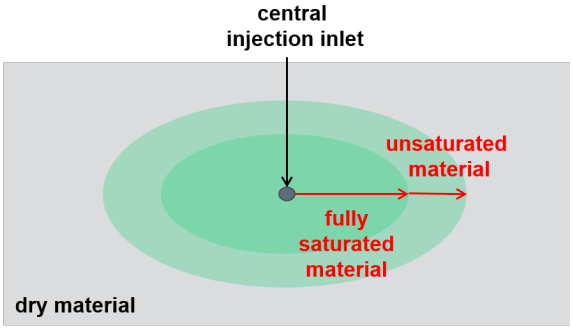

Figure 6.5: Schematic of the flow front observed during radial injection. If the fabric has an elevated dual scale, the flow front observed is not fully saturated.

The difference between the saturated permeability, that depends only on the geometrical characteristics of the fabric and does not change regarding the type of impregnation of the fluid and the unsaturated permeability can cause significant differences when simulating the flow. The unsaturated permeability is considered as a function of the relative permeability that will depend on the degree of saturation [10, 23] and the saturated (bulk) permeability.

This difference was observed when comparing the equivalent permeability of INCREASE06 using a transient technique (radial injection) and a steady-state method (saturated compression) that measures the saturated permeability of the fabric. Figure 6.6 shows that there is an overestimation of the permeability when using the injection technique in comparison to the saturated compression. Considering the injection pressure of 2 bar, it is assumed that the flow is mostly driven by the viscous forces which makes the flow front advance faster in the meso-pores than if it was fully saturating the micro and meso-pores at isovelocity.

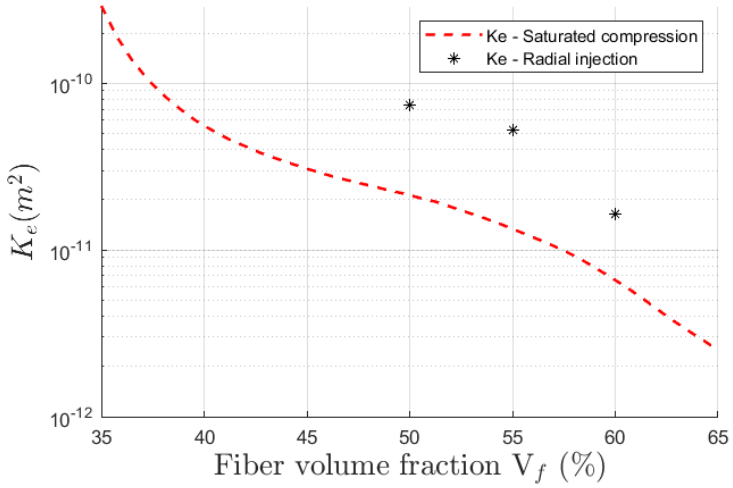

Figure 6.6: Equivalent in-plane permeability K_e calculated using saturated compression and radial injection techniques shown in Section 4.7.

The dual scale flow and therefore saturation of the fabric have a large impact in the permeability measurements. A good understanding of the impregnation during injection not only helps align the simulations with experimental observations but also provides valuable guidelines for selecting parameters in the C-RTM process. This includes determining the optimal duration for which the part should remain inside the mold after injection, ensuring proper saturation and impregnation of the fabric.

6.2 Motivation and Objectives

The use of an interlock fabric such as the INCREASE06 has many technical advantages in comparison to the laminate structures that are more commonly used [9]. Due to a lack of studies, the understanding of the behavior of the 3D structure is still restricted.

Usually in LCM simulations, it is assumed that behind the flow front the reinforcement is fully saturated and that can lead to predictions inaccuracies of, for example, filling time and flow front speed when comparing to real experiments [56, 54]. This was observed industrially during the C-RTM process and also when characterizing the permeability in the laboratory. The objective of this chapter is to present an experimental methodology to measure the saturation of the interlock INCREASE06 during injection. The technique must be able to measure the saturation blindly since the fabric is made of carbon fibers and the experimental bench must be adapted to a compression machine in order to achieve the three desired V_f, applying pressures above 10 bar.

The saturation evolution will allow a better characterization of the permeability and also serve as a guideline for the manufacturing parameters such as the over feeding time holding injection pressure during C-RTM.

6.3 Saturation

The saturation S of a material is defined as the ratio between the volume of fluid V_{fluid} and the total volume V_{total} within a representative volume of interest, considering a porosity

ε it can be defined as:

$$S = \frac{V_{fluid}}{\varepsilon V_{\text{total}}} \tag{6.2}$$

The saturation values goes from zero when there is no liquid (dry) to 1 when fully saturated. Attempts have been made to measure the saturation evolution during injection as reviewed by Michaud [44]. Labat et al. [36, 35] used a conductivity sensor to measure the change in conductance and correlates later to the change in saturation as function of time. Later, Guéroult [23] refined the method by measuring the dielectric properties of the fibrous reinforcement and fluid.

The dielectric measurement technique was chosen to identify both the saturated and unsaturated flow front of the INCREASE06 during injection. A experimental bench was design considering the specificity of the fabric (conductivity of carbon and elevated thickness) and will be described in the next sessions.

6.4 Dieletric sensor principle

The dielectric sensor uses a parallel copper plate capacitor in order to measure the change in saturation of the interlock fabric during injection. The capacitance C of the parallel plate capacitor determines the amount of charge it can hold. The value of C, as seen in Equation 6.3, depends on 3 factors:

- The area A of the plates
- The distance d between the plates
- The relative permittivity ε_r of the dielectric material between plates

$$C = \varepsilon_0 \varepsilon_r \frac{A}{d} \tag{6.3}$$

where ε_0 is the permittivity of the vacuum.

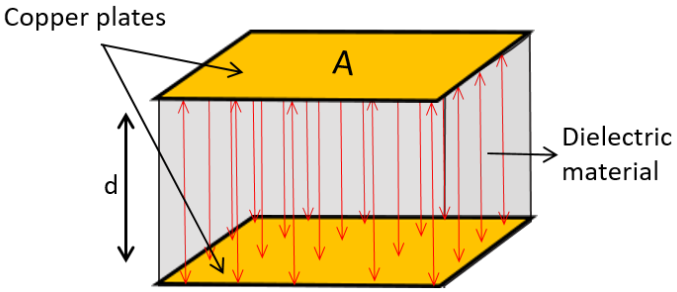

Figure 6.7: Parallel plate dielectric sensor with plate surface A and distance d between plates.

The impedance Z_C of a perfect capacitor is equal, in magnitude, to its reactance X_C as decribed by Equation 6.4:

$$Z_C = X_C = \frac{1}{\omega C} = \frac{1}{2\pi f C} \tag{6.4}$$

where w is the angular frequency in rad/s , C the capacitance and f the frequency in Hz.

The dielectric material, initially consists of air and fibers prior to the injection. As impregnation occurs, the air is replaced by a liquid until no air remains. Because no dielectric material is purely capacitive it can be modeled as a resistor and a capacitor in parallel configuration [80] as seen in Figure 6.8:

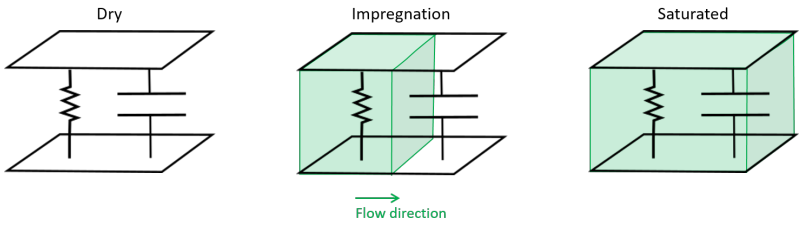

Figure 6.8: Dielectric material modeled as a resistor and capacitor in parallel

With the arrival of the fluid into the sensing region, the impedance Z_{Sensor} (Equation 6.5) will change since the permittivity ε_r so the X_c and resistance of the sensing area will change.

$$Z_{\text{sensor}} = \frac{1}{\frac{1}{R} + \frac{1}{X_C}} \tag{6.5}$$

Because of the higher permittivity of the fluid in relation to air, the impedance of the sensor will decrease during impregnation until the region is fully saturated:

$$Z_{dry} > Z_{impregation} > Z_{saturated}$$

This variation is proportional to the volume of fluid into the sensing region and will then be used to measure the degree of saturation in the region. An AC source feeds the sensor that is also connected in series to a reference resistor R_{ref}. The tension variation in the sensor V_{sens} can be calculated by measuring V_{ref} (Equation 6.6) and then transformed in saturation as it will be explained in Section 6.5.5.

$$V_{\text{sens}} = V_{\text{in}} - V_{\text{ref}} \tag{6.6}$$

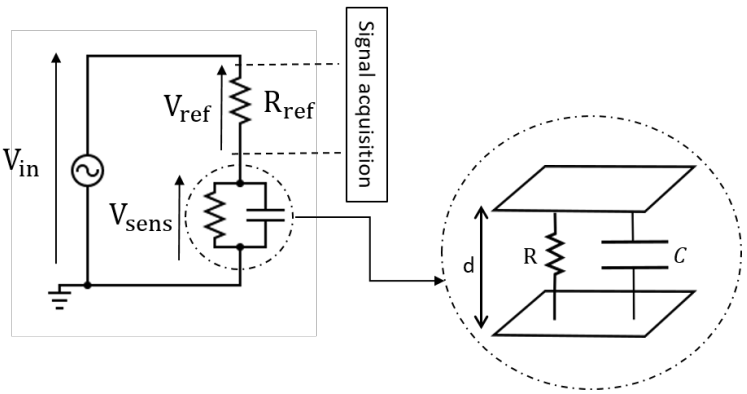

Figure 6.9: Schematic of a parallel plate dielectric sensor inserted in the electric circuit

6.5 Bench design

The bench was designed to measure the saturation of the INCREASE06 interlock fabric. The geometrical specificity of the sensor (area A and distance between plates d) as well the type of injected fluid (of relative permittivity ε_r) influence on the resulting capacitance of the sensor. Carbon fabrics such as the INCREASE06 interlock are conductive and will produce a low C however, the sensitivity of the system (measured voltage when the fabric is fully saturated minus the dry voltage) must be larger than the electrical circuit noise. To increase the sensitivity of the system, the size of the sensor and the type of injection fluid will be studied.

6.5.1 Electrical components

The two sensors $S1$ and $S2$ are connected to an AC source generator of amplitude $V_{in} = 20$ V and $f = 10$ kHz. Each sensors are connected in series to a reference resistors R_{ref1} and R_{ref2} both with a resistance of 10 $k\Omega$.

Electrical interference was observed during preliminary tests where the fluid arrival on one sensor would affect the measurement on the other sensor while still dry. In order to avoid interference between sensors, a set of 4 toggle switches were installed as seen in Figure 6.10. The purpose of the switches is to close and measure the tension of one circuit while the other one is open and vice-versa. The measurement is done sequentially, one sensor at a time.

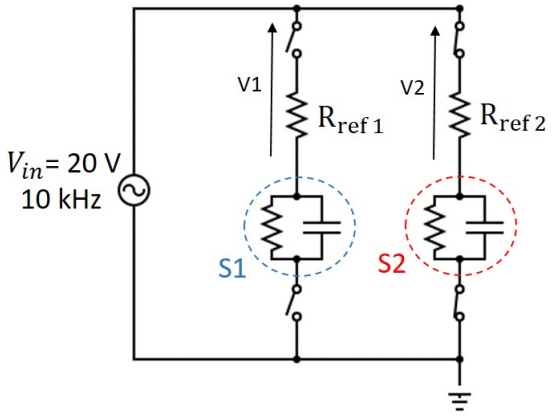

Figure 6.10: Circuit diagram of dielectric sensor installation representing the electrical components: S1 and S2 (Sensor 1 and 2), R_{ref1} and R_{ref2} (reference resistors), V_{in} (AC source) and toggle switches.

6.5.2 Sensor volume

Two sensors were tested: a smaller sensor of 2 × 2 cm and a larger sensor of 4 × 4 cm. The tests were made using both a commercial glass interlock Injectex and the INCREASE06 carbon interlock.

Both small and large sensors produced a large enough voltage variation ($\Delta V = V_{saturated} - V_{dry}$) when using the glass interlock for sensor visual validation as explained in Section 6.5.6. However, the smaller sensor creates a ΔV on the same order as the noise when used with the INCREASE06 fabric. Since glass is a dielectric material, the variation is more than 10 times what is obtained with carbon.

Therefore, the larger sensor was chosen to measure this particular carbon interlock fabric since its the one that produced a variation higher than the noise. Table 6.1 shows the measured voltage variation of both glass and carbon interlock fabrics.

Type of interlock	$\Delta V(V)$
Glass - Injectex	2.32
Carbon - INCREASE06	0.14

Table 6.1: Variation $\Delta V = V_{saturated} - V_{dry}$ comparison between the Injectex glass interlock and INCREASE06 carbon interlock using a sensor of 4 × 4 cm and a distance between plates of $d = 17$ mm, with $V_{in} = 20$ V and $f = 10$ kHz

6.5.3 Sensor position

The positioning of the sensor is limited by the size of the available interlock samples and the size of the compression plates on the universal test machine Shimadzu AGX-V (Figure 6.16). Both sensors are positioned at 3 cm and 17 cm from the sample edge in contact with the inlet. To avoid edge effects, the sensors are positioned in the center of the plate, 2 cm from the lateral edges as seen on the top view schematic in Figure 6.11.

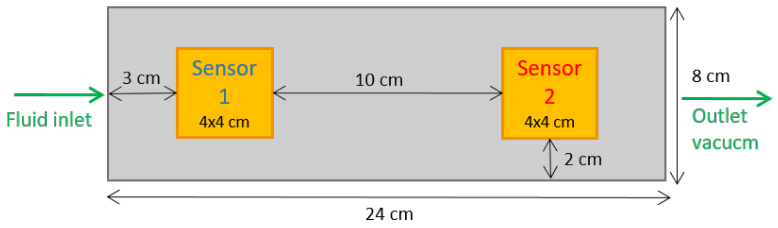

Figure 6.11: Schematic top view of dielectric sensor size and position on a preform.

6.5.4 Model fluid

As mentioned in Section 6.5.2 and in Table 6.1 particularly for carbon fabrics, it is important for the voltage variation ΔV of the system to be higher than the noise for good sensitivity. A fluid with a higher relative permittivity can increase ΔV so some available options were tested for the injection. Between the available fluids, Silicone oil has the lowest ε_r as seen in Table 6.2 and generated insufficient ΔV.

Pure glycerol has the highest ε_r, therefore both viscosity and permittivity can be adjusted with appropriate water/glycerol blends.

Fluid	Relative permittivity at ε_r at 25°C
Glycerol	42.5
Water	80.2
Silicon oil	11.7

Table 6.2: Tested fluids and their relative permittivity ε_r

For the chosen model fluid, 14 % in weight of water was added to pure glycerol. The dynamic viscosity of the blend is $\mu = 0.17$ Pa.s at 25°C.

6.5.5 Saturation measurement

As discussed in Sections 6.4 and 6.5, the operation of a dielectric sensor involves applying an AC voltage to the sensor, which is connected in series to a reference resistor R_{ref}. When the fluid enters the sensing volume, which is bounded by the copper plates of the sensor, the impedance of the sensing volume decreases. This change in impedance is directly proportional to the variation in fluid volume within the sensor and, consequently, indicates the level of saturation in that particular region. By measuring the change in impedance, the dielectric sensor can provide information about the degree of fluid saturation in the sensing volume.

The change in impedance of the sensing volume Z_{S1} can be calculated simply by measuring the tension $V1$ (Figure 6.10) across the known reference resistor R_{ref1} using Ohm's law [37]:

$$Z_{S1} = R_{\text{ref1}} \times \frac{(V_{in} - V_1)}{V_1} \tag{6.7}$$

Knowing the dry and fully saturated impedance Z_{dry} and Z_{sat}, the saturation S can then be calculated at any time t from the measured impedance of the impregnating sample Z using Equation 6.8 [72, 37]:

$$S = \frac{1/Z - 1/Z_{dry}}{1/Z_{sat} - 1/Z_{dry}} \tag{6.8}$$

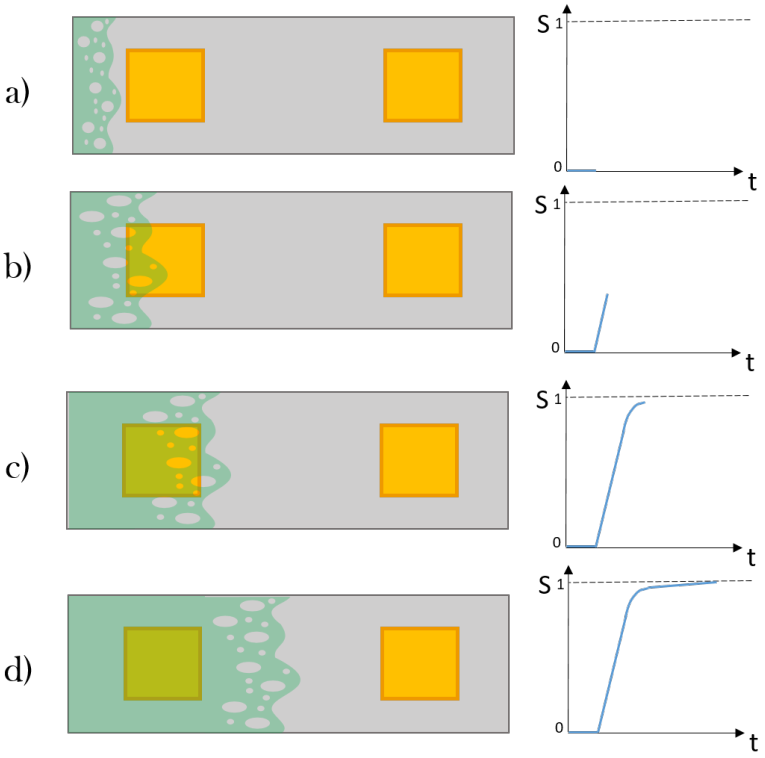

Figure 6.12: Schematic of saturation dielectric measurement over time during injection.

The evolution of saturation over time can be seen in Figure 6.12. Before the flow reaches the sensor, the sensing volume is dry and therefore the measured saturation is

0 (a). When the flow reaches the edge of the sensor, the impedance of the sensing area starts to change and the degree of saturation increases (b). After the unsaturated flow front surpasses the sensor (c) the majority of the meso voids are filled but the volume is not yet fully saturated. The full saturation occurs when the measurement of the sensing volume is at its highest stabilized, and therefore S = 1 (d).

6.5.6 Sensor visual validation

To validate the sensor, a glass interlock fabric Injectex was used to visually track the unsaturated flow front during the injection. A mixture of Glycerol + 17% water (by weight) was used as model fluid and a violet pigment was added to the mixture to increase the optical contrast. The injection was done using a vacuum bag and a camera was positioned over the injection table to capture the position of the unsaturated flow front. The areas of the copper sensors used were 2 × 2 cm.

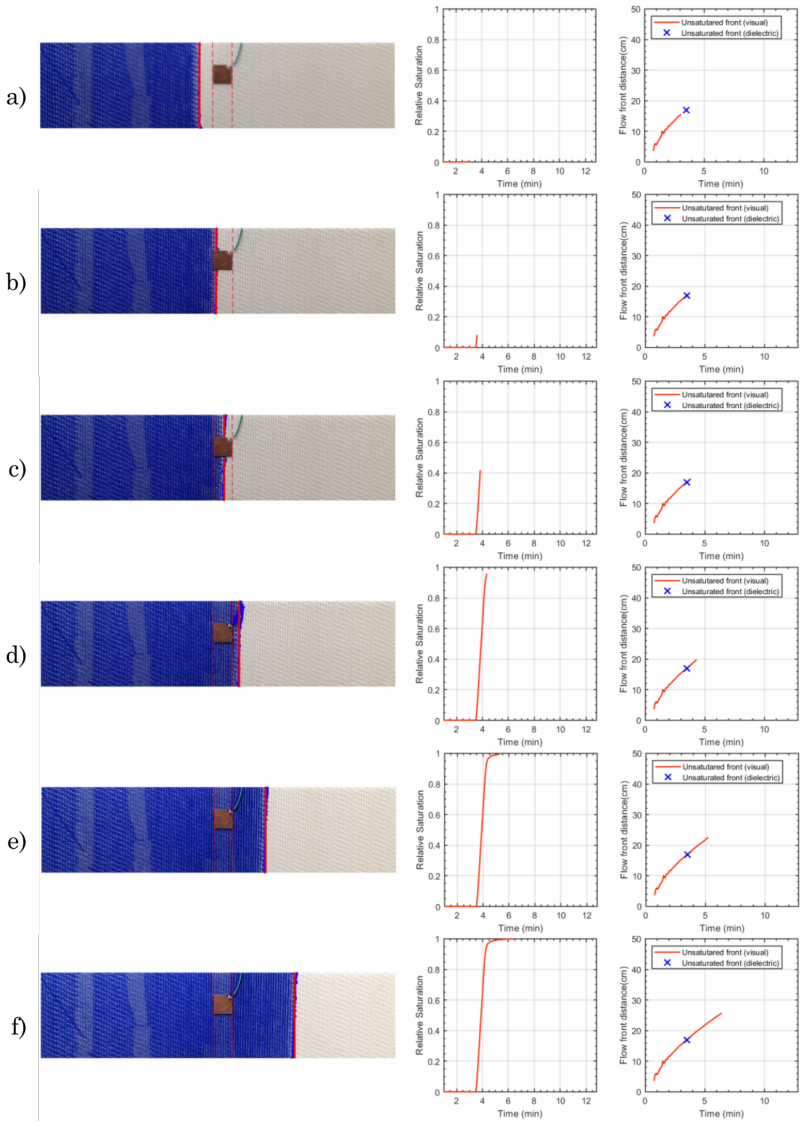

Figure 6.13: Validation of the dielectric sensor with glass Injectex 3D textile. As the fluid fills the preform (left from a) to f)), the sensor's saturation S evolves from 0 to 1 (center graph) and the flow front position measured optically (solid line) and dielectrically match (cross on the right graph).

Figure 6.13 shows images captured during the injection. On the right the saturation

measurement of the sensing area and the tracking of the unsaturated flow front are shown. Before the flow front reaches the sensor, the fabric is dry and the measured saturation is 0 (a). When the unsaturated flow front reaches the edge of the sensor the saturation starts increasing (b). The sensor is positioned at 17 cm from the edge of the sample and its time of arrival (blue cross) is in good agreement with the visually tracked flow front showing accurate response of the sensor (b). When the unsaturated flow front is halfway through the sensor, the measured saturation is around 40% (c) which shows that there is a delay between the saturated flow front and the visually tracked unsaturated flow front due to dual scale flow. The flow front then surpasses the sensor but the impregnation of the sensing region is not yet complete (d). The saturation is complete when the sensor reaches its maximum value and becomes stable (e) and (f).

Figure 6.14 compares the flow front position and relative saturation over time of the glass Injectex fabric. The graph shows good agreement between the arrival of the flow front at 17 cm and the start of the increase of measured saturation. The orange highlighted area represents the length of the sensor L_s of 2 cm. Both meso and micro pores are being filled simultaneously.

When the flow surpasses the sensor area, the fabric is around 80% saturated, eventually the saturation rate decreases as the majority of the meso-voids are filled and then the residual micro-pores are slowly filled until full saturation.

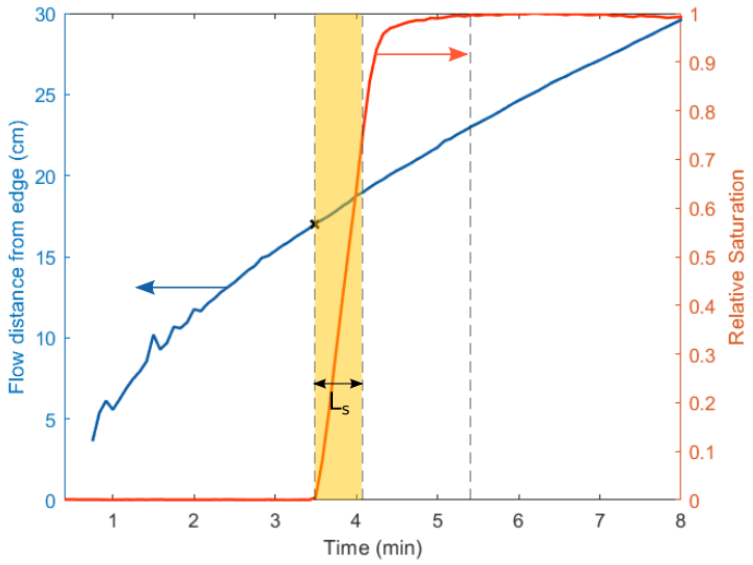

Figure 6.14: Saturation evolution and flow front position of the glass interlock Injectex during injection.

6.6 Experimental protocol

To measure the saturation evolution of the INCREASE06 fabric, three samples were injected at 50, 55 and 60 % fiber volume fraction. The unidirectional injection was done in both the warp and weft directions. In total 6 configurations were tested.

The fabric was inserted into a sealed bag that serves as a vaccum bag but also isolates the copper sensor from the conductive carbon fabric. The total measurement of the area includes the top and bottom isolating layers for all experiments as seen in Figure 6.15:

To achieve the desired fiber volume fraction the plates and the sample are positioned

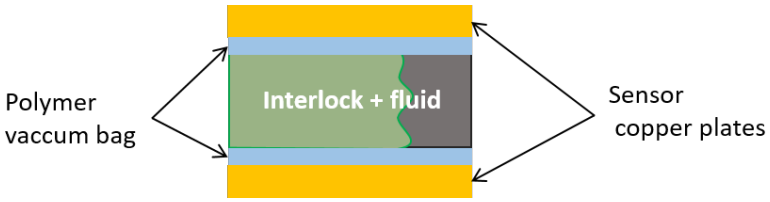

Figure 6.15: Electrical insulation for the sensors from the carbon preform using PA12 polymer vacuum bag.

and compressed in the universal testing machine Shimadzu AGX-V shown in Figure 6.16. The machine compresses the fabric to the desired fiber volume fraction then the glycerol/water blend is injected using a vaccum pump set at 0.8 bar absolute.

Figure 6.16: Universal testing machine Shimadzu AGX-V - *https://www.shimadzu.fr*

The injection is unidirectional. The interlock samples are rectangular (8 × 24 cm) and cut along the direction of warp and weft tows for the measurement of the saturation and permeabilities K_x and K_y respectively. Before the arrival of the fluid, the sensors measure the impedance of the dry fabric Z_{dry}. When the fluid arrives in the sensor area, the impedance of the sensing volume increases until its maximum value Z_{sat}. The change in impedance is proportional do the change in fluid volume in the sensing area and therefore to the degree of saturation in the area.

Each sample was compressed until a desired fiber volume fraction V_f then injected with the glycerol + water blend. The chosen mixture has 14% of water and a dynamic viscosity $\mu = 0.17$ Pa.s. The list of all performed tests can be seen in Table 6.3 (6 tests in total: 3 different V_f combined with 2 flow directions).

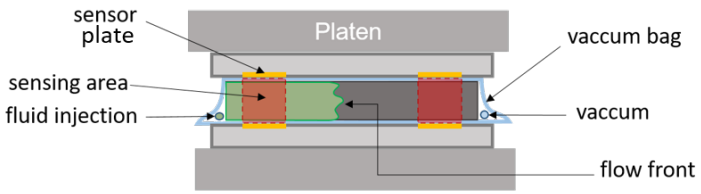

Figure 6.17: Schematic of the unidirectional injection mounted in the universal testing machine.

Direction	V_f(%)	h (mm)	Fluid viscosity μ (Pa.s)	P absolute (bar)	$\Delta P_{inj.}$ (bar)
Warp	50	12.5	0.17	0.8	0.2
	55	11.4			
	62	10			
Weft	50	12.5	0.17	0.8	0.2
	55	11.4			
	62	10			

Table 6.3: List of performed tests and test parameters.

6.7 Results

6.7.1 Post processing of results

The absolute voltages measured with sensor 1 (blue line) and sensor 2 (red line) for the injection in the weft direction at $V_f = 62\%$ can be seen in Figure 6.18. The difference in ΔV between both sensors comes from the fact that both sensor and measurement electronic chain are not exactly the same.

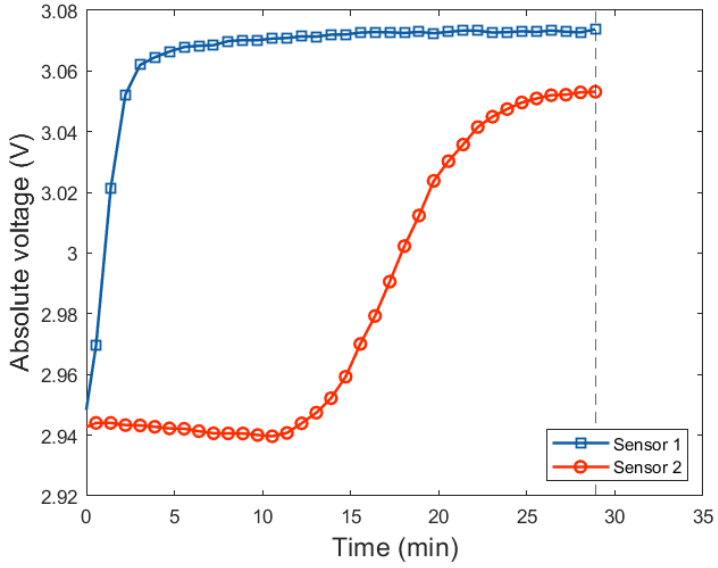

Figure 6.18: Absolute voltages measured by both sensors during an injection in the weft direction and $V_f = 62\%$

Small geometrical differences impact on the sensor response such as the copper plate area or the distance as given in Equation 6.3. In the experimental bench, the sensor 2 always produced a smaller ΔV than sensor 1 even when the injection gate was positioned to

the opposite side, confirming that it is a characteristic of the sensor and the measurement electronic chain and not of the fabric.

Figure 6.19 shows that for all tests configurations, the sensitivity of the sensors is always greater than 0.1 V and much larger than the noise, therefore the set up (electrical circuit, imposed generator, fluid and preform) allow to realize measures of impregnation with confidence.

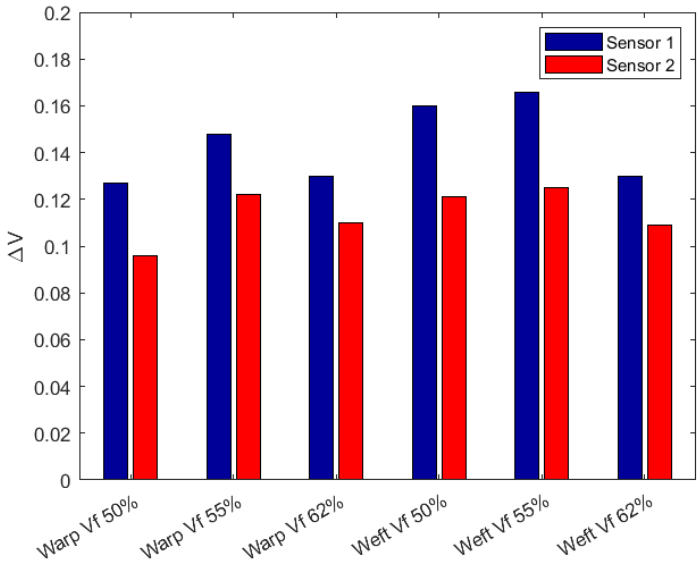

Figure 6.19: Voltage variation ΔV of sensor 1 and 2 during unidirectional injections for the 6 tested configurations.

The values are normalized when the voltage is transformed into saturation using Equation 6.8. The Figure 6.20 shows the evolution of the saturation during the injection of the fabric injected at $V_f = 62\%$ in the weft direction. One can see that the sensor 1 response is steeper than sensor 2 because of the injection at constant inlet pressure. The macro impregnation speed is larger and reaches saturation values of 0.8 faster, however, the final saturation from 0.8 to 1 takes more time at the position 1 (close to the inlet) than position 2 (close to the outlet).

6.7.2 Saturation over time

The saturation evolves over time for all test configurations presented in Table 6.3. Measurements are collected in Figures 6.21 and 6.22 for the samples injected in the warp and weft directions respectively.

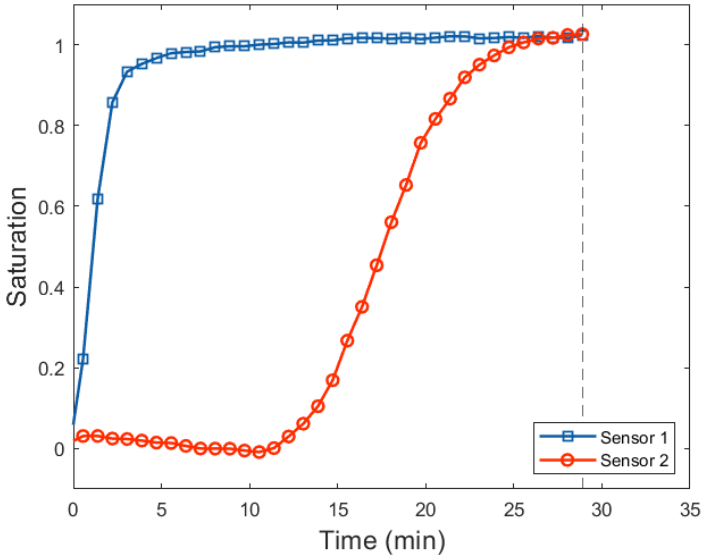

Figure 6.20: Saturation evolution over time of injection in the weft and warp directions of INCREASE06 with $V_f = 62\%$

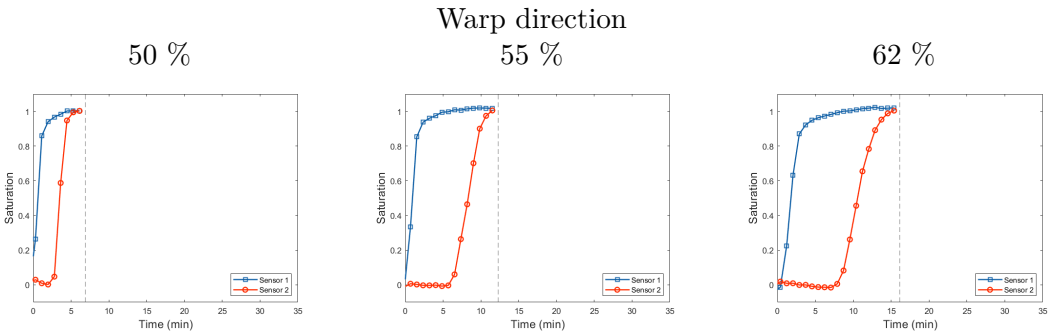

Figure 6.21: Saturation evolution over time of INCREASE06 samples compressed to $V_f = 50, 55$ and 62% and injected in the warp direction.

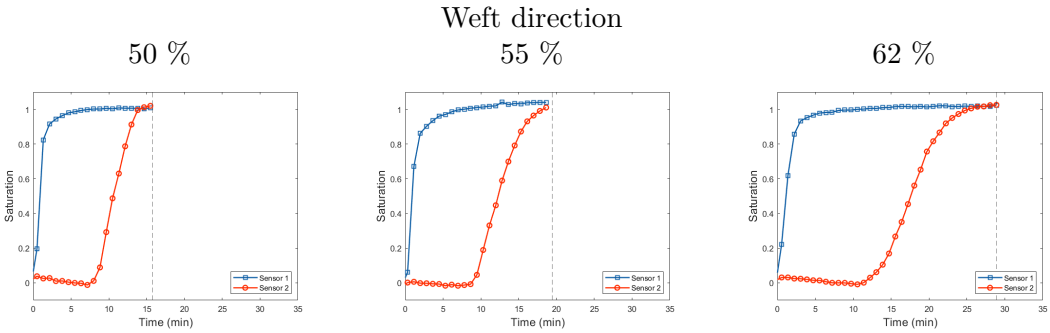

Figure 6.22: Saturation evolution over time of INCREASE06 samples compressed to $V_f = 50, 55$ and 62% and injected in the weft direction.

Comparing the tests realized at low and high V_f show that the preforms saturate faster at low V_f as expected. When the V_f increases the saturation time is doubled from 7.5 to 15 min (warp direction) and from 15 to 30 min (weft direction).

The observations made in both directions show that the saturation occurs faster in

the warp direction which is in agreement with the macroscopic permeability measurements presented in Chapter 4.

6.7.3 Sensor position comparison

During an experimental impregnation process, the saturation level $S(t)$ is determined from the recorded voltage at the location of the sensor (Equation 6.8). To obtain spatial information $S(x)$ and identify the unsaturated length, it is necessary to convert the measured saturation profiles in time $S(t)$ to corresponding spatial profiles $S(x)$.

Under the assumption of a small saturation evolution profile in space as time progresses, the saturation signal can be transformed as expressed in Labat [34] and Guéroult [23]. For the derivations below, the following nomenclature is used:

Variable	**Description**
x	1D axis of the space domain; $x = 0$ corresponds to the beginning of the preform
X_f	flow front position in the space domain
X	sensor position; therefore a fixed value in the space domain
t	time; $t = 0$ corresponds to the beginning of injection
T_0	time at which flow front reaches the sensor's location X,therefore a fixed value in the time domain
T	arbitrary reference time, i.e time at which the data will be plotted
ΔX	distance from the sensor position X
ΔT	time delay from the time of interest T corresponding to the distance ΔX
$D = \frac{K}{\phi\mu}\Delta P$	constant ratio of materials properties
u_D	Darcy's velocity

With the above nomenclature, Darcy's law writes in 1D along the $x-$ axis:

$$u_D(t) = -\frac{K}{\phi\mu}\nabla P = \frac{K}{\phi\mu}\frac{\Delta P}{X_f(t)} = \frac{D}{X_f(t)} \tag{6.9}$$

using $u_D(t) = \frac{dX_f(t)}{dt}$, after integration of Equation 6.9 we obtain:

$$X_f(t) = \sqrt{2D}\sqrt{t} \tag{6.10}$$

Using Equation 6.10, we can rewrite Equation 6.9:

$$u_D(t) = \sqrt{\frac{D}{2}}\frac{1}{\sqrt{t}} \tag{6.11}$$

For a given time delay ΔT related to the time of interest T, the corresponding distance ΔX to the sensor's location can be expressed, by definition of velocity:

$$\Delta X = \int_T^{T+\Delta T} u_D(t)dt = \int_T^{T+\Delta T} \sqrt{\frac{D}{2}}\frac{1}{\sqrt{t}}dt \tag{6.12}$$

which leads after integration to:

$$\Delta X = \sqrt{2D}[\sqrt{T+\Delta T} - \sqrt{T}] \tag{6.13}$$

Considering that at time $t = T_0$, the flow front reaches the sensor's position X, Equation 6.10 leads to:

$$X = \sqrt{2D}\sqrt{T_0} \tag{6.14}$$

and Equation 6.13 becomes:

$$\Delta X = \frac{X}{\sqrt{T_0}}(\sqrt{T + \Delta T} - \sqrt{T}) \tag{6.15}$$

Then the spatial saturation profile is transformed at various $x = X - \Delta X$ from the time saturation profile using $S(x) = S(t)$ with $t = T + \Delta T$

The algorithm describing the steps for the time to space transformation can be seen below:

Algorithm 1 Transformation of the saturation evolution from time domain to spatial domain

Calculate $S(t)$ using Equation 6.8
Identify the time of the flow front arrival into the edge of the sensor $t = T_0$
Choose the time delay $\Delta T = \{T_{min}, ..., T_{max}\}$
Calculate corresponding $\Delta X = \{X_{min}, ..., X_{max}\}$ using Equation 6.15
Calculate $x = X - \Delta X$
Interpolate $S(t)$ using $t = T + \Delta T$
Plot transformed $S(x)$

This method can now be applied to the different experimental saturated over time curves that were presented and get the spatial saturation profile at an instant T as seen in Figure 6.23:

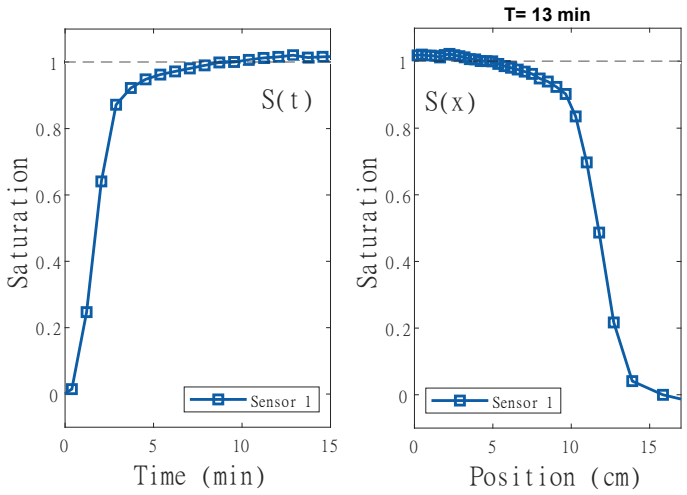

Figure 6.23: Transformation from time domain $S(t)$ (left) to spatial domain $S(x)$ (right) of the injection in the weft direction at $V_f = 62\%$ plotted at a chosen time $T = 13$ min.

6.7.3.1 Unsaturated length Δx

The unsaturated length is the distance between the unsaturated and saturated flow front as illustrated in Figure 6.24. A smaller unsaturated length correspond to a reduced void content since the impregnation speed intra and inter-tow are closer.

The influence of fabric geometry in the unsaturated length was previously studied by Pedarròs [69] by comparing UD, UDM and TW fabrics. Due to the complexity of the interlock's geometry, a direct correlation between its geometry and the unsaturated length is difficult to make, however differences are expected between the injection made in the weft and warp directions.

The unsaturated length is also expected to be smaller when the tests are conducted at a higher V_f. The larger the ratio between the average bulk permeability of the fabric K_{bulk} and the tow permeability K_{tow}, the more pronounced is the fabric's dual-scale porosity contrast, on the contrary, as K_{bulk} gets closer to K_{tow} during compression, the fabric has a smaller unsaturated length and gets closer to a single-scale behavior.

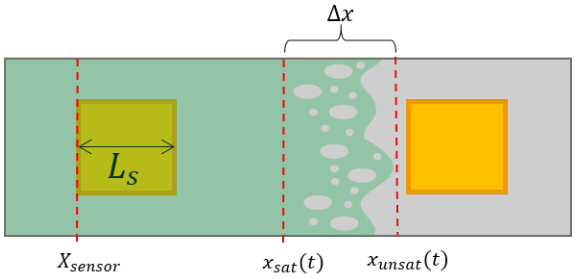

Figure 6.24: Unsaturated length Δx measured during injection at a time t.

Two particular moments during injection are used to calculate the unsaturated length experimentally: when the unsaturated flow front first reaches the sensor at a known time T_0 and the time when saturation first reaches 1. This happens when the saturated flow front leaves the sensor at position X_{sensor} added the length of the sensor L_s as seen in Figure 6.25.

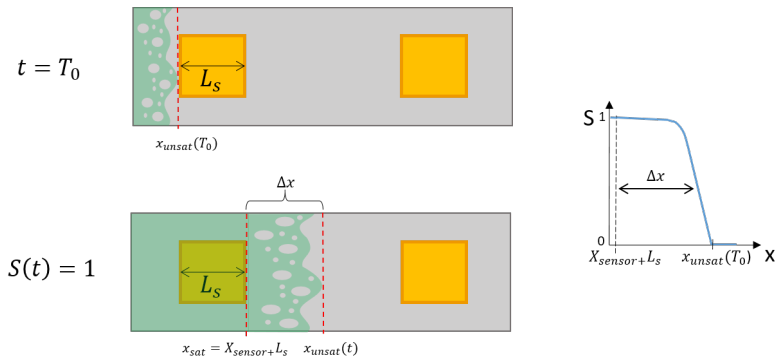

Figure 6.25: Unsaturated length Δx measured during injection at a time t.

Knowing those two points the unsaturated length Δx can be calculated as follows:

$$\Delta x = x_{unsat}(t) - x_{sat}(t) \tag{6.16}$$

6.7.3.2 Sensor position comparison

The impregnation speed decreases over time during a injection with constant pressure P. The flow speed influences how much capillarity will be representative in the filling: at a higher impregnation speed, the flow is driven by viscous forces and preferably fills the meso voids first then the micro voids. On the contrary, at low speed, the capillary forces drive the flow into the tow, filling the micro voids.

The unsaturated length is expected to vary between Sensor 1 (positioned closer to inlet) and Sensor 2 since the local impregnation speed is different.

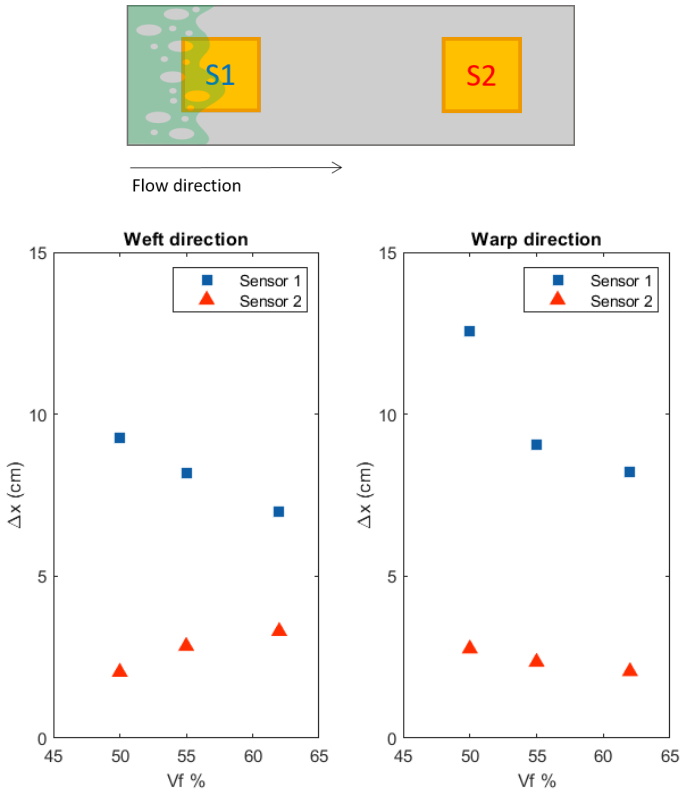

Figure 6.26: Unsaturated length Δx comparison between sensor 1 and 2 during injection in weft (left) and warp (right) directions.

Figure 6.26 shows the unsaturated length Δx measured from the injection tests described in Table 6.3.

Firstly, it can be observed that this particular interlock fabric has a highly-contrasted dual-scale porosity. The unsaturated length measured is on the order of centimeters while other traditional unidirectional carbon fabrics were shown to have unsaturated lengths in the order of millimeters [69]. The dense and twisted tows that are difficult to impregnated combined to large meso-spaces in between tows creates a much longer region with transient void content (large Δx).

When comparing the unsaturated length at different positions (S1 positioned at 3 cm and S2 at 17 cm from the edge of the sample) it is clear that the Δx is larger on the S1 area. Having a higher impregnation speed, the S1 region fills the channels faster in comparison to the Sensor 2 region that impregnates channels and tows in a slower rate as seen in Figure 6.27.

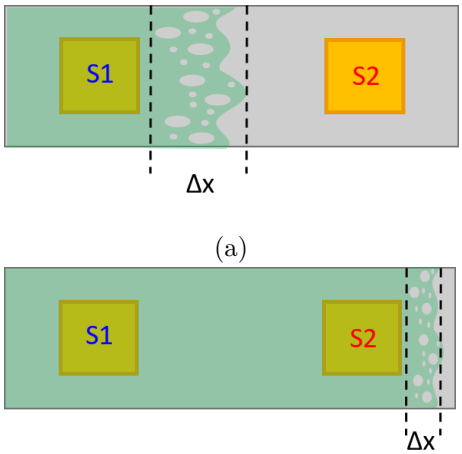

Figure 6.27: Schematic of the unsaturated length Δx in the beginning (a) and end (b) of the injection at constant pressure P

Average permeability comparison

The tests were performed at different fiber volume fractions of 50, 55 and 62% as seen in Table 6.3. With the increase in V_f the average bulk permeability of the fabric K_{bulk} decreases and get closer to the permeability of the tow K_{tow} that supposedly does not increase significantly with compression as the main mechanism that occurs during the compaction is more the displacement of the tow than the deformation of the tows.

The unsaturated length Δx decreases with the augmentation of V_f (Figure 6.26) since K_{bulk} gets closer to K_{tow} and the dual-scale porosity contrast of the fabric decreases.

The decrease in Δx is clearly observed in sensor 1, whereas sensor 2 remains relatively constant at around 4 cm. This behavior can potentially be attributed to the limited sensitivity of sensor 2 in measuring the sensing area due to a low impregnation speed. Another challenge encountered with sensor 2 is the 3 cm distance between the edge of the sensor and the end of the sample may not provide sufficient length for the complete saturation of the sensing area before the flow front reaches the end of the sample.

If the sample size was not constrained by the size of the compression platens of the universal testing machine, it would be advisable to use a longer sample for the measurement of this specific fabric that has a large unsaturated length. This would allow for better assessment and saturation of the sensing area, potentially resolving the issues observed with sensor 2.

6.7.3.3 Different flow direction

The injections were made in warp and weft directions. The weft and warp tows have different lineal weights (Table 3.1) and also the complex 3D weaved pattern changes with the rotation of the geometry.

Pedarròs [69] analyzed the influence of the topology of the porous medium on its unsaturated length. It was shown that in a more unidirectional fabric (fiber aligned to the flow direction) fewer voids are created because the transverse tows act as obstacles.

Figure 6.28 compares the unsaturated length of the tests injected in the weft and warp directions. As shown in Chapter 4 the permeability in the warp direction is higher than in

the weft direction and with this information alone the unsaturated length measured during the injection in the warp direction is expected to be larger due to the faster impregnation speed in this direction.

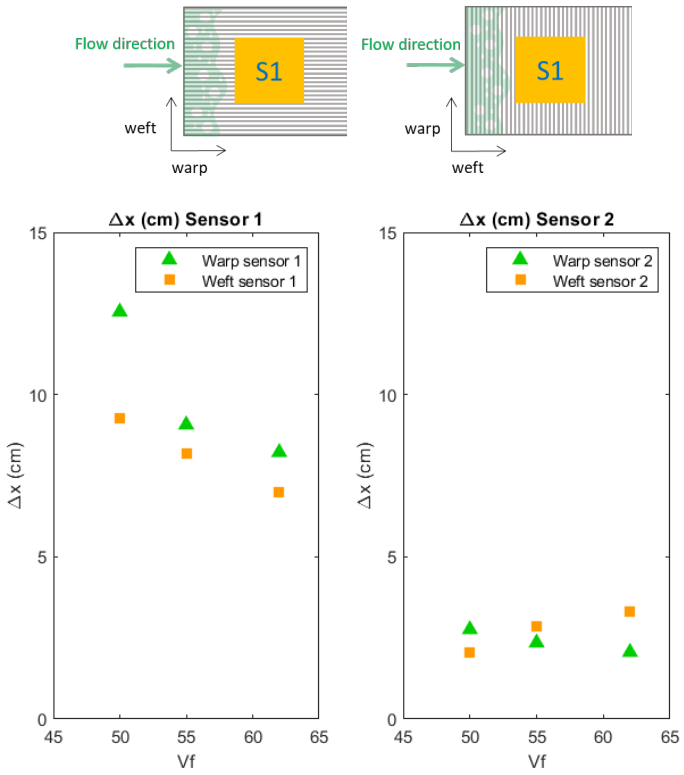

Figure 6.28: Comparison between weft and warp unsaturated length Δx of sensor 1 (left) and sensor 2 (right).

The INCREASE06 fabric has different sized tows, the warp (48k filaments) and weft (24k filaments). The unsaturated length Δx is analyzed at a macroscale by comparing the bulk permeability of in the warp K_x and weft K_y directions as previously mentioned.

In a meso-scale analysis however, the Δx results show that the average unsaturated length Δx of the sensing area is longer when the flow is perpendicular to the weft tows and parallel to the warp (Figure 6.29 (b)). Considering both the size of the tows and the difference in parallel and transverse permeability proposed by Gerbart [21] ($K_{tow\perp} < K_{tow\parallel}$) those results are contrary to what it would be expected.

It's important to note that the geometry is quite complex and the individual influence that the weft and warp tows have on the flow is not explicit. This behavior may be due to the twisting of the tows which makes the parallel impregnation of the warp (larger tow) difficult and also to the effect that the transverse yarns have on the flow.

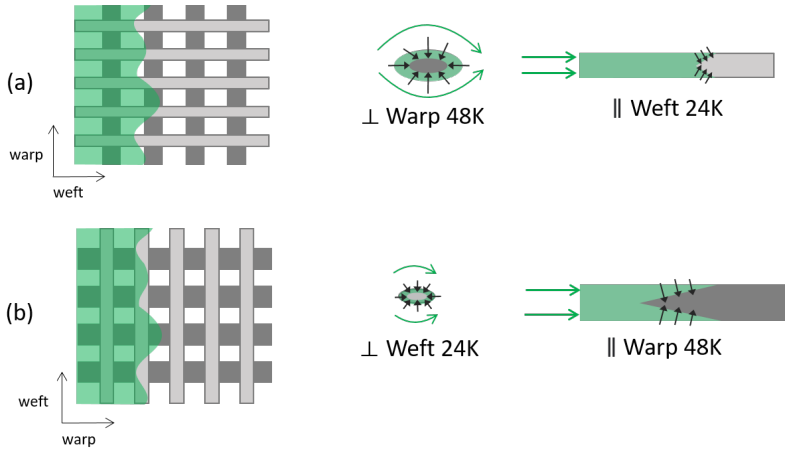

Figure 6.29: Flow behavior during injection in the warp (a) and weft (b) directions.

The saturation analysis at the tow scale cannot be done with this proposed experiment, as the measured saturation is an average value of the sensing region and should be complemented with a numerical model.

A complementary preliminary numerical study is presented in Section 6.8. A simplified geometry with representative tow size and tow spacing is analyzed in order to better understand the influence of different sized tows on the impregnation .

6.7.3.4 Partial conclusion

The unsaturated length Δx is the difference between the unsaturated and saturated flow front. The impregnation speed and pore geometry were shown to influence the size of Δx. It is preferable to adjust the manufacturing conditions in order to have a smaller unsaturated length and less void content. From the experimental results, it was concluded that for the INCREASE06 interlock:

- A lower impregnation speed creates a smaller Δx
- A smaller average permeability K_{bulk} decreases the dual-scale porosity contrast of the fabric and therefore produces a smaller Δx (at higher V_f)
- The injection of the flow parallel to the weft direction creates a smaller Δx for this particular fabric.

Regarding the sensor set up, the sample must be longer in order to finish impregnation in the sensing area 2. Therefore only the results from the first sensor will be analyzed going forward.

6.7.4 Time to fill

It is important to make sure that the composite part is well impregnated at the end of the manufacturing process. During the production of the composites plates using C-RTM, it was observed that at the end of injection (when the flow front arrived to the vents) the tows were not yet fully impregnated. A bleeding process was added, where the mold is kept closed after the flow front arrival at the vents while maintaining a high pressure to increase the filling of the micro-voids. After around 30 minutes, the part was then removed with a better impregnation in comparison to a part with zero bleeding.

The dielectric sensor can measure the time to fully impregnate the sensing volume and it can be used to optimize the bleeding during the process in real time. The T_{fill} is

the time to fully saturate the sensing volume and it is the difference between the time of full saturation $t_{saturation}$ and the time of flow front arrival $t_{arrival}$ as shown in Figure 6.30:

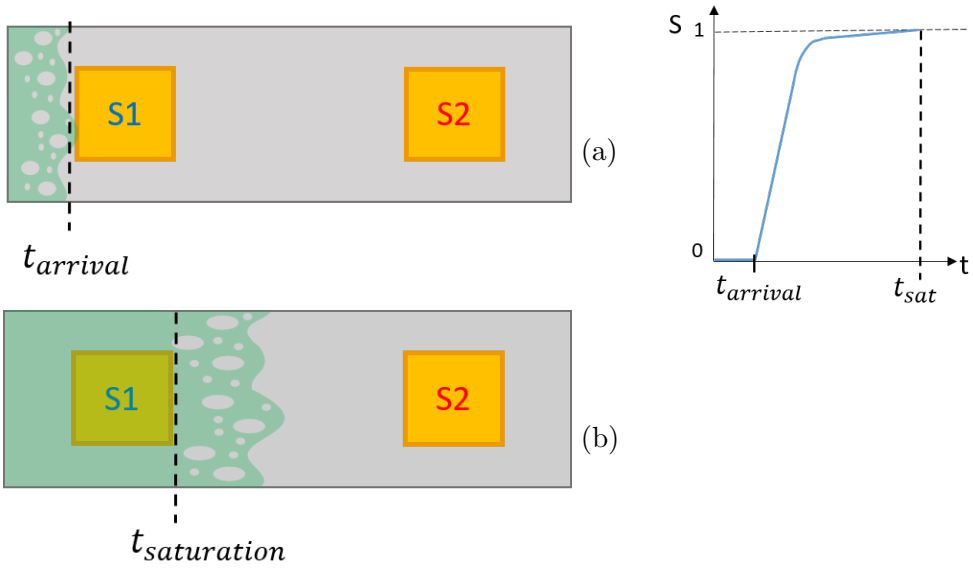

Figure 6.30: Time of flow front arrival $t_{arrival}$ (a) and time of full saturation $t_{saturation}$ of the sensing area (b)

In Figure 6.31, the measured filling time (T_{fill}) in minutes is depicted for sensor 1, alongside the theoretical filling time of a single-scale fabric without any unsaturated length calculated with the permeability measured during the dielectric tests. The difference between these two values highlights the influence of voids transportation in the impregnation time of a fabric. As mentioned, the difference between the expected and real filling time was observed in-site during the manufacturing of plates and the bleeding time was added to the process.

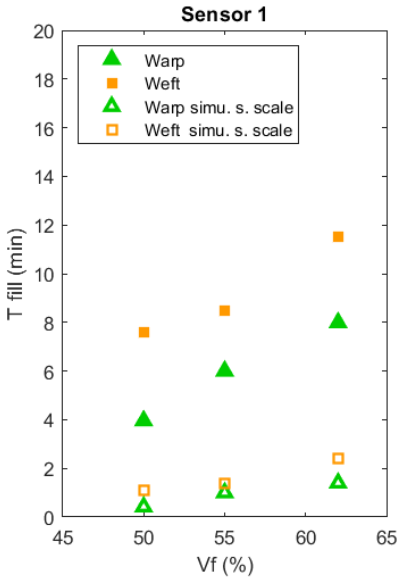

Figure 6.31: Comparison between the time for full impregnation T_{fill} measured with the dielectric sensor and a theoretical single scale T_{fill} .

The total filling time of a fabric with a highly contrasted dual-scale porosity such as the INCREASE06 interlock is 6 times higher in comparison to a theoretical single scale fabric with the same macroscopic bulk permeability. It it very important to consider not only the permeability of the fabric but also the influence of ratio between the bulk and tow permeability when simulating the process and choosing the manufacture parameters.

6.7.4.1 Partial conclusion

The filling time T_{fill} is the time to fully saturate the sensing volume. The filling time increases at lower macroscopic (bulk) permeability because the meso-voids are smaller due to compression. The impregnation also takes longer for the tests injected in the weft direction in comparison to the ones on the warp direction, which is coherent with the fabric's anisotropy and $K_{warp} > K_{weft}$.
The macroscopic permeability must not be the only considered when modeling the manufacturing process. For fabrics with an high dual-scale porosity contrast, the filling time is much higher in comparison to a single scale fabric and this difference must be taken into consideration when choosing the process parameters.

6.7.5 Permeability

The permeability in the warp direction (K_x) and weft direction (K_y) was determined by calculating the time of flow arrival at different positions: the edge of sensor 1 ($x = 3$ cm), sensor 2 ($x = 17$ cm), and the edge of the sample ($x = 24$ cm). Figure 6.32 illustrates that the permeability values obtained using the dielectric sensor are higher compared to those obtained through the radial injection method.

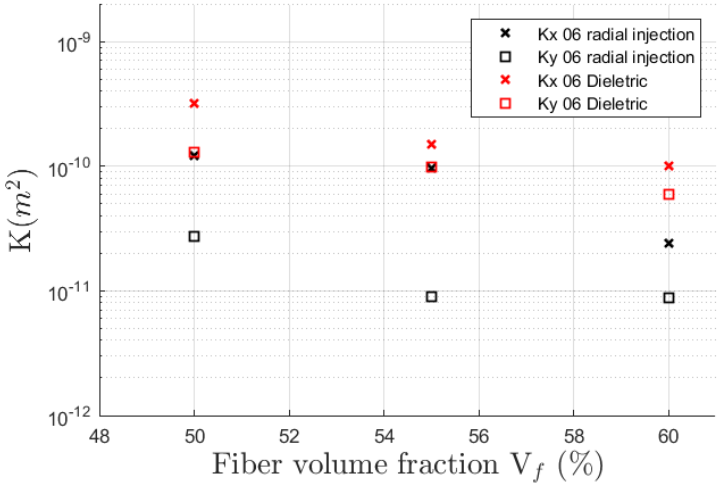

Figure 6.32: Comparison of macroscopic permeability measured with dielectric sensors and radial injection as seen in Chapter 2.

The injection for the dielectric measurements were performed only once the fabric was fully relaxed after the compression and the force cell was stable. During the relaxation period the fibers are reorganized which did not happen as much during the radial injection. This difference in fiber arrangement could explain the variation observed between the two measurement techniques.

Additionally, there was a difference in the inlet pressure between the radial injection test and the saturation tests conducted with the dielectric sensor. The radial injection test had an inlet pressure above atmospheric pressure, while the dielectric tests were performed under a partial vacuum (below atmospheric pressure). This discrepancy in inlet pressure results in different impregnation speeds and more or less pronounced dual scale saturation as previously discussed in Section 6.7.3.2.

6.8 Preliminary numerical analysis

As previously mentioned the experimental analysis is limited to the macro scale since the values measured are averaged over the sensing region. To have a better understanding of the impregnation phenomena at the meso-scale (tows and channels), a numerical analysis of a simplified geometry with representative tow and tow-spacing dimensions was used.

The results presented in Section 6.7.3.3 showed that the unsaturated length was higher (larger unsaturated region) when the flow was parallel to the warp (larger) tows and perpendicular to the weft (smaller). These results have raised questions since having the flow perpendicular to a larger and denser tow is expected to create a longer unsaturated region. For this reason, a preliminary analysis of the influence of unbalanced tow size is presented

The simulations of the unidirectional injection of a dual scale fabric are implemented here using the software OpenFOAM.

OpenFOAM is a collection of tools developed independently by the OpenFOAM foundation and the OpenCFD company [79]. It was born as a project for solving field operations, based on libraries written in C++. It uses the Finite Volumes Method (FVM, [29]) for solving equations, which is a method that discretizes the space in small volumes, as opposed to the Finite Elements Method (FEM) which is based on elements. This means that the equations are solved inside of a volume instead of at nodes, which is useful in fluid dynamics since it simplifies the computation of flows and transport.

OpenFOAM is not a solver in itself, but rather a collection of solvers (a library) for different purposes. One of the solvers provided, called interFoam, is used for simulating dual-phase flows in a given domain. This solver, initially used for incompressible fluids, was adapted to allow compressibility to simulate the presence of air during the injection process. The results showed in the following have been run in a code under development at GeM.

6.8.1 Meso-scale description

The simulation of the fabric is done at the meso-scale level. The domain is discretized in hexahedra, where the equations are solved. For modeling in the meso-scale, a Darcy-Brinkman model is used to simulate the two-phase flow. In here, a single set of equations can be used to represent the flow in a solid free region (gaps between fiber tows) and simultaneously inside the porous matrices (fiber tows) [13].

The two-phase micro-continuum approach relies on single-field variables, i.e., unique fluid pressure and velocity fields that are defined throughout the entire grid regardless of the nature of the phases that occupy the cells. The single-field pressure $\bar{p}$ and velocity $\bar{\boldsymbol{v}}$ are defined as weighted sums of the pressure and Darcy velocity in each fluid phase:

$$\bar{p} = \alpha_l \bar{p}_l + \alpha_g \bar{p}_g \tag{6.17}$$

$$\bar{\boldsymbol{v}} = \phi(\alpha_l \bar{v}_l + \alpha_g \bar{v}_g) \tag{6.18}$$

where ϕ corresponds to the porosity of the material, α is the volume fraction and l,g identify the liquid and gas phases respectively.

The simulation is performed by solving the following set of equations:

$$\frac{\partial \phi \alpha_i}{\partial t} + \nabla \cdot \bar{\boldsymbol{v}}_i = 0 \quad i = l,g \tag{6.19}$$

$$\frac{1}{\phi}\left(\frac{\partial \rho \bar{\boldsymbol{v}}}{\partial t} + \nabla \cdot \left(\frac{\rho}{\phi}\bar{\boldsymbol{v}}\bar{\boldsymbol{v}}\right)\right) = -\nabla(\phi \alpha_i \bar{p_i}) + \phi \alpha_i \rho_i \boldsymbol{g} + \nabla \cdot (\phi \alpha_i \bar{S_i}) + \boldsymbol{D}_{is} + \boldsymbol{D}_{ij} \quad i = l,g \tag{6.20}$$

where $\boldsymbol{D}_{is}$ represents the interaction between fluid i and surface s and $\boldsymbol{D}_{ij}$ between fluid i and j.

In here, Equation 6.19 is the continuity condition of each phase. The saturation equation is derived from here by summing the continuity in both phases. Since we are considering a non-moving porous network, we can write the total velocity as:

$$\nabla \cdot \bar{\boldsymbol{v}} = 0, \tag{6.21}$$

which combined with both Equations in 6.19 gives

$$\frac{\partial \phi \alpha_l}{\partial t} + \nabla \cdot (\alpha_l \bar{\boldsymbol{v}}) + \nabla \cdot (\phi \alpha_g \alpha_l \bar{\boldsymbol{v}_r}) = 0 \tag{6.22}$$

where $\boldsymbol{v}_r = (\boldsymbol{v}_l - \boldsymbol{v}_g)$ is the relative pore-scale velocity between both phases. This equation represents the saturation of the wetting phase l being advected by the velocity of the domain, with an extra convection term coming from the relative velocity.

For Equation 6.20, the matrices $\boldsymbol{D}_{ik}$ represent the drag forces exerted by the solid phase ($k = s$) or interfacial shear between the two fluids ($k = j$) in the respective phase i, while $S = \mu(\nabla \bar{\boldsymbol{v}} + \nabla \bar{\boldsymbol{v}}^T)$ is the shear stress tensor and $\boldsymbol{g}$ the gravity. For the pressure equation, the same approach is taken of summing both phases and replacing the drag forces for a generalized expression, which leads to

$$\frac{1}{\phi}\left(\frac{\partial \rho \bar{\boldsymbol{v}}}{\partial t} + \nabla \cdot \left(\frac{\rho}{\phi}\bar{\boldsymbol{v}}\bar{\boldsymbol{v}}\right)\right) = -\nabla \bar{p} + \rho \boldsymbol{g} + \nabla \cdot \bar{S} - \mu \mathbf{K}^{-1} \bar{\boldsymbol{v}} + \boldsymbol{F}_c \tag{6.23}$$

where μ is the single field viscosity ($\mu = \alpha_l \mu_l + \alpha_g \mu_g$), $\mathbf{K}$ is the permeability and $\boldsymbol{F}_c$ represents the surface tension.

The procedure used by the solver for the previous coupled equations is sequential in nature, meaning that it handles one field and uses the results to obtain the next one. The simulation keeps going timewise until some criterion is reached or until the sample is completely saturated.

6.8.2 Representative geometry and boundary conditions

The representative fabric used in this study consists of a simple twill with an unbalanced tow size such as the one from INCREASE06 described in Table 3.1. The warp tows of INCREASE06 have 24k filaments while the weft tows have 12k. The height and width of the weft tows were reduced by a factor of $\sqrt{2}$ to represent the volume differences as

illustrated in Figure 6.33. The tow spacing in the simulation accurately reflects the real geometry.

This geometry will give a qualitative insight into the the effect of an unbalanced fabric on saturation. This simulation is a first step towards the representation of the impregnation of the INCREASE06 geometry. The solver is currently under development and a simplified geometry will provide an insight into the this peculiarity (unbalances tows) of the fabric, while also providing a stepping stone into the simulation of the real INCREASE06 geometry when the more accurate geometric model is available.

The unit cell is scaled up in terms of intertow gap size and fiber tow permeability to facilitate the interpretation of flow fields. Boundary conditions are defined accordingly to allow convergence of the numerical model under laminar flow condition.

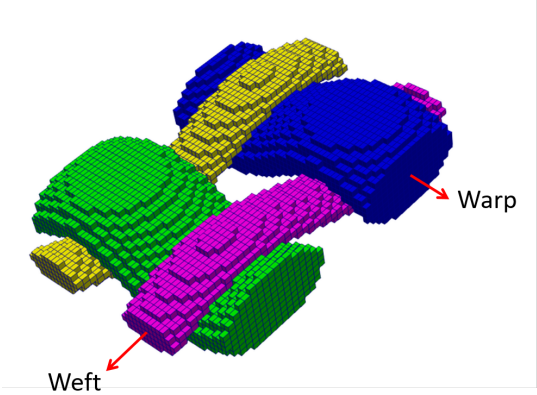

Figure 6.33: Representative unbalanced fabric model used for the meso-scale simulation - made with TexGen.

The input parameters of the simulation can be seen in Table 6.4. The tow permeabilities parallel $K_{tow\parallel}$ and perpendicular $K_{tow\perp}$ in relation to the flow were calculated using Gebart's model [21].

Input parameter	Value
$K_{tow\parallel}$	1.5×10^{-8} m^2
$K_{tow\perp}$	3.2×10^{-9} m^2
V_{ftow}	50 %
μ_{fluid}	0.17 Pa.s
μ_{air}	1.9×10^{-5} Pa.s
ΔP	0.01 bar

Table 6.4: Input parameters for flow simulation

μ_{fluid} is the fluid viscosity measured during the experiments, V_{ftow} is the fiber volume fraction of the tow, and ΔP is the pressure difference between inlet and outlet of the domain. The initial boundary conditions are set at the inlet are pressure $P_{inlet} = 1.01$ bar and the saturation $\alpha_l = 1$. Everywhere else inside the domain and outlet has pressure $P_{outlet} = 1$ bar and the lateral walls have a zero gradient boundary condition as seen in Figure 6.34:

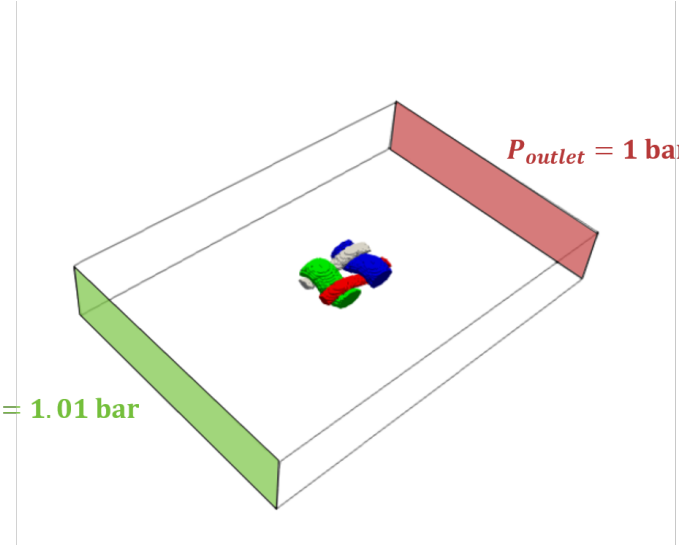

Figure 6.34: Applied inlet and outlet boundary conditions on the domain.

The simulation of the flow is done in the full domain of $40 \times 60 \times 9.09$ mm (Figure 6.35 (a)) but in order to avoid boundary effects and also better represent what is measured with a parallel plate dielectric sensor, the saturation over time curves are done by averaging α_l within a center cell of $8 \times 12 \times 3.03$ mm as depicted in Figure 6.35 (b):

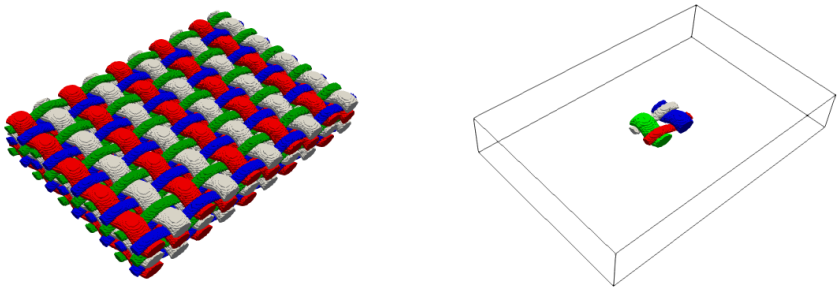

(a) Full domain of $5 \times 5 \times 3$ cells (b) Center cell

Figure 6.35: Domain for injection simulation (a) and cell in which the saturation evolutions is captured (b).

6.8.3 Results

Figure 6.36 shows the impregnation of the fabric in the weft direction. The fabric starts with saturation close to 0 (blue) until the arrival of the flow. The saturation occurs in the direction of the flow, being completely saturated close to the inlet. The lesser saturated areas ($0 < S < 1$) represent the saturation delay and air transport within the tows in the channels. This 5s detailed simulation of the flow took 1920 core hours (96 cores).

To better visualize the exchange of fluid between tows and channels and the saturation of the tows, the computational domain has been split in two. Figure 6.37 (a) illustrates the filling of the channels and Figure 6.37 (b) the filling of the tows of a injection in the weft direction.

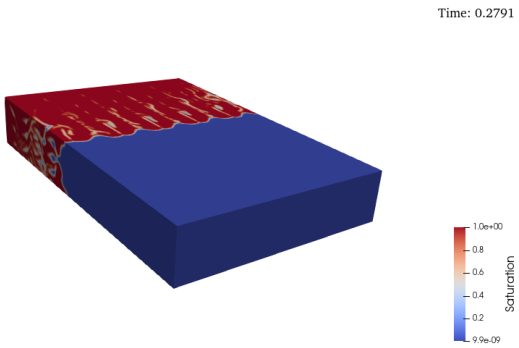

(a)

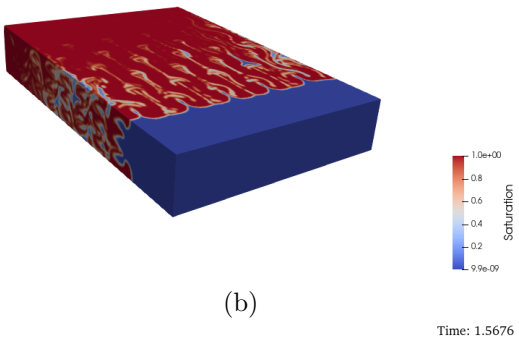

(b)

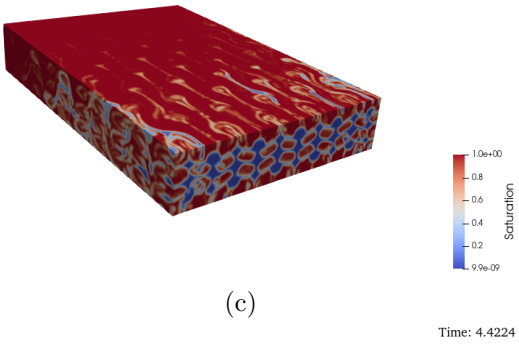

(c)

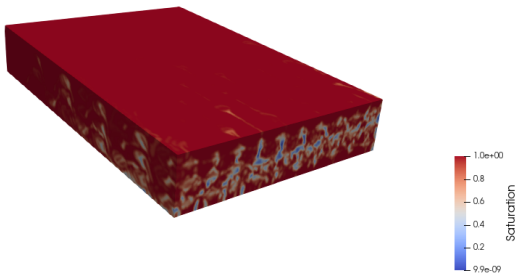

(d)

Figure 6.36: Saturation evolution (α_l) over time of a flow in the direction of the weft tows.

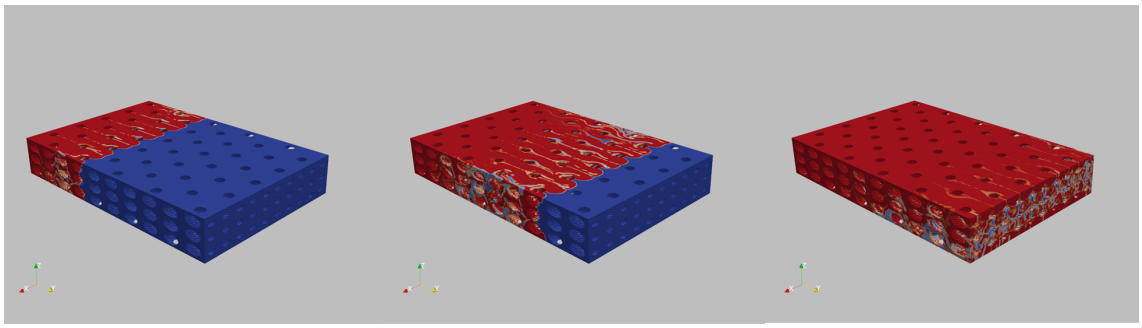

(a) Saturation of the channels at increasing time from left to right.

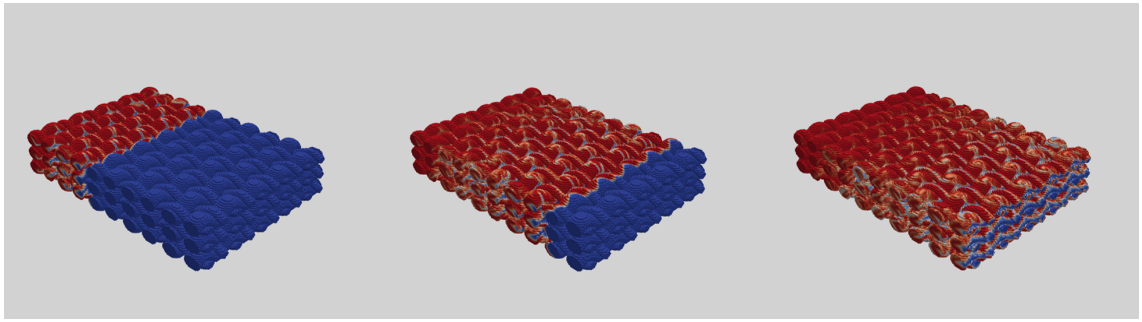

(b) Saturation of the tows at increasing time from left to right.

Figure 6.37: Saturation evolution in the weft tow direction

As expected, the channels in the fabric fills at a faster rate than the tows. The air bubbles within the channels are carried towards the outlet, while the impregnation of the tows is delayed due to their permeability. This delay in impregnation is particularly evident in the case of the warp direction (Figure 6.38 (b)), where even after the flow front reaches the outlet, the tows are still significantly far from being fully saturated.

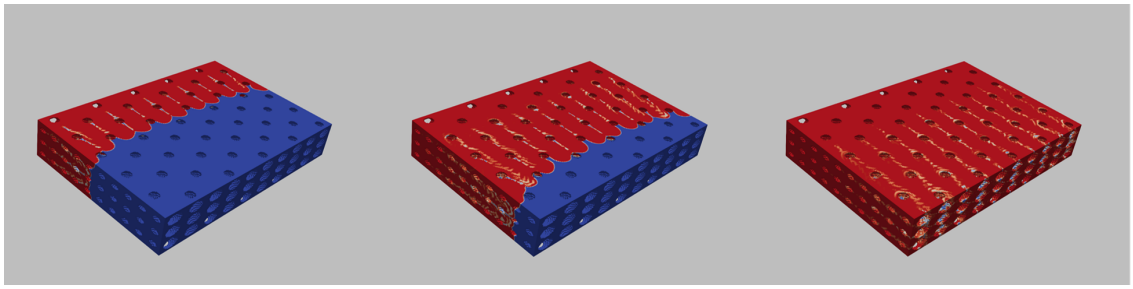

(a) Saturation of the channels at increasing time from left to right.

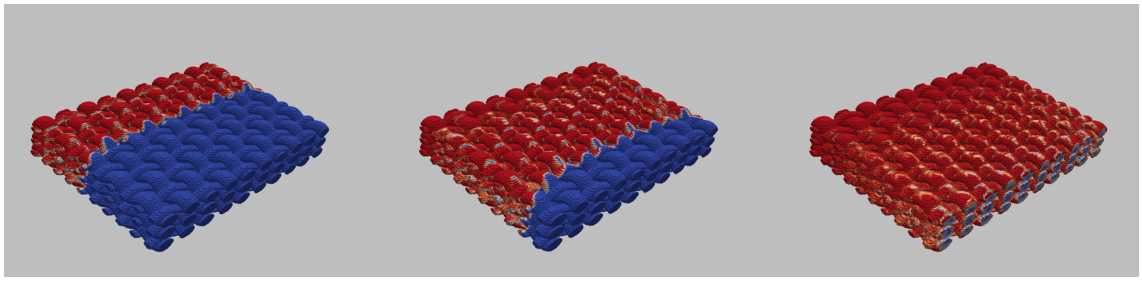

(b) Saturation of the tows at increasing time from left to right.

Figure 6.38: Saturation evolution in the warp tow direction

The saturation of the center cell shown in Figure 6.35 (b) has been calculated for

both weft and warp directions. Figure 6.39 shows that the cell reaches saturation more rapidly for the flow in the warp direction. In the case of the weft direction, there is a decrease in saturation at the beginning of the injection, which can be attributed to the flow leaving the cell due to initial turbulence.

In the first stage of filling (below 0.5 s) the saturation occurs in the channels more rapidly in the warp direction than the weft direction achieving almost full saturation. The flow in the warp direction is parallel to the warp (larger tows) and perpendicular to the weft (smaller tow). In contrast, in the weft direction, the residual saturation after the immediate filling of the channels will take considerably longer since since the volume to fill transversely in the warp tows is larger.

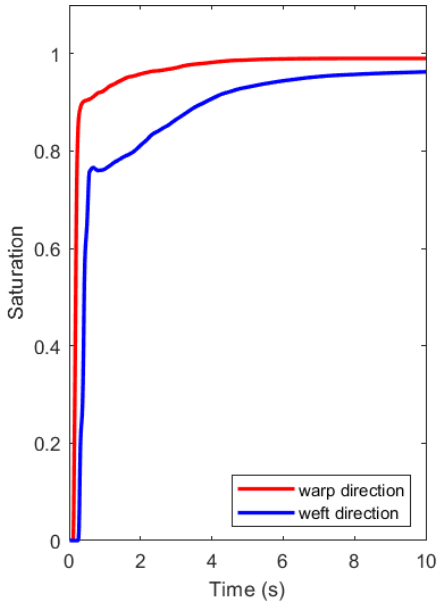

Figure 6.39: Average numerical saturation (α_l) measured within a center cell.

The experimental results, shown in Figure 6.40, confirm a similar trend to the numerical observations. Specifically, the slope at the initial stages of saturation is steeper for the warp direction compared to the weft direction. This difference can be attributed to two factors. Firstly, the intrinsic permeability in the warp direction ($K_x = K_{\text{warp}}$) is larger than that in the weft direction ($K_y = K_{\text{weft}}$), as illustrated in Figure 4.30. Secondly, the filling behavior of the weft and warp tows, which have different lineal weights, differs depending on whether the tow is parallel or perpendicular to the flow direction.

To determine the contribution of different components (channels, warp tows, and weft tows) to the overall saturation of the cell, the volume of fluid for each component was divided by the total volume of fluid in the cell. The results, as depicted in Figure 6.41, indicate that the channels hold the largest volume, followed by the warp tows, and finally the weft tows.

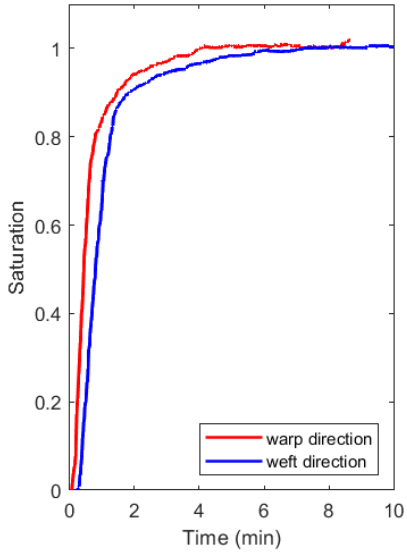

Figure 6.40: Experimental saturation evolution in warp and weft direction for $V_f = 50\%$

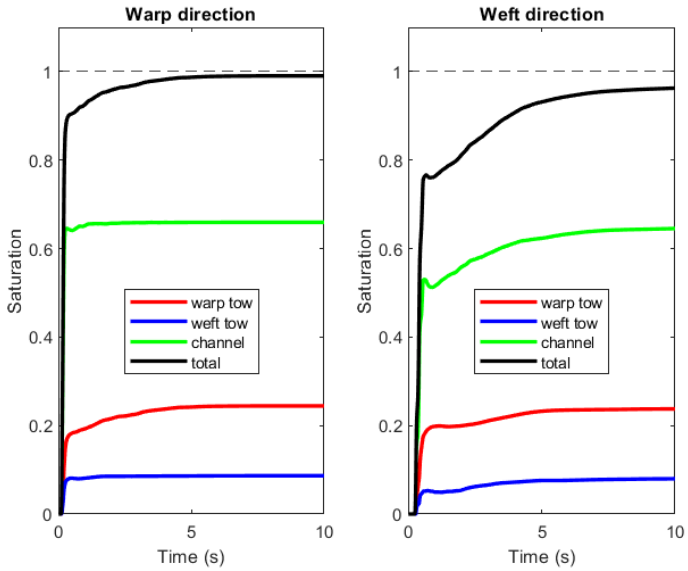

Figure 6.41: Numerical saturation contribution of channels, warp tows and weft tows in a unit cell.

Figure 6.42 provides a more detailed view of the delay observed at the beginning of saturation in the weft tow direction. The saturation rate (represented by the slope) is also less pronounced when the flow is parallel to the weft (smaller) and transverse to the warp (larger) tow (flow in the weft direction).

The smaller saturation rate observed in the weft tow direction aligns with expectations for transverse flow over a larger tow. This finding suggests that the tow itself may not significantly influence the measured unsaturated length discussed in Section 6.7.3.3. Instead, it is the overall geometry, including the non-addressed transverse tows, that has a greater influence on the saturation of the sensing region.

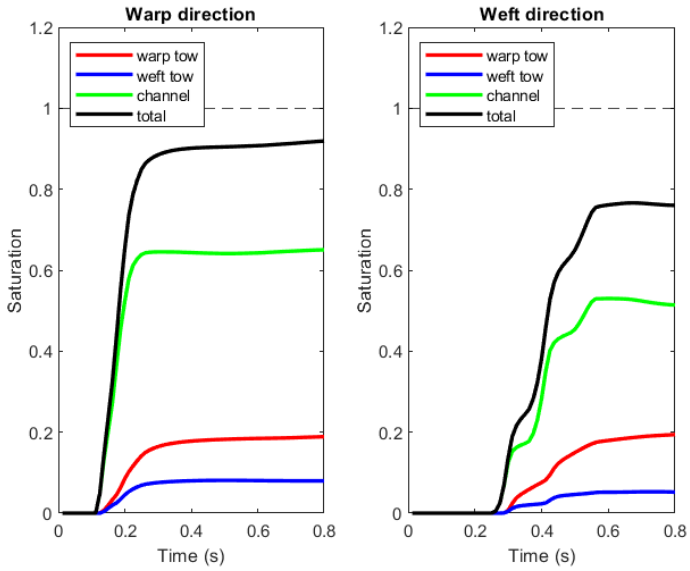

Figure 6.42: Numerical saturation contribution of channels, warp tows and weft tows in a unit cell from $0 < t < 0.8$ s in the warp (left) and weft (right) directions.

Table 6.5 shows that the volume of fluid at the end of injection is about twice that of the weft tows. This is qualitatively consistent with the size of the tows chosen for the model unbalanced fabric.

Component	Volume in warp direction (%)	Volume in weft direction (%)
Channels	66	64
Warp tows	24	23
Weft tows	10	9.5

Table 6.5: Volume contribution of indidividual components whithing individual cell (channels, warp tows and weft tows)

The next step is to replicate this numerical analysis by the simulation of the INCREASE06 geometry's using X-ray images to construct accurate models with more precise component dimensions and shapes as shown in the work of Umer et al. [3]. This enables the calculation of the saturation rate, as described earlier (an averaged value over a specific volume), and facilitates a comparison with experimental measurements obtained from the parallel plate dielectric sensor. By doing so, crucial information such as the time required for complete saturation and the contribution of each component can be extracted and analyzed.

6.9 Conclusion

A dielectric sensor was utilized to monitor the saturation evolution of the INCREASE06 interlock fabric during the injection process. The experimental setup was appropriately insulated from the conductive carbon fibers in the reinforcement and installed under a press (universal testing machine) to enable precise dielectric measurements at multiple V_f.

It was observed that the unsaturated length decreases as the macro bulk permeability decreases. When the fabric is compressed, the meso-voids become smaller, decreasing the

ratio between the bulk permeability (K_{bulk}) and tow permeability (K_{tow}). Consequently, the fabric exhibits a behavior closer to that of a single-scale fabric. Additionally, a slower impregnation speed resulted in a reduced unsaturated length, as evidenced by a comparison between sensor 1 (higher impregnation speed) and sensor 2 (lower impregnation speed).

Furthermore, the time required for complete impregnation of the sensing region was measured. At the highest level of compression ($V_f = 62\%$), it took approximately 12 minutes to fill the volume between the 4 $\times$ 4 cm copper plates entirely. This finding confirms the need for additional time towards the end of the C-RTM process to complete tow impregnation.

A preliminary numerical analysis was conducted on a simplified fabric model with unbalanced tows and tow spacing similar to that observed in the INCREASE06 geometry. The analysis revealed that the tows require significantly more time to achieve full saturation after the passage of the macroscopic flow front. Additionally, notable differences were observed in the filling behavior between the weft and warp directions. The size difference coupled with the distinct $K_{tow\perp}$ and $K_{tow\parallel}$ creates a difference in the filling of the tows when the flow is parallel and perpendicular.

In the future, a comprehensive simulation and numerical analysis will be conducted using an accurate INCREASE06 geometry, incorporating the actual tow shape and channel size. This analysis will be directly correlated with experiments employing parallel plate dielectric sensors by comparing averaged saturation values over a volume corresponding to the sensor size.

Chapter 7

General conclusion and outlook

This study focused on the characterization of the permeability of a carbon fiber interlock fabric used for the production of aircraft fan-blades and aimed to investigate the physical phenomena that may occur during the C-RTM process, which can have implications for the quality of the final part. The need for a revised permeability measurement technique arises from the implementation of new advanced 3D fabrics that have unique characteristics such as densely packed fiber tows and a more open geometry in comparison to traditionally used fabrics. Therefore, it is necessary to develop a measurement technique that accurately captures the permeability behavior of these advanced fabrics as their use is expected to become increasingly prevalent in future applications.

To achieve a comprehensive characterization of the permeability tensor over a range of fiber volume fractions (V_f) representative of the compression phase of the C-RTM process, a combination of permeability measurement techniques was employed. There were a number of challenges associated with this fabric. Firstly, the tows are made with carbon fibers, which are opaque and black, making flow visualization challenging. Additionally, it is thick and stiff, requiring tens or bar to compress it to its desired V_f and therefore, machinery with sufficient force is necessary. Lastly, the tows are quite dense and the geometry is open creating a highly contrasted dual-scale porosity medium and difficult tow impregnation affecting the overall permeability behavior.

The solution to these challenges was to use a combination of techniques described in Chapter 4. Firstly, a radial injection technique was used to measure the in-plane permeability and the in-plane and transverse deviation angles for three different V_f. The visualization of the flow was enhanced using a combination of fluorescent pigment and UV-light and the image was captured using a camera under the lower transparent plate. The investigation of the deviation angle is important for the subsequent measurements since if the flow is not aligned to the weft and warp directions the results need to be adjusted due to the rotation of the permeability tensor. For this particular fabric, the in-plane rotation was found to be negligible and therefore the measurements of the principal flow permeabilities could be made in the direction of the warp and weft tows. The transverse deviation angle is as important as the in-plane for increased thickness reinforcements as the INCREASE06 interlock. The transverse angle θ was measured using the projected distance between the injection point and the center of the ellipse formed at the bottom of the fabric. The transverse deviation value was quite high (about 30°) and later an incomplete filling RTM test were carried out and the transverse deviation was found to be very small. This difference can be explained by possible inaccuracies in determining the position of the center of mass in the binary image of the ellipse, leading to inaccurate measurements. Secondly, the hypothesis that the injection point coincides with the center

of the ellipse formed at the top was not confirmed. This could not be verified since the upper platen is metallic and the flow cannot be seen.

The radial injection technique provides valuable information on in-plane permeability, anisotropic ratio and flow's direction. However, this experiment is not practical for industrial implementation since it requires UV optical measurement equipment and a thick (60 mm) transparent platen. The same information can be extracted by performing an incomplete filling RTM process and measuring the ellipses formed at the top and bottom of the plate. Due to the very open geometry of the interlock, a fast cure resin was used in order to freeze the flow patterns. The anisotropic ratio was measured and was found to be in good agreement with that observed during the radial injection. The in-plane deviation can be measured by the angle between the ellipse axes and the tow direction and the transverse deviation is the angle formed between the center of the upper and lower ellipses. The in-plane permeability can be calculated with additional pressure information (measured at the inlet or another location in the impregnated area).

The transverse and the equivalent in-plane permeabilities were continuously measured using a saturated compression technique. This technique allows the saturated (intrinsic) permeability to be measured for a wide range of V_f with only one set of experiments. These values, in combination with the anisotropic ratio measured with the injection, provide both the in-plane permeabilities K_x and K_y and the transverse K_z permeability during compression. The proposed measurement protocol combines both techniques and can be carried out using less than 1 m^2 of fabric for full characterization, making this approach complete and economical given the high production cost of the interlock.

The two main permeabilities K_x and K_y can be measured continuously by designing two independent tests with a rectangular compression platen instead of a circular one. The use of the rectangular platen caused problems during the compression of the interlock which were later found to come from the deformation caused by the different pressure gradients arising in the different testing configurations (change in the fabric orientation relative to the rectangular platen). An in-depth analysis of flow induced deformation of the interlock fabrics was presented in Chapter 5. Tow washout (movement due to the viscous-drag forces) was found to start early on in the interlock fabrics, affecting the permeability measurement when the combination of fluid viscosity and closing speed generated too high fluid pressure. This behavior was compared to the deformation of well studied isotropic (twill) and anisotropic (quasi-UD) fabrics. A processing window was created for the INCREASE06 fabric during C-RTM. This window limits the process parameters (closing mold speed $\dot{h}$) in order to avoid flow-induced deformation during the manufacturing process.

The occurrence of flow-induced deformation can be identified when the measured fluid pressure deviates from the theoretical one. Different mechanical signatures were observed when comparing different geometries (twill and interlock). The deformation of the twill continues during the compression however, because of the high mobility of the tow in the uncompacted interlock, the tows will initially move easily (even for low viscous drag forces). Then as the displacement continues, because of the binding yarns of the interlock structure, the tows will tend to be locked in a deformed configuration and will not evolve anymore. An attempt to decrease the deformation and allow continuous measurement of K_x and K_y was made by designing a new compression platen with a smaller length to width ratio. The difference in the generated pressure fields in the two testing configuration was smaller with the new platen. This was sufficient to improve the tests of the quasi-UD fabric and allow the use of higher fluid viscosity without deformation but not for the interlock fabric as deformation occurs early on and the use of a lower fluid viscosity to avoid

flow-induced deformation did not generate enough fluid pressure for the measurements. It is concluded that the information from the radial injection test is still required for the calculation of K_x and K_y.

The radial injection technique captured a flow front that was non uniform and difficult to fit. Upon inspection it was clear that this contour was created by the filling of the inter-tow space (channels) being filled much faster than the tows. This behavior was also observed industrially during the manufacture of a plate during C-RTM. When the flow front reached the vents, it was observed that the tows were still not impregnated. This was improved by adding a step after compression where the injection pressure is increased and the fabric is left in the mold for an additional 30 minutes to continue impregnation. Both observations show that this fabric features a highly contrasted dual scale porosity structure that makes the impregnation of the tows challenging. Chapter 6 describes the implementation of an experimental saturation test. The experimental bench uses dielectric sensors to measure the changes in the dielectric properties of a fabric from dry to saturated. The tests were carried out in the warp and the weft directions at constant pressure. It was shown that this fabric has a very high unsaturated length (several cm) in comparison to traditional fabrics. The time to fully saturate the sensor region (4×4 cm) was shown to be around 12 minutes at the highest V_f, justifying the additional time added during the manufacturing. The sensor can be implemented in the C-RTM molds and be used as a tool for real-time saturation monitoring.

A preliminary numerical analysis was made at tow-scale. A simplified geometry with representative tow and tow-spacing was used to analyze the influence of an unbalanced tow size geometry on the flow. The simulation was performed using a modified solver in OpenFOAM which solved for the dual-phase flow in anisotropic double-scale porous media. Compressibility of the gas is implemented. This code is currently under development at GeM. The tows, in particular the warp, were shown to take significantly longer to impregnate after the passage of the flow front. The saturation curves were predicted from the simulation outcomes and correlated to the ones obtained from the dielectric measurement by averaging the saturation over a center cell. This study provided qualitative information on the influence of the tows and will serve as a stepping stone into the simulation of the real and more complex INCREASE06 geometry.

Outlook

Further experimental and numerical investigations should be carried out in order to better understand the behavior of the interlock fabric during the C-RTM process. An experiment is proposed in which glass tows are added into the weaving of the interlock. The technique described in Chapter 5 can only identify the occurrence of the deformation but do not provide information on the extent and type of deformation that occurs during the compression. The glass tows would act as tracers and can be dynamically tracked during the radial injection technique and would also provide contrast in a micro-CT analysis of a final part due to the density differences between carbon and glass. This analysis would provide valuable information on the effects of the tow washout, which is known to happen.

A micro-CT scan of the reinforcement can also be used to create an accurate geometrical representation to be studied. The saturation curves can be generated as mentioned in Chapter 6 and compared to the dielectric experiments. Furthermore, the virtual permeability of the material can be calculated as a function of saturation, taking into account the presence and transport of air within the structure.

The experimental characterization of the INCREASE06 interlock permeability re-

vealed that several physical phenomena can occur during the compression process, which can have direct impact on the measured permeability. These phenomena, resulting from the interaction between the fabric structure and the fluid forces under compression, contribute to the complexity of the permeability behavior. Understanding and accounting for these phenomena is crucial to accurately characterize the permeability of the interlock fabric. The highly contrasted dual-scale porosity structure of the fabric makes the filling of the tows challenging and should be further investigated through a combination of experimental and numerical analysis.

Bibliography

[1] H. Aimé. *Etude expérimentale et modélisation de la déformation de préformes fibreuses au cours de l'injection RTM haute pression.* PhD thesis, Ecole centrale de Nantes, 2014.

[2] H. Alhussein, R. Umer, S. Rao, E. Swery, S. Bickerton, and W. Cantwell. Characterization of 3d woven reinforcements for liquid composite molding processes. *Journal of materials science*, 51(6):3277–3288, 2016.

[3] M. Ali, R. Umer, K. Khan, and W. Cantwell. Xct-scan assisted flow path analysis and permeability prediction of a 3d woven fabric. *Composites Part B: Engineering*, 176:107320, 2019.

[4] R. Arbter, J. Beraud, C. Binetruy, L. Bizet, J. Bréard, S. Comas-Cardona, C. Demaria, A. Endruweit, P. Ermanni, F. Gommer, et al. Experimental determination of the permeability of textiles: A benchmark exercise. *Composites Part A: Applied Science and Manufacturing*, 42(9):1157–1168, 2011.

[5] M. S. S. S. Badawi. Development of the weaving machine and 3d woven spacer fabric structures for lightweight composites materials. 2008.

[6] S. Bickerton, M. Buntain, and A. Somashekar. The viscoelastic compression behavior of liquid composite molding preforms. *Composites Part A: Applied Science and Manufacturing*, 34(5):431–444, 2003.

[7] S. Bickerton, Q. Govignon, and P. Kelly. *Advanced fibre-reinforced polymer (FRP) composites for structural applications: 7. Resin infusion/liquid composite moulding (LCM) of advanced fibre-reinforced polymer (FRP).* Elsevier Inc. Chapters, 2013.

[8] M. A. Biot. Theory of elasticity and consolidation for a porous anisotropic solid. *Journal of applied physics*, 26(2):182–185, 1955.

[9] F. Boussu, I. Cristian, and S. Nauman. General definition of 3d warp interlock fabric architecture. *Composites Part B: Engineering*, 81:171–188, 2015.

[10] J. Bréard, Y. Henzel, F. Trochu, and R. Gauvin. Analysis of dynamic flows through porous media. part i: Comparison between saturated and unsaturated flows in fibrous reinforcements. *Polymer composites*, 24(3):391–408, 2003.

[11] M. Buntain and S. Bickerton. Compression flow permeability measurement: a continuous technique. *Composites Part A: Applied Science and Manufacturing*, 34(5): 445–457, 2003.

[12] J. Carey, G. Melenka, A. Hunt, and C. Ayranci. Introduction to braided composite material behavior. In *Handbook of Advances in Braided Composite Materials*, pages 207–237. Elsevier, 2017.

[13] F. J. Carrillo, I. C. Bourg, and C. Soulaine. Multiphase flow modeling in multiscale porous media: An open-source micro-continuum approach. *Journal of Computational Physics: X*, 8:100073, 2020.

[14] A. W. Chan and S.-T. Hwang. Anisotropic in-plane permeability of fabric media. *Polymer Engineering & Science*, 31(16):1233–1239, 1991.

[15] S. Comas-Cardona, C. Binetruy, and P. Krawczak. Unidirectional compression of fibre reinforcements. part 2: A continuous permeability tensor measurement. *Composites Science and Technology*, 67(3-4):638–645, 2007.

[16] S. Comas-Cardona, P. Le Grognec, C. Binetruy, and P. Krawczak. Unidirectional compression of fibre reinforcements. part 1: A non-linear elastic-plastic behaviour. *Composites science and technology*, 67(3-4):507–514, 2007.

[17] H. Darcy. *Les fontaines publiques de la ville de Dijon: exposition et application...* Victor Dalmont, 1856.

[18] A. Dereims. *Simulation industrielle des procédés d'élaboration de pièces composites par infusion de résine: couplage fluide/solide poreux très faiblement perméable en grandes déformations*. PhD thesis, Ecole Nationale Supérieure des Mines de Saint-Etienne, 2013.

[19] A. Endruweit and A. Long. Analysis of compressibility and permeability of selected 3d woven reinforcements. *Journal of composite materials*, 44(24):2833–2862, 2010.

[20] A. Endruweit, S. Gehrig, and P. Ermanni. Mechanisms of hydrodynamically induced in-plane deformation of reinforcement textiles in resin injection processes. *Journal of composite materials*, 37(18):1675–1692, 2003.

[21] B. R. Gebart. Permeability of unidirectional reinforcements for rtm. *Journal of composite materials*, 26(8):1100–1133, 1992.

[22] I. Gnaba, X. Legrand, P. Wang, and D. Soulat. Literature review of tufted reinforcement for composite structures. In *IOP Conference Series: Materials Science and Engineering*, volume 254, page 042011. IOP Publishing, 2017.

[23] S. Guéroult. *Analyse expérimentale de la saturation des milieux fibreux à double échelle de pores: application à la mise en oeuvre des matériaux composites par procédé RTM*. PhD thesis, Le Havre, 2012.

[24] T. G. Gutowski, Z. Cai, S. Bauer, D. Boucher, J. Kingery, and S. Wineman. Consolidation experiments for laminate composites. *Journal of Composite Materials*, 21(7): 650–669, 1987.

[25] T. G. Gutowski, T. Morigaki, and Z. Cai. The consolidation of laminate composites. *Journal of Composite Materials*, 21(2):172–188, 1987.

[26] K. F. Hasan, P. G. Horváth, and T. Alpár. Potential fabric-reinforced composites: a comprehensive review. *Journal of Materials Science*, 56(26):14381–14415, 2021.

[27] A. Hautefeuille. *Couplage écoulement-déformation des renforts fibreux dans les procédés de mise en œuvre des composites structuraux*. PhD thesis, Centrale Nantes, 2019.

[28] A. Hautefeuille, S. Comas-Cardona, and C. Binetruy. Mechanical signature and full-field measurement of flow-induced large in-plane deformation of fibrous reinforcements in composite processing. *Composites Part A: Applied Science and Manufacturing*, 118: 213–222, 2019.

[29] H. Jasak. *Error analysis and estimation for the finite volume method with applications to fluid flows*. PhD thesis, Imperial College London (University of London), 1996.

[30] M. K. Kang and W. Il Lee. Analysis of resin transfer/compression molding process. *Polymer composites*, 20(2):293–304, 1999.

[31] P. Kelly, R. Umer, and S. Bickerton. Viscoelastic response of dry and wet fibrous materials during infusion processes. *Composites Part A: Applied Science and Manufacturing*, 37(6):868–873, 2006.

[32] S. K. Kim and I. M. Daniel. Determination of three-dimensional permeability of fiber preforms by the inverse parameter estimation technique. *Composites Part A: Applied Science and Manufacturing*, 34(5):421–429, 2003.

[33] Y. R. Kim, S. P. McCarthy, and J. P. Fanucci. Compressibility and relaxation of fiber reinforcements during composite processing. *Polymer composites*, 12(1):13–19, 1991.

[34] L. Labat. *Etude des défauts de type vides pour la maîtrise du procédé RTM*. PhD thesis, Le Havre, 2001.

[35] L. Labat, J. Bréard, S. Pillut-Lesavre, and G. Bouquet. Void fraction prevision in lcm parts. *The European Physical Journal-Applied Physics*, 16(2):157–164, 2001.

[36] L. Labat, M. Grisel, J. Breard, and G. Bouquet. Original use of electrical conductivity for void detection due to injection conditions of composite materials. *Comptes Rendus de l'Académie des Sciences-Series IIB-Mechanics*, 329(7):529–534, 2001.

[37] A. Laurent-Mounier, C. Binétruy, and P. Krawczak. Multipurpose carbon fiber sensor design for analysis and monitoring of the resin transfer molding of polymer composites. *Polymer composites*, 26(5):717–730, 2005.

[38] F. LeBel, E. Ruiz, and F. Trochu. Experimental study of saturation by visible light transmission in dual-scale fibrous reinforcements during composite manufacturing. *Journal of Reinforced Plastics and Composites*, 36(23):1693–1711, 2017.

[39] A. C. Liakopoulos. Darcy's coefficient of permeability as symmetric tensor of second rank. *Hydrological Sciences Journal*, 10(3):41–48, 1965.

[40] B. Martin. *Etudes expérimentales de l'influence des paramètres de conception des renforts NCF unidirectionnels sur leurs propriétés de transport et leurs performances mécaniques*. PhD thesis, Paris, ENMP, 2015.

[41] B. Martin, S. Comas-Cardona, C. Binetruy, N. Billon, J.-L. Bouvard, and P. Lucas. Influence of fabrics' design parameters on the morphology and 3d permeability tensor of quasi-unidirectional non-crimp fabrics. *Composites Part A: Applied Science and Manufacturing*, 90:470–479, 2016.

[42] D. May, A. Aktas, S. Advani, D. Berg, A. Endruweit, E. Fauster, S. Lomov, A. Long, P. Mitschang, S. Abaimov, et al. In-plane permeability characterization of engineering textiles based on radial flow experiments: A benchmark exercise. *Composites Part A: Applied Science and Manufacturing*, 121:100–114, 2019.

[43] T. Mennecart, S. Gies, N. Ben Khalifa, and A. E. Tekkaya. Analysis of the influence of fibers on the formability of metal blanks in manufacturing processes for fiber metal laminates. *Journal of Manufacturing and Materials Processing*, 3(1):2, 2019.

[44] V. Michaud. A review of non-saturated resin flow in liquid composite moulding processes. *Transport in porous media*, 115(3):581–601, 2016.

[45] V. Michaud and J.-A. Månson. Impregnation of compressible fiber mats with a thermoplastic resin. part i: theory. *Journal of composite materials*, 35(13):1150–1173, 2001.

[46] V. Michaud and A. Mortensen. Infiltration processing of fibre reinforced composites: governing phenomena. *Composites Part A: applied science and manufacturing*, 32(8): 981–996, 2001.

[47] V. Michaud, R. Törnqvist, and J.-A. Månson. Impregnation of compressible fiber mats with a thermoplastic resin. part ii: Experiments. *Journal of composite materials*, 35(13):1174–1200, 2001.

[48] V. Nierstrasz and M. Warmoeskerken. *Process engineering and industrial enzyme applications*. Woodhead Publishing Ltd, Cambridge, 2003.

[49] M. Nordlund and V. Michaud. Dynamic saturation curve measurement for resin flow in glass fibre reinforcement. *Composites Part A: Applied Science and Manufacturing*, 43(3):333–343, 2012.

[50] D. of Materials Science and M. U. of Cambridge. URL `https://www.doitpoms.ac.uk/index.php`.

[51] S.-J. Park and M.-K. Seo. Element and processing. In *Interface science and technology*, volume 18, pages 431–499. Elsevier, 2011.

[52] X.-T. Pham, F. Trochu, and R. Gauvin. Simulation of compression resin transfer molding with displacement control. *Journal of reinforced plastics and composites*, 17 (17):1525–1556, 1998.

[53] A. Pickett. *Introduction to Process and Mechanical Modelling of Engineering Composites Part 1. Fundamentals*. 04 2021.

[54] K. Pillai and S. Advani. Numerical simulation of unsaturated flow in woven fiber preforms during the resin transfer molding process. *Polymer Composites*, 19(1):71–80, 1998.

[55] K. M. Pillai. Governing equations for unsaturated flow through woven fiber mats. part 1. isothermal flows. *Composites Part A: Applied Science and Manufacturing*, 33 (7):1007–1019, 2002.

[56] K. M. Pillai. Modeling the unsaturated flow in liquid composite molding processes: a review and some thoughts. *Journal of Composite materials*, 38(23):2097–2118, 2004.

[57] M. Richardson and Z. Zhang. Experimental investigation and flow visualisation of the resin transfer mould filling process for non-woven hemp reinforced phenolic composites. *Composites Part A: Applied Science and Manufacturing*, 31(12):1303–1310, 2000.

[58] F. Robitaille and R. Gauvin. Compaction of textile reinforcements for composites manufacturing. ii: Compaction and relaxation of dry and h2o-saturated woven reinforcements. *Polymer composites*, 19(5):543–557, 1998.

[59] F. Robitaille and R. Gauvin. Compaction of textile reinforcements for composites manufacturing. iii: Reorganization of the fiber network. *Polymer composites*, 20(1): 48–61, 1999.

[60] M. N. Saleh, A. Yudhanto, P. Potluri, G. Lubineau, and C. Soutis. Characterising the loading direction sensitivity of 3d woven composites: Effect of z-binder architecture. *Composites Part A: Applied Science and Manufacturing*, 90:577–588, 2016.

[61] H. S. Sas. *Addressing variability of fiber preform permeability in process design for liquid composite molding*. PhD thesis, University of Delaware, 2015.

[62] D. G. Seong, S. Kim, M. K. Um, and Y. S. Song. Flow-induced deformation of unidirectional carbon fiber preform during the mold filling stage in liquid composite molding process. *Journal of Composite Materials*, 52(9):1265–1277, 2018.

[63] D. G. Seong, J. S. Kim, M. K. Um, and D. Lee. Investigation on the mold compressive stage of compression resin transfer molding by using in-situ measurement of permeability variation of fiber preform. *Fibers and Polymers*, 20(3):651–655, 2019.

[64] D. Seto, R. Matsuzaki, A. Todoroki, and Y. Mizutani. Void formation in an anisotropic woven fiber during resin transfer molding. In *18th International Conference on Composite Materials*, 2011.

[65] S. Sharma and D. A. Siginer. Permeability measurement methods in porous media of fiber reinforced composites. *Applied Mechanics Reviews*, 63(2), 2010.

[66] J. C. Slattery. Single-phase flow through porous media. *AIChE Journal*, 15(6):866–872, 1969.

[67] P. Tan, L. Tong, and G. Steven. Modelling for predicting the mechanical properties of textile composites—a review. *Composites Part A: Applied Science and Manufacturing*, 28(11):903–922, 1997.

[68] H. Teixidó, J. Staal, B. Caglar, and V. Michaud. Capillary effects in fiber reinforced polymer composite processing: A review. *Frontiers in Materials*, 9(ARTICLE): 809226, 2022.

[69] H. Teixidó Pedarròs. *Visualization and modelling of dynamic flow in fibrous preforms for liquid composite molding*. PhD thesis, Ecole Polytechnique Fédérale de Lausanne (EPFL), 2023.

[70] K. Terzaghi, R. B. Peck, and G. Mesri. *Soil mechanics in engineering practice*. John Wiley & Sons, 1996.

[71] Texpedi.com. 3d woven fabric and its application in the composite industry, Nov 2020. URL `https://www.texpedi.com/2020/11/3D-woven-fabrics.html`.

[72] K. Tifkitsis and A. A. Skordos. A novel dielectric sensor for process monitoring of carbon fibre composites manufacture. *Composites Part A: Applied Science and Manufacturing*, 123:180–189, 2019.

[73] C. L. Tucker, R. B. Dessenberger, et al. Governing equations for flow and heat transfer in stationary fiber beds. *Composite Materials Series*, pages 257–257, 1994.

[74] R. Umer, H. Alhussein, J. Zhou, and W. Cantwell. The mechanical properties of 3d woven composites. *Journal of Composite Materials*, 51(12):1703–1716, 2017.

[75] N. Vernet, E. Ruiz, S. Advani, J. B. Alms, M. Aubert, M. Barburski, B. Barari, J. M. Beraud, D. C. Berg, N. Correia, et al. Experimental determination of the permeability of engineering textiles: Benchmark ii. *Composites Part A: Applied Science and Manufacturing*, 61:172–184, 2014.

[76] J. Weitzenböck, R. Shenoi, and P. Wilson. Measurement of three-dimensional permeability. *Composites Part A: Applied Science and Manufacturing*, 29(1-2):159–169, 1998.

[77] J. Weitzenböck, R. Shenoi, and P. Wilson. Radial flow permeability measurement. part a: Theory. *Composites Part A: Applied Science and Manufacturing*, 30(6):781–796, 1999.

[78] J. Weitzenböck, R. Shenoi, and P. Wilson. A unified approach to determine principal permeability of fibrous porous media. *Polymer composites*, 23(6):1132–1150, 2002.

[79] H. G. Weller, G. Tabor, H. Jasak, and C. Fureby. A tensorial approach to computational continuum mechanics using object-oriented techniques. *Computers in physics*, 12(6):620–631, 1998.

[80] B. Yenilmez and E. M. Sozer. A grid of dielectric sensors to monitor mold filling and resin cure in resin transfer molding. *Composites part a: applied science and manufacturing*, 40(4):476–489, 2009.

[81] A. X. Yong, A. Aktas, D. May, A. Endruweit, S. Lomov, S. Advani, P. Hubert, S. Abaimov, D. Abliz, I. Akhatov, et al. Experimental characterisation of textile compaction response: A benchmark exercise. *Composites Part A: Applied Science and Manufacturing*, 142:106243, 2021.

[82] M. Yun, H. Sas, P. Simacek, and S. G. Advani. Characterization of 3d fabric permeability with skew terms. *Composites Part A: Applied Science and Manufacturing*, 97: 51–59, 2017.

[83] W. Zhao, N. Pei, and C. Xu. Experimental study of carbon/glass fiber-reinforced hybrid laminate composites with torsional loads by using acoustic emission and micro-ct. *Composite Structures*, 290:115541, 2022.

Titre : Influence du contraste élevé de double échelle de porosités des renforts interlock en carbone sur leur perméabilité, déformations induites par écoulement et saturation pendant le moulage CRTM - Caractérisation expérimentale et modélisation

Mots clés : interlock, carbone, perméabilité, double échelle, saturation, caractérisation

Résumé : Un premier objectif de cette thèse est de développer une méthodologie de mesure de perméabilité qui caractérise avec précision le tenseur complet de perméabilité d'un tissu en interlock en carbone utilisé dans la fabrication des aubes de turbine d'avion par le procédé C-RTM. Les caractéristiques uniques du tissu, notamment ses épaisseur et rigidité élevées, ses fibres opaques et sa double échelle de porosité très marquée, présentent des défis lors de l'utilisation de techniques de mesure traditionnelles.

Afin de mesurer le tenseur complet de perméabilité de façon économique et sur une plage étendue de fraction volumique de fibres, une combinaison de méthodes expérimentales a été proposée et utilisée.

Les travaux portent également sur l'étude de l'apparition de déformations du réseau fibreux induites par l'écoulement et propose une fenêtre de procédé optimale pour imprégner les interlocks lors du procédé C-RTM.

Le développement d'un banc d'essai expérimental pour mesurer la saturation pendant l'injection est présenté, ainsi que l'influence de sa double échelle de porosité très marquée. Les résultats sont complétés par une modélisation numérique préliminaire à l'échelle mésoscopique d'une géométrie simplifiée représentative.

Les défis posés par la double échelle marquée de l'espace poral et les modes d'imprégnation du tissu en interlock qui en découlent, justifient de l'approche proposée, combinant analyse expérimentale et modélisation, qui doit être poursuivie pour approfondir l'étude de ces mécanismes.

Title : Influence of highly contrasted dual-scale porosity carbon interlock fabrics on permeability, flow-induced deformation and saturation during CRTM process - Experimental characterization and modeling

Keywords : interlock, carbon, permeability, dual-scale, saturation, characterization

Abstract :

A primary objective of this thesis is to develop a permeability measurement methodology that accurately characterizes the full permeability tensor of a carbon interlock fabric used in the manufacture of aircraft turbine blades using the C-RTM process. The unique characteristics of the fabric, including its high thickness and stiffness, its non-transparent fibers and its pronounced dual-porosity scale, present challenges when using traditional measurement techniques.

In order to measure the full permeability tensor economically and over a wide range of fiber volume fractions, a combination of experimental methods has been proposed and applied.

The development of an experimental test bench to measure saturation during injection and the influence of its very strong double porosity scale is presented. The results are complemented by preliminary mesoscopic numerical modelling of a representative simplified geometry.

The challenges posed by the pronounced double scale of the pore space and the resulting modes of impregnation of the interlocked fabric justify the proposed approach of combining experimental analysis and modelling, which must be pursued in order to study these mechanisms in greater depth.